Charles University in Prague

Faculty of Mathematics and Physics

MASTER THESIS

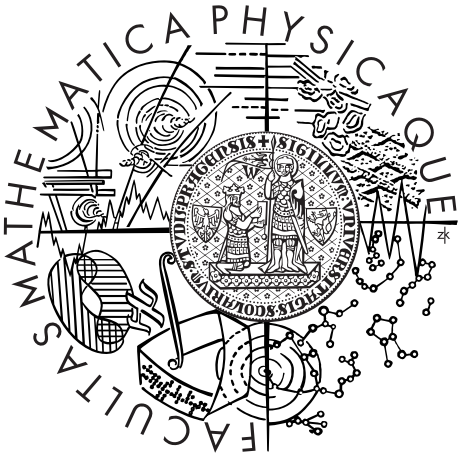

Alexander Pitňa

Statistické zpracování družicových dat gama záblesků družice Fermi

Astronomical Institute

Supervisor of the master thesis: doc. RNDr. Attila Mészáros, DrSc.

Study programme: Physics

Specialization: Astronomy and Astrophysics

Prague 2013

Charles University in Prague

Faculty of Mathematics and Physics

MASTER THESIS

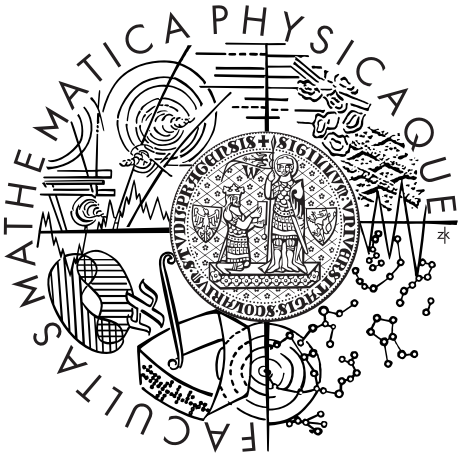

Alexander Pitňa

Statistical analysis of the Fermi gamma-ray space telescope data

Astronomical Institute

Supervisor of the master thesis: doc. RNDr. Attila Mészáros, DrSc.

Study programme: Physics

Specialization: Astronomy and Astrophysics

Prague 2013

Acknowledgements

Firstly, I would like to express my gratitude to my master thesis supervisor, doc. RNDr. Attila Mészáros, DrSc., for his leadership and helpful advices. Secondly, I appreciate the help of my friends and family, especially Barbora Lásková, Marek Nad' for useful discussions.

I declare that I carried out this master thesis independently, and only with the cited sources, literature and other professional sources.

I understand that my work relates to the rights and obligations under the Act No. 121/2000 Coll., the Copyright Act, as amended, in particular the fact that the Charles University in Prague has the right to conclude a license agreement on the use of this work as a school work pursuant to Section 60 paragraph 1 of the Copyright Act.

In Prague date 12.4.2013 Alexander Pitňa

Název práce: Statistické zpracování družicových dat gama záblesků družice Fermi
Autor: Alexander Pitňa
Katedra: Astronomický ústav Univerzity Karlovy
Vedoucí diplomové práce: doc. RNDr. Attila Mészáros, DrSc., Astronomický ústav Univerzity Karlovy

Abstrakt: Gama záblesky jsou jedním z jevů, kterým astrofyzici dosud zcela nerozumí. Z důvodu jejich extremních luminozit jsou viditelné v kosmologických vzdálenostech. Proto se mohou stát nástrojem, kterým bychom mohli zkoumat mladý vesmír. Tato práce je zaměřena na určení celkové vyzářené energie gama záblesků, jejich luminozit a závislost těchto veličin na rudém posuvu. Při zkoumání 28 dlouhých gama záblesků se známými rudými posuvy je nalezena závislost těchto veličin na rudém posuvu. Dále se práce zabývá tím, zda-li je tato závislost zapříčiněna výběrovým efektem detekce nebo se jedná o skutečný astrofyzikální jev. Nejdříve je ukázáno, že příslušná k-korekce má na závislost těchto veličin na rudém posuvu jen malý, pokud ne žádný vliv. Za druhé, je navrhnut nový přístup jak studovat závislost luminozitní funkce na rudém posuvu. Za třetí, je ukázáno, že vzorek gama záblesků s určenými rudými posuvy je vychýlený, což znamená, že při kombinování měření z různých zdrojů je třeba být opatrný. Z výsledků plyne, že závislost veličin na rudém posuvu se dá vysvětlit výběrovým efektem detekce.

Klíčová slova: gama záblesky, družice Fermi, kosmologie

Title: Statistical analysis of the Fermi gamma-ray space telescope data
Author: Alexander Pitňa
Department: Astronomical Institute of Charles University in Prague
Supervisor: doc. RNDr. Attila Mészáros, DrSc., Astronomical Institute of Charles University

Abstract: Gamma-ray bursts (GRBs) are one of the phenomena that still puzzle the astrophysicists. Due to their extreme luminosities, they are visible in cosmological distances. They could provide a tool for understanding the early Universe. This thesis focuses on the estimation of the total energy released by the GRBs, their luminosities and how these quantities depend on the redshift. For a sample of 28 long GRBs with known redshifts, a dependence of their total energies and luminosities on the redshift is found. The thesis further studied if this dependence is either an observational bias or a real astrophysical phenomenon. Firstly, proper use of k-correction revealed that it has little effect on the redshift dependence of these quantities. Secondly, a new approach has been proposed to investigate the redshift dependence of the luminosity function. Thirdly, selection effect has been found, when investigating the sample of bursts with known redshifts, implying a caution when combining data from different sources. All these efforts show that the observational bias can still explain the redshift dependence.

Keywords: Gamma-ray burst, Fermi satellite, Cosmology

Contents

Chapter 1

Introduction

In this thesis I will present the results of the study of a phenomenon known as the gamma-ray bursts (GRBs). GRBs are extra luminous nonrepetitive explosions in deep space encompassing a wide range of distances and energy releases. Typical photon energies in peak luminosity are of the order of hundreds of keV. In redshift units z, which can be measured with high precision, the range is roughly 0.1 to 10. The actual distance depends on the chosen cosmological model. The upper boundary is not known, but is likely to be much higher, reaching into the era of the massive first generation stars. Energy release ranges from 10^{50} to 10^{54} ergs and, considering the time scales on which the energy is radiated, serious constraints are put on the modeling of a progenitor and radiation mechanism. Time scale ranges from hundredths to a few hundreds of seconds with clear distinction of two types of GRBs, the short GRBs with time scales less than 2 s and the long GRBs with time scales more than 2 s. Therefore, it is needed to come up with two profoundly different progenitors for each group. In either case, connection with the Star Formation Rate (SFR) is reasonable, because of the compactness of the source derived from the variations in light curves. This connection has been studied but there are still many puzzles to solve.

The Fermi Gamma-ray Space Telescope (Fermi) is a latest tool for studying, among many other phenomena, the connection between the Star Formation Rate (SFR) and the GRB rate. Together with the Swift satellite and InterPlanetary Network (IPN – group of satellites that can detect the gamma-rays) more redshifts measurements for the GRBs can be obtained.

The focus of the thesis is to derive some intrinsic properties of the GRBs detected by the Fermi satellite. Next, I will study the GRB rate and possible luminosity function evolution by analyzing these intrinsic properties. Attention will be put also on the estimation of the degree of biases.

The structure of the thesis is as follows. The history and present knowledge of the GRBs is presented in the second Chapter. The third Chapter describes the Fermi

satellite, its onboard instruments and data products. In the fourth Chapter I discuss the acquiring of the data and creation of the samples used later in the analyses. The fifth Chapter consists of the description of intrinsic properties and the theory of the k-correction in a gamma range and its proper usage in the calculation of the intrinsic properties. Further, the analysis of data with respect to GRB rate and GRB luminosity function will be described. In the sixth Chapter I perform the statistical tests to account for the biases introduced in Chapter four. In seventh Chapter I summarize the results. Chapter 2–3 are review parts and do not contain any new result of the author. In these two Chapters the brevity is kept and the theory of physical models is omitted, because in 2011 two reviews were published in the Astronomical Institute of the Charles University (Řípa 2011; Bystřický 2011). The Chapters 4–7 give the results of the authors study. The thesis contains also four Appendices describing the used statistical tests, computation of uncertainties, list of physical quantities used for computation of the intrinsic properties and the list of the GRBs that were used for analyses. Finally, the list of the cited publications, the list of abbreviations, the list of tables and the list of figures are included.

Chapter 2

Summary of the Gamma-ray Bursts

In this chapter a brief overview of the GRBs is presented. The review starts with the earliest detection of the GRBs, a description of the current knowledge of the GRBs and ends with the latest knowledge of the GRBs. The overview was drawn from the several publications (Klebesadel et al. 1973; Fishman and Meegan 1995; van Paradijs et al. 1997; Heise et al. 2001; Stanek et al. 2003; Hjorth et al. 2003; Barthelmy et al. 2005; Kouveliotou et al. 1993; Horváth 1998; Balázs et al. 2003; Band et al. 1993; Bloom et al. 2001; Butler et al. 2010; Wanderman and Piran 2010; Lloyd-Ronning et al. 2002; Firmani et al. 2005; Salvaterra et al. 2012; Amati et al. 2002; Yonetoku et al. 2004; Schaefer 2007; Schaefer et al. 2001; Virgili et al. 2012; Gruber 2012; Wang et al. 2011; Zhang et al. 2012; Xu and Huang 2012; Mészáros 2006; Řípa et al. 2012) and for more detailed information one should look into them.

2.1 History

In exaggeration, for the earliest detection we may thank to the nuclear arm races in the middle seventies. The U.S. military satellites Vela provided the means to control the violation of the nuclear test ban treaty signed by the nuclear powers in 1963. Soon after the launch of the satellites, the unexpected detection of gamma–ray photons certainly surprised the U.S. military. Simple telemetry revealed that the gamma–rays did not come from the Earth but rather from the outer space. Since then, the detection of the GRBs continues to flourish. Sixteen bursts were detected between 1969 July and 1972 July. The observations were made by the CsI scintillation detectors on the four Vela satellites, Vela 5A, 5B, 6A and 6B. Energy ranges of the detectors were 0.2–1.0 MeV for Vela 5 and 0.3–1.5 MeV for Vela 6. Burst durations were in the interval of 0.1–30

s and significant variations in time curves were observed. The total detected fluence ranged from 10^{-5} erg·cm^{-2} to $2 \cdot 10^{-4}$ erg·cm^{-2} (Klebesadel et al. 1973).

Several observations after the detection by the Vela satellites were performed, which further widened our knowledge of the GRBs. After a long period of stagnation, Compton Gamma–Ray Observatory (CGRO), launched in 1991, greatly improved our understanding of GRBs. Onboard instrument Burst And Transient Source Experiment (BATSE) showed that the GRBs were distributed isotropically, suggesting cosmological origin. The results of the survey about the BATSE instrument are summarized in (Fishman and Meegan 1995).

After the successful BATSE survey, an Italian–Dutch satellite Beppo-SAX was launched in 1997. Its main contribution in understanding the GRBs was the confirmation of their cosmological origin. The position of the burst could be determined by detection of x-ray images. That opened the possibility of afterglow measurements on longer wavelengths leading to identification of the host galaxies (van Paradijs et al. 1997).

In 2000 the High Energy Transient Explorer (HETE-2) was launched. The mission further widened our understanding of GRBs. Firstly, it confirmed a new class of objects called X-ray flashes (XRF) discovered by Beppo-SAX satellite (Heise et al. 2001). Their typical energies are lower compared to those of GRBs. Secondly, it made the first association of the GRB with supernova (SN2003dh)(Stanek et al. 2003; Hjorth et al. 2003).

The next great shift in GRB detection was achieved in 2004 by launching the Swift Gamma-Ray Burst Mission. Swift is a multi-wavelength observatory to a great extent dedicated to the study of GRBs. It consists of three instruments. Burst Alert Telescope (BAT) is able to calculate a position of the burst with accuracy of 1–4 arcminutes within 15–20 s. Its Field of View (FoV) is one steradian (fully coded) and three steradians (partially coded). Energy range is 15–150 keV with ∼7 keV resolution and a sensitivity of 10^{-8} erg·s·cm^2 (Barthelmy et al. 2005). The second instrument, X-ray Telescope (XRT), provides more precise location with accuracy of cca 2 arcseconds. The energy range is 0.2–10 keV. The third instrument, the Ultraviolet/Optical Telescope (UVOT), provides a position in fractions of arc-seconds and performs optical and ultraviolet photometry and low resolution spectra in 170–650 nm[1].

The latest satellite launched in 2008, partially dedicated to the study of the GRBs, is the Fermi Gamma-ray Space Telescope. It will be described in detail in Chapter 3.

[1] http://Swift.asdc.asi.it/

2.2 Prompt Emission Properties

In this section of the thesis the prompt emission properties of the GRBs will be described shortly. GRBs show high variability in durations, fluxes, light curves and spectral characteristics. Since I will study the long duration GRBs, they will be described in more detail than the short group of GRBs.

2.2.1 Durations

The durations ranges of the GRBs covers many order of magnitudes: starting with very short 0.01 s ending up to 1000 s. Many definitions of specific durations of the GRBs exist. The most common is T_{90}, defined as the time during which 90 % of the total fluence (fluence will be explained in subsection 2.2.2) was accumulated between the time at which 5 % of the fluence was detected and the time at which 95 % of the fluence was detected. Instead of the total fluence, fluence in arbitrary energy interval can be used to compute T_{90}. T_{90} provides a reasonable estimation of the total duration of the burst.

A distinction of the GRBs into two subgroups is obvious considering the duration distribution shown in Figure 2.1 (Kouveliotou et al. 1993). The bimodality of the duration distribution has been observed several times with differrent satellites. Time boundary of duration is usually set to 2 s. The bursts having T_{90} shorter than 2 s are considered as short bursts (denoted sGRBs), conversely the bursts having T_{90} longer than 2 s are considered as long bursts (denoted lGRBs). However, with the rising number of the detected GRBs providing better statistics, introduction of the third group was proposed by Horváth (1998) having T_{90} around 2–10 s. Presently, no firm conclusion has been reached about this "intermediate" subgroup and the question remains open. The short and intermediate bursts will not be studied in this thesis.

Important empirical characteristic of the duration distribution is the log–normality. The $\log(T_{90})$ shows normal distribution with high level of significance (Balázs et al. 2003). Log–normal distribution is often seen, if the observed properties of the GRBs are studied.

2.2.2 Peak Fluxes and Fluences

Peak flux is defined as the maximum flux [ph·cm^{-2}·s^{-1}] over some timescale $\delta\tau$ considering photons within the energy interval $\langle E_1, E_2\rangle$. The timescale $\delta\tau$ usually depends on the instrument. For example, for the BATSE $\delta\tau = 64\,\mathrm{ms}, 256\,\mathrm{ms}, 1024\,\mathrm{ms}$. Measured peak fluxes are determined by the instrument which detects the burst. The lowest threshold limit differs for each satellite depending on the onboard detectors. It is usually between 0.2–0.7 ph·cm^{-2}·s^{-1}. For the bright bursts the peak fluxes may exceed 50

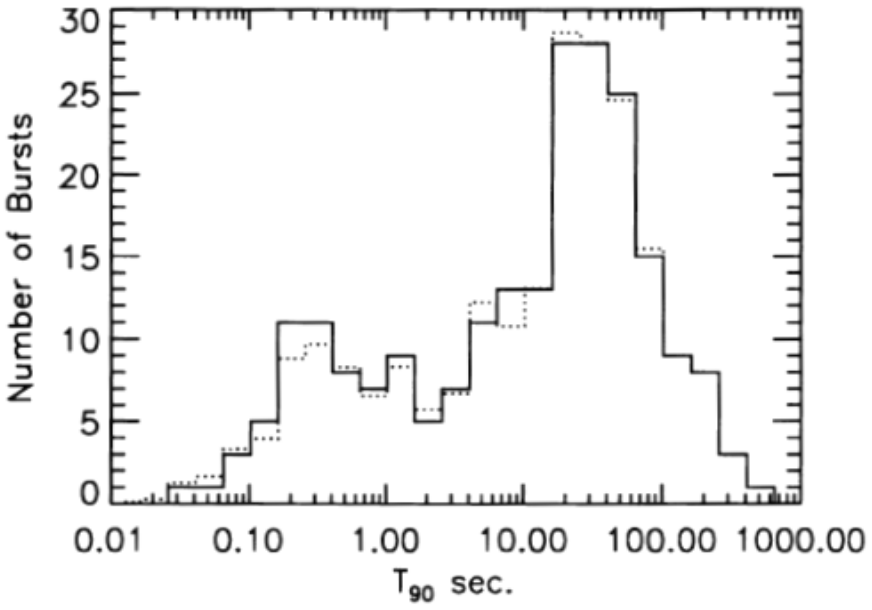

FIGURE 2.1: Distribution of T_{90} of the first BATSE catalogue (Kouveliotou et al. 1993).

ph·cm^{-2}·s^{-1}. Measured count rates, from which the peak fluxes and light curves are determined, are complicated functions of time for many GRBs.

Fluence is defined as the total detected energy in energy range $\langle E_1, E_2 \rangle$ over the time range of the burst (commonly T_{90}) in units of erg·cm^{-2}. Typical fluences, in the energy interval 50–300 keV, are 10^{-8}–10^{-4} erg·cm^{-2}. Fluences show a log–normal distribution for the different subgroups (Balázs et al. 2003).

2.2.3 Light Curves

The profiles of the light curves are unique for each burst. Regardless, some pattern among them can be found. According to Fishman and Meegan (1995) the profiles of the bursts can be divided into these classes: a) Single pulse or spike events b) Smooth, either single or multiple, well defined peaks c) Distinct, well-separated episodes of emission; and d) Very erratic, chaotic and spiky bursts. In figure 2.2 these classes are illustrated. The fastest observed time variations Δt in the light curves were of the order of thousandths of seconds implicating compact source of radiation. Simple calculation using formula $D \lesssim \Gamma^2 c\Delta t$ reveals that the typical length scale D of the source must be in the orders of 10^2–10^6 km depending on the Lorenz Γ factor (calculation with Γ= 1–100). c is the velocity of light.

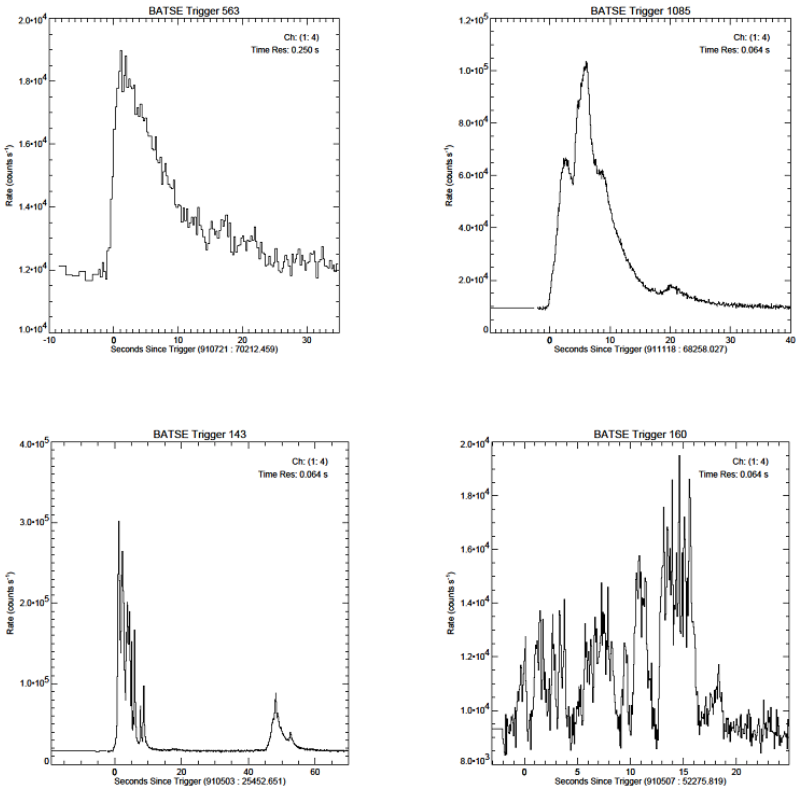

FIGURE 2.2: The profiles of the four light curves of GRBs detected by the BATSE satellite. Upper left image illustrates single pulse light curve (LC). Upper right image illustrates smooth multiple LC. Lower left image illustrates well-separated episodes of emission. Lower right image illustrates chaotic and spiky bursts. (Credit: http://www.batse.msfc.nasa.gov/batse/grb/lightcurve/)

2.2.4 Spectra

Characteristics of the light curves have a wide range of possible values. On the other hand, spectral functions used for fitting the time integrated or peak flux spectra are less diverse. The spectra are unambiguously non-thermal and can be fitted by a number of specific spectral functions (see section 4.2.5). A spectral function proposed by Band et al. (1993) (called Band spectrum after David Band) has the form

$$N_{\mathrm{BAND}}(E) = \begin{cases} A\left(\frac{E}{100\ \mathrm{keV}}\right)^{\alpha} \exp\left(-\frac{(\alpha+2)E}{E_{\mathrm{peak}}}\right) & \mathrm{if}\, E < \frac{(\alpha-\beta)E_{\mathrm{peak}}}{\alpha+2} \\ A\left(\frac{E}{100\ \mathrm{keV}}\right)^{\beta} \exp(\beta-\alpha)\left(\frac{(\alpha-\beta)E_{\mathrm{peak}}}{100\ \mathrm{keV}(\alpha+2)}\right)^{\alpha-\beta} & \mathrm{if}\, E \geq \frac{(\alpha-\beta)E_{\mathrm{peak}}}{\alpha+2} \end{cases}, \tag{2.1}$$

where the amplitude A is in units $\left[\mathrm{ph}\cdot\mathrm{s}^{-1}\cdot\mathrm{cm}^{-2}\cdot\mathrm{keV}^{-1}\right]$, α is a low-energy index, β is a high-energy index and E_{peak} in [keV] is the peak energy in a so called $E^2N_{\mathrm{BAND}}(E)$ spectrum. The $E^2N_{\mathrm{BAND}}(E)$ spectrum represents the total energy flux per energy band. In figure 2.3 the example of a spectral fit with Band function is shown.

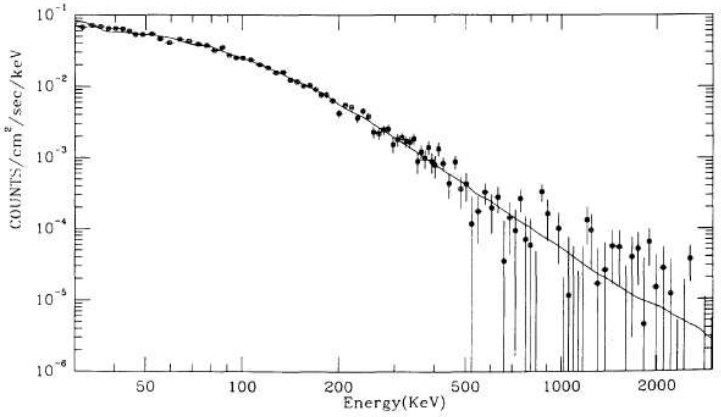

FIGURE 2.3: Example of a spectral fit to the average spectrum of GRB911127. (Credit: Band et al. (1993))

An empirical spectral function in this form can fit the spectrum of the burst reasonably well. Due to the fact that the peak energy $E_{\rm peak}$ of the bursts correlates with some intrinsic properties of the bursts, it is possibly the most studied parameter. These correlations will be described in section 2.3.4.

2.3 Derived Intrinsic Properties

In this section the intrinsic properties of the long duration GRBs will be described. Thanks to the Swift satellite, we have now determined redshifts for many lGRBs, which are crucial in deriving of the intrinsic properties.

Like the supernova type Ia, the GRBs could become a new independent tool for testing the cosmological models and studying the early Universe ($z > 6$). However, many requirements must be satisfied, which are not usually measured well. Arguably, the most important necessity is to find an intrinsic quantity that does not depend on the redshift, second could be the intrinsic scatter of the quantity and third the calibration. Naturally, all three requirements must be fulfilled, for a good cosmological tool.

In the following subsections, some of the intrinsic properties, and their observed redshift dependencies, will be described together with some observed correlations between them.

2.3.1 Isotropic Equivalent Energy

In general, the total emitted energy of an astrophysical source, and the time scale over which this energy is radiated, put a constraint on the physics of the radiation mechanism. Considering the lGRBs, the total emitted energy in the comoving frame of reference is immense $E_{\rm iso} \approx 10^{53}\,{\rm erg}$ and the time scale over which this energy is released is in the order of 1–100 of seconds. Importantly, this energy is derived under

the assumption that the source radiates *isotropically* (therefore the subscript "iso"). The estimation of $E_{\rm iso}$ is straightforward, when the redshift of the burst is determined. It is an important note that $E_{\rm iso}$ need not be the real total energy emitted by a GRB. If there is a beaming, i.e. if GRB emits into a solid angle Ω, then the topical energy is lowered by a factor $4\pi/\Omega$. The question of beaming is not a subject of this thesis and therefore it will be discussed only shortly in subsection 2.3.4.

Bloom et al. (2001) estimated the $E_{\rm iso}$ (taking 17 bursts) in $\langle E_1, E_2\rangle = \langle 0.1, 10\,000\rangle$ keV comoving energy band. The values lie in the range $10^{51.5}\sim10^{54.5}$ erg, showing a large intrinsic scatter in ~ 3 orders of magnitude. Butler et al. (2010) have found that $E_{\rm iso}$ (taking 67 bursts) – in $\langle 1, 10\,000\rangle$ keV energy band – covers even wider energy range $10^{50}\sim10^{54.5}$ erg. The fact that the $E_{\rm iso}$ covers such a wide range of energies puts strong constrains on the theoretical modeling of the progenitor.

2.3.2 Isotropic Peak Luminosity

An isotropic peak luminosity $L_{\rm iso}$ is a luminosity of the burst in the comoving frame of reference. Subscript "iso" denotes the assumption of the isotropic radiation of the source. The timescale over which this quantity is usually derived is 1024 ms. Such as for $E_{\rm iso}$, $L_{\rm iso}$ is computed in an arbitrary comoving energy band $\langle E_1, E_2\rangle$.

Yonetoku et al. (2004) found that $L_{\rm iso}$ in units of $\left[\mathrm{erg}\cdot\mathrm{s}^{-1}\right]$, computed in $\langle 30, 10\,000\rangle$ keV energy interval, ranges from 10^{51} erg $\cdot\,\mathrm{s}^{-1}$ to $5\cdot10^{53}$ erg $\cdot\,\mathrm{s}^{-1}$.

2.3.3 Luminosity Function

In general, luminosity function Φ gives the fraction of astrophysical objects per unit luminosity. Considering the GRBs, the full shape of their luminosity function, which characterizes the GRB emission mechanism, is unknown. Many authors (Butler et al. 2010; Wanderman and Piran 2010; Lloyd-Ronning et al. 2002; Firmani et al. 2005; Salvaterra et al. 2012) have derived different forms and constraints of the luminosity function, and its fundamental property, the dependence on the redshift z, still remains unresolved. The following paragraphs briefly summarize the various estimations of the luminosity function by a number of studies.

Butler et al. (2010) have found that the GRB luminosity function is best written as a broken power law in the effective luminosity L $\left[\mathrm{erg}\cdot\mathrm{s}^{-1}\right]$ as

$$\Phi(L) = \frac{\mathrm{d}N}{\mathrm{d}\log L} \propto \begin{cases} L^{\alpha=-0.2\pm0.2} & \text{for} \quad \log L < \log L_* = 52.7\pm0.4 \\ L^{\beta=-3.0\pm1.5} & \text{for} \quad \log L > \log L_* = 52.7\pm0.4 \end{cases}, \tag{2.2}$$

and

$$L = \frac{E_{\rm iso}}{(1+z)^{0.0\pm0.5}} \left(\frac{10^{2.5}\mathrm{keV}}{E_{\rm peak}}\right)^{1.8\pm0.3} \left(\frac{10^{0.6}\mathrm{s}}{T_{r45,z}}\right)^{0.4\pm0.2}, \tag{2.3}$$

where $E_{\rm iso}$ [erg] is defined over $\langle 1, 10\,000\rangle$ keV energy interval, $E_{\rm peak}$ is defined in section 2.2.4 and $T_{r45,z}$ is a high-luminosity duration.

Luminosity function in this functional form (see the coefficient over $(1+z)$ in eq. 2.3) is not dependent on redshift.

Similarly, Wanderman and Piran (2010) have found the luminosity function distribution in a form of a broken power law (eq. 2.2), with parameters $\alpha = 0.2^{+0.2}_{-0.1}$, $\beta = 1.4^{+0.3}_{-0.6}$ and $L_* = 10^{52.5\pm0.2}\,{\rm erg}\cdot{\rm s}^{-1}$. Wanderman and Piran (2010) have also concluded that the assumption of no luminosity function evolution with redshift can be accepted.

On the other hand, Lloyd-Ronning et al. (2002) have found that the average luminosity can be parametrized as $L \propto (1+z)^{1.4\pm\sim0.5}$, i.e. the luminosity function is redshift dependent. Further, Firmani et al. (2005) have also shown an evolving luminosity function. Salvaterra et al. (2012) have found strong evolution in luminosity or in density, in order to account for the observations of bright GRBs detected by the Swift satellite.

2.3.4 Intrinsic Correlations

It has been shown that many intrinsic quantities of the GRBs show intrinsic correlations. In this subsection I briefly describe some of them. Note, that $E_{\rm peak}$ is the peak energy in so-called $E^2N(E)$ spectrum (see eq. 4.1). In the paragraphs of this section this quantity is always in the rest frame of the burst.

Amati Relation

Amati et al. (2002) studied spectral and energetics properties of twelve GRBs detected by Beppo-SAX with determined redshifts and discovered a positive correlation between $E_{\rm iso}$ (in comoving energy interval $\langle 1, 10\,000\rangle$ keV) and $E_{\rm peak}$. The correlation can be expressed as

$$E_{\rm peak} \propto E_{\rm iso}^{0.52\pm0.06} \tag{2.4}$$

Yonetoku Relation

Yonetoku et al. (2004) studied the GRBs detected by the Beppo-SAX and BATSE satellite and derived a relation combining the $E_{\rm peak}$ and $L_{\rm iso}$, which is the peak luminosity in the rest frame of the GRB. The relation is concisely expressed as $L_{\rm iso} \propto E_{\rm peak}^{\mu}$. They have found that

$$\frac{L_{\rm iso}}{10^{52}\,{\rm erg}\cdot{\rm s}^{-1}} = 2.34^{+2.29}_{-1.76}\cdot 10^{-5}\left[\frac{E_{\rm peak}}{\rm keV}\right]^{2.0\pm0.2}. \tag{2.5}$$

Ghirlanda Relation

Ghirlanda et al. (2004) studied the sample of GRBs with measured redshifts and estimated jet opening angles from the achromatic break of the afterglow light curve. They found tight correlation between $E_{\rm peak}$ and collimation-corrected energy of the burst E_γ. The correlation has the form of a power law and can be written as

$$E_{\rm peak} \simeq 480 \left(\frac{E_\gamma}{10^{51}\,{\rm erg}} \right)^{0.7} \,{\rm keV}. \tag{2.6}$$

One can say that Ghirlanda relation is an improvement of the Amati relation, since it accounts for the jet opening angle.

Variability–Luminosity Relation

The variability V of the GRBs can be viewed as a measure of spikiness or smoothness of the light curves. Many definitions of V were proposed (Reichart et al. 2001; Fenimore and Ramirez-Ruiz 2000; Guidorzi et al. 2005). Schaefer (2007) has found a correlation between the luminosity $\left[{\rm erg}\cdot{\rm s}^{-1}\right]$ and the variability of the bursts in a form

$$\log(L) = 52.49 + 1.77 \log\left[\frac{V(1+z)}{0.02}\right]. \tag{2.7}$$

Lag–Luminosity Relation

One of the prompt emission properties is the spectral lag τ, defined shortly as the time delay between the soft and hard light curves of the burst. Schaefer (2007) has found a correlation between the luminosity $\left[{\rm erg}\cdot{\rm s}^{-1}\right]$ and τ. The correlation has a form of the power law,

$$\log(L) = 52.26 + 1.01 \log\left[\frac{\tau(1+z)^{-1}}{0.1\,{\rm s}}\right]. \tag{2.8}$$

The lag–luminosity relation is closely tied to the variability–luminosity relation (Schaefer et al. 2001).

2.4 Modern Observations (2010–2013)

In this section I shortly recapitulate some results from the last three years. Much effort has been spent to extract as much information as possible from a large sample (~ 700) of the GRBs detected by the Swift satellite. For a large fraction of them (~ 200), the redshift is determined. This is due to the fact, that the Swift satellite has been designed solely for the detection of the GRBs, with respect to maximizing the probability of the redshift measurement. Another advantage over the other satellites, is the low value of the threshold flux $\sim 0.4\,{\rm ph}\cdot{\rm s}^{-1}\cdot{\rm cm}^{-2}$. However, a complicated detection threshold

algorithm is very hard to model. The main disadvantage of the Swift satellite is a low energy band of the BAT instrument (15–150 keV).

The Fermi satellite has two great advantages: a wide energy range of the detectors, $\langle 10, 30\,000 \rangle$ keV, and a high spectral resolution, 256 channels. However, its current sensitivity is around $\sim 0.7\,\mathrm{ph} \cdot \mathrm{s}^{-1} \cdot \mathrm{cm}^{-2}$, approximately two times higher than that of the BAT instrument.

One may presume, that by combining the data acquired by both of the satellites, the amount of information hidden in the data is more than just an add-up. Virgili et al. (2012) studied the joint Swift/BAT-Fermi/GBM sample and suggested the importance of an energy-dependent temporal analysis of the GRBs. Cobb et al. (2010) proposed to use the OIR instrument suit on the Gemini south and Gemini north telescopes, to rapidly observe new GRBs, to fully unroll the potential of the Swift and Fermi satellites. One of the goals is to constrain the progenitors of the short GRBs, which are still unresolved.

Considering the Amati relation described in section 2.3.4, Butler et al. (2010) has shown that this tight correlation is strongly detector dependent. In spite of that, they concluded that there exists intrinsic correlation between E_{iso} and E_{peak}, but it has a large scatter. Similarly, Gruber (2012) reported that the correlation has larger scatter than that in eq. 2.4. They found that

$$E_{\mathrm{peak}} = 441^{+1840}_{-360} \left(\frac{E_{\mathrm{iso}}}{1.07 \cdot 10^{53}\,\mathrm{erg}} \right)^{0.55 \pm 0.10} \mathrm{keV}. \tag{2.9}$$

Wang et al. (2011) published also updated Amati relation, variability–luminosity and lag–luminosity correlations.

The Yonetoku relation has also been verified by a number of studies. Gruber (2012) have found the correlation between L_{iso} and E_{peak} in a form of

$$E_{\mathrm{peak}} = 667^{+295}_{-310} \left(\frac{L_{\mathrm{iso}}}{4.97 \cdot 10^{53}\,\mathrm{erg} \cdot \mathrm{s}^{-1}} \right)^{0.48 \pm 0.01} \mathrm{keV}. \tag{2.10}$$

However, Wang et al. (2011) analyzed a combined sample of 116 long GRBs (31 pre-Swift and 85 Swift) and have found a different power law index $\mu \simeq 1.4$, instead of the original index $\mu \simeq 2$ found by Yonetoku et al. (2004). The new Yonetoku relation has a form

$$\frac{L_{\mathrm{iso}}}{10^{52}\,\mathrm{erg} \cdot \mathrm{s}^{-1}} = 1.28^{+0.17}_{-0.13} \left[\frac{E_{\mathrm{peak}}}{300\,\mathrm{keV}} \right]^{1.40 \pm 0.12}. \tag{2.11}$$

Further, Zhang et al. (2012) derived yet one more different value of the power law index $\mu \simeq 1.7$, which is marginally consistent with Yonetoku's value within the one σ level.

Considering the classification of the GRBs into groups, Horváth et al. (2012) analyzed the latest Fermi GRB catalogue. They used statistical method of PCA and

Multiclustering, which revealed three groups. However, additional analysis is needed to rule out the possibility that the splitting is a mathematical by-product. Further, Řípa et al. (2012) studied a sample of 427 GRBs detected by the Reuven Ramaty High Energy Solar Spectroscopic Imager satellite (RHESSI) and also found three groups of GRBs. They concluded that the group of intermediate-duration bursts differs from the group of lGRB and has similar properties as the group of sGRB.

Recently, Xu and Huang (2012) found a new tight three-parameter correlation between the end time of the plateau phase in the afterglow (in the rest frame) $T_{\rm a}$, the X-ray luminosity $L_{\rm X}$ and the isotropic gamma-ray energy release $E_{\rm iso}$, which has a form

$$L_{\rm X} \propto T_{\rm a}^{-0.87\pm0.09} E_{\rm iso}^{0.88\pm0.08}. \tag{2.12}$$

Chapter 3

The FERMI Satellite

The FERMI Gamma-ray Space Telescope, formerly known as the Gamma-ray Large Area Space Telescope (GLAST), is the latest space observatory dedicated to the study of the Universe with respect to the high energy part of the electromagnetic spectrum. Aside from deepening the knowledge of already known astronomical phenomena, FERMI is expected to make also new revolutionary scientific discoveries. This is due to the fact that the onboard instruments has unprecedented energy coverage and sensitivity.

In this Chapter I briefly describe the onboard instruments and the data products. Sections 3.2 and 3.3 are drawn from the some publications (Atwood et al. 2009; Meegan et al. 2009; Paciesas et al. 2012). For more detailed information look into them.

3.1 Overview

The FERMI mission is a joint collaboration of NASA, the United States Department of Energy and government agencies of France, Italy, Japan and Sweden[1]. The FERMI satellite was launched on 11 June 2008 and was designed to have a five-year lifetime. The mission objectives are to explore the most extreme environments in the Universe, to search for signs of new physics, to shed light on a mysterious dark matter, origins of cosmic rays, and last but not least, to help crack the puzzles of the GRBs.

The principal instrument onboard the FERMI satellite is the Large Area Telescope (LAT) and the secondary instrument is the Gamma-ray Burst Monitor (GBM). Together they provide an energy band ranging from 8 keV to 300 GeV. In Figure 3.1 the schema of the FERMI satellite is shown. In next subsections a brief description of these instruments will be given.

[1] http://www-glast.stanford.edu/

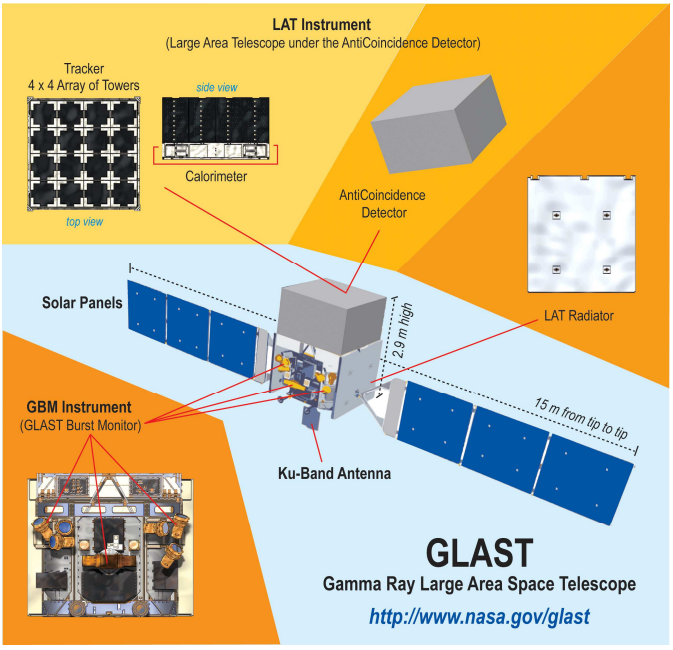

FIGURE 3.1: The schematic description of the Fermi satellite. (Credit: http://fermi.sonoma.edu/multimedia/gallery/)

3.2 LAT

After a successful mission of the Compton Gamma Ray Observatory (CGRO), which was the first space observatory designed to detect the high energy photons (from 20 keV to 30 GeV), the development of an instrument that is more sensitive and has a wider energy coverage began. The LAT is superior in every way in comparison with the previous high energy instrument EGRET aboard the CGRO. The scientific objectives of the LAT are, a) determining the origins of the diffuse emission and the nature of the unidentified sources detected by EGRET, b) understanding the mechanism of particle acceleration that produces the gamma photons, c) explore the high energy part of the GRBs' spectra, d) searching for the signs that help in understanding the dark matter, and e) explore the early universe Atwood et al. (2009).

In Table 3.1 the main scientific performance, compared with the EGRET instrument, is summarized. For detailed description see Atwood et al. (2009).

The LAT is a pair-conversion telescope that measures the directions, energies and arrival times of gamma-rays. It is composed of a 4x4 array of identical towers supported by a low-mass aluminium grid structure. Each tower (40x40 cm^2) consists of a precision converter-tracker, calorimeter and data acquisition module. In order to filter out the massive flux of cosmic rays, which is a houndred times larger than the flux of the gamma-rays, a segmented anticoincidence detector (ACD) covers the tracker array. A programable trigger and data acquisition system utilizes prompt signals from tracker, calorimeter and ACD, to achieve a self-triggering capability. The characteristic of the

Quantity	LAT	EGRET
Energy Range	20 MeV – 300 GeV	20 MeV – 30 GeV
Peak Effective Area[a]	$> 8000\,\mathrm{cm}^2$	$> 1500\,\mathrm{cm}^2$
Field of View (FoV)	> 2 sr	0.5 sr
Angular Resolution[b]	$< 3.5^\circ$ (100 MeV) $< 0.15^\circ$ (> 10 GeV)	5.8° (100 MeV)
Energy Resolution[c]	$< 10\,\%$	$10\,\%$
Deadtime per Event	$< 100\,\mu$s	100 ms
Source Location Determination[d]	$< 0.5'$	$15'$
Point Source Sensitivity[e]	$< 6 \cdot 10^{-9}\,\mathrm{cm}^{-2} \cdot \mathrm{s}^{-1}$	$\sim 10^{-7}\,\mathrm{cm}^{-2} \cdot \mathrm{s}^{-1}$

TABLE 3.1: A brief summary of the scientific performance of the LAT instrument in comparison with the CGRO/EGRET instrument. The LAT is superior in every parameter that is listed in the table. [a] After background rejection. [b] Single photon, 68% containment, on axis. [c] 1-σ, on axis. [d] 1-σ radius, flux $10^{-7}\,\mathrm{cm}^{-2} \cdot \mathrm{s}^{-1}$ (> 100 MeV), high $|b|$. [e] $>$ 100 MeV, at high $|b|$, for exposure of one-year all sky survey, photon spectral index -2.
(Credit: fermi.gsfc.nasa.gov/science/instruments/table1-1.html)

detected gamma-ray is, a) no signal in the ACD, b) more than one track starting from the same location within the volume of the tracker, and 3) an electromagnetic shower in the calorimeter[2].

3.3 GBM

The GBM was constructed mainly for detection of GRBs. It was designed to have similar characteristics as the CGRO/BATSE instrument, but with higher resolution in time and photon energy. The primary scientific objective of the GBM is the joint analysis of spectra and time histories of GRBs observed by both the GBM and the LAT (Meegan et al. 2009). Further objectives are, a) to provide near-real time burst locations utilized by the LAT and ground-based observers, b) study of the rest of the sources that triggers the GBM (solar flares, terrestrial gamma flashes and soft gamma repeaters).

The GBM consists of Data Processing Unit (DPU), Power Box, 12 thalium activated sodium iodide (NaI(Tl)) scintillation detectors and two bismuth germanate (BGO) scintillation detectors. The NaI(Tl) detectors measure the low-energy part of the GRB' spectrum and are used to determine a direction to the source. The orientation of the 12 detectors is such that the position of the burst could be determined by the technique of the relative count rates. The BGO detectors measure the high-energy part of the spectrum. They are located at opposite sides of the spacecraft so that any

[2] fermi.gsfc.nasa.gov/science/instruments/lat.html

burst (not occulted by the Earth) could be detected at least with one of the them. In Figure 3.2 the locations and orientations of the detectors are illustrated.

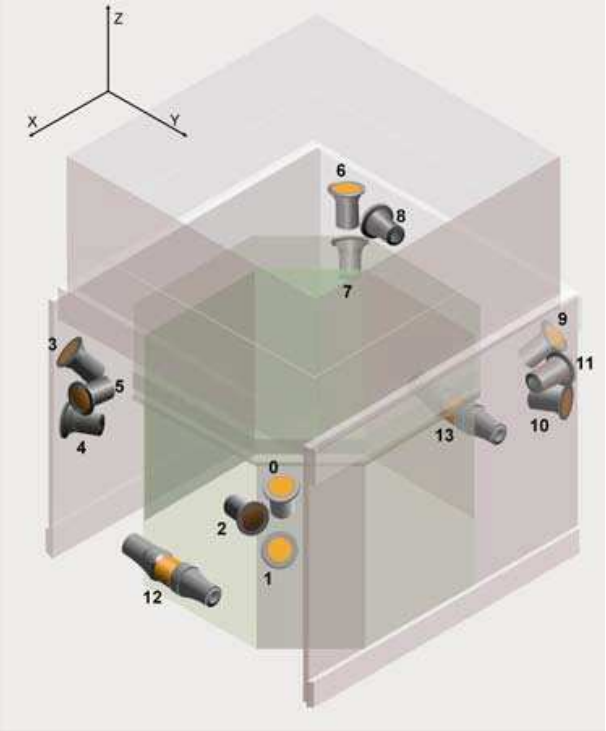

FIGURE 3.2: Locations and orientations of the GBM detectors. (Credit: Meegan et al. (2009))

Table 3.2 and 3.3 summarizes the specifications and current performance compared with the BATSE instrument, respectively.

3.3.1 Data types of the GBM

The GBM Flight Software (FSW) on DPU continuously monitors all the detectors and produces three types of science data packets: CTIME, CSPEC and TTE.

The Continuous Time (CTIME) data consists of accumulated spectra with 8 channel resolution and have nominally 256 ms time resolution (configurable from 64 ms to 1024 ms). The Continuous Spectroscopy (CSPEC) data consists of the accumulated spectra with 128 channel resolution and have nominally 4096 ms time resolution (configurable from 1024 ms to 32768 ms). Both the accumulation intervals (i.e. time resolutions) for CTIME and CSPEC are controlled by the FSW. The TTE data consists of individual detector events. Each event has a detector number, time tag (with accuracy $\sim 10\,\mu s$, but resolution $2\,\mu s$) and energy (128 channels). The TTE data are stored in a ring buffer with the capacity of 512,000 events (holding the data for $\sim 30\,$s) (Meegan et al. (2009)).

	GBM	BATSE
Total Mass	115 kg	850 kg
	Low-Energy Detectors	Large Area Detectors
Material	NaI	NaI
Number	12	8
Area	126 cm^2	2025 cm^2
Thickness	1.27 cm	1.27 cm
Energy Range	8 keV – 1 MeV	25 keV – 1.8 MeV
	High-Energy Detectors	Spectroscopy Detectors
Material	BGO	NaI
Number	2	8
Area	126 cm^2	126 cm^2
Thickness	12.7 cm	7.62 cm
Energy Range	150 keV – 40 MeV	30 keV – 10 MeV

TABLE 3.2: The characteristics of the FERMI/GBM instrument in comparison with the CGRO/BATSE instrument. The GBM detectors cover a wider energy range and have a smaller collection area.
(Credit: gammaray.msfc.nasa.gov/gbm/instrument/description/character.html)

Quantity	GBM	BATSE
Energy Range	$\sim$ 8 keV – 30 MeV	$\sim$ 25 keV – 10 MeV
Field of View	9.5 sr	4π sr
Energy Resolution[a]	$< 10\%$	$< 10\%$
Dead time per Event	$< 2\mu$s	
Burst Sensitivity[b]	$\sim 0.7\,\mathrm{ph \cdot cm^{-2} \cdot s^{-1}}$	$\sim 0.2\,\mathrm{ph \cdot cm^{-2} \cdot s^{-1}}$
Onboard GRB Location	$< 15^\circ$ in 1.8 s	$\sim 25^\circ$
Time resolution	2 μs	2 ms

TABLE 3.3: A brief summary of the current scientific performance of the FERMI/GBM in comparison with the CGRO/BATSE. The current sensitivity of the GBM detectors is roughly three times higher than that of the BATSE detectors. [a] 1-σ, 0.1–1 MeV. [b] 50–300 keV.
(Credit: fermi.gsfc.nasa.gov/science/instruments/table1-2.html & gammaray.msfc.nasa.gov/gbm/instrument/description/character.html)

In normal mode, the GBM continuously transmits the CTIME and CSPEC data with nominal resolution. When a trigger occurs, the FSW speeds up the time resolution to 64 ms (for CTIME data) and 1024 s (for CSPEC data). The TTE data are transmitted continuously with CTIME and CSPEC data for $\sim$ 300 s. The TTE data in the ring buffer are frozen and transmitted later, providing $\sim$ 30 s of high resolution pre-trigger data (Meegan et al. 2009).

3.3.2 Triggers

The GBM enters the trigger mode, if two or more NaI(Tl) detectors have an increase rate above a specified threshold. An increase rate is monitored by the FSW and the threshold is specified in units of standard deviation σ_{br} of the background rate. The detection threshold algorithm works on multiple timescales (from 16 ms to 16384 ms) and in various energy ranges ($>$ 100 keV, $>$ 300 keV, 25–50 keV and 50–300 keV). However, only the algorithms that work in 50–300 keV energy range are currently enabled, since the algorithms working in different energy ranges never triggered a burst that had not been triggered by the "50–300 keV" algorithms (Paciesas et al. 2012).

Chapter 4

Definition of the Samples

In this part of the thesis I will focus on the process of acquiring the relevant data and on the methodology, which I will use for the selection of the particular GRBs. A measured redshift provides a strong way to determine the intrinsic properties of the GRBs. Hence, having a well determined redshift, is extremely useful. Therefore, in this Chapter a sample of GRBs, having measured redshifts, will be defined together with two other samples.

4.1 Definition of the GRBall, GRBz and GRBtrun Samples

The data will be acquired from the Fermi GBM Burst Catalog[1] (FERMIGBRST), which is an official product from the Fermi GBM Science Team. By selecting the bursts, matching the criteria $T_{90} > 2$ s with known spectral parameters, I will obtain a sample of 397 bursts. This sample will be denoted as "GRBall". The period, which covers the GRBall sample, starts on July 14th 2008 and ends on July 9th 2010. From that sample, the bursts having determined redshifts will be chosen. This is done by comparing the GRBs which are both in Greiner table[2] and in GRBall. This procedure yields a sample of 29 bursts, which is a subset of the GRBall sample.

The burst denoted by GRB090423330 is one of the most distant object, whose redshift has ever been measured. Due to its extreme distance, the measured T_{90} differs considerably from the topical T_{90} in the comoving frame of reference (denoted as $T_{90\mathrm{cf}}$). One has $T_{90} = 7.168$ s. By using the standard cosmological formula $T_{90\mathrm{cf}} = T_{90}/(1+z)$, it follows $T_{90\mathrm{cf}} = 0.774$ s. Due to the intrinsic properties, discovered by Fenimore et al. (1995) and in depth studied by Mészáros and Mészáros (1996), another prescription for $T_{90\mathrm{cf}}$ may be used, namely $T_{90\mathrm{cf}} = T_{90}/(1+z)^{0.6}$ yielding $T_{90\mathrm{cf}} = 1.89$ s. In any case

[1] https://heasarc.gsfc.nasa.gov/W3Browse/fermi/fermigbrst.html

[2] Although Greiner table is a subjective work of Dr. Greiner, it has a high reliability and is heavily referenced. http://www.mpe.mpg.de/∼jcg/grbgen.html

it is likely that this burst belongs to the family of the short GRBs. Therefore I will exclude this burst from the sample with known redshifts. Now 28 bursts remain after this exclusion and they will be denoted as "GRBz" sample. None of the 28 bursts in the GRBz sample does have $T_{90\mathrm{fc}}$ below 2 s. Hence, it is likely that all of them belong to the family of the long GRBs. For the sake of consistency, the burst GRB090423330 is not excluded from the GRBall sample.

Additionally, I also create a sample "GRBtrun", which is defined as a group of the GRBs that are in the GRBall sample except for the GRBs in the GRBz sample (GRBall = GRBtrun ∪ GRBz). This sample will also be used in the analyses, because GRBtrun and GRBz samples are obviously independent.

The physical quantities describing GRBall will be denoted with the superscript "all". Physical quantities describing GRBz will be denoted with the superscript "z".

4.2 Description of the Parameters

In this section I will provide the definitions of the quantities and abbreviations used later on in the thesis. For completeness, quantities described in section 2.2 will be described below, some with abbreviations.

4.2.1 Name

The name I used to designate GRB is in the form GRByymmddfff, where fff is the fraction of the day as described in FERMIGBRST. The designations of the GRBs in GRBz sample are listed in the first column of Table 4.1. The designations of the burst in GRBall sample are listed in Appendix D.

4.2.2 T_{90}

T_{90} [s] is the duration, during which 90 % of the burst fluence was accumulated. The start of the T_{90} interval is the time at which 5 % of the total fluence has been detected, and the end of the T_{90} interval is the time at which 95 % of the total fluence has been detected. Values of T_{90} with errors for the GRBz sample are listed in the second column of Table 4.1.

4.2.3 Fluence F

Fluence [$\mathrm{erg \cdot cm^{-2}}$] is the flux integrated over T_{90} time of the burst. It can be defined over an arbitrary energy range. It is usually computed in the reliable energy range of the detector (e.g. 50–300 keV for BATSE satellite[3]). In FERMIGBRST the energy intervals of 50–300 keV and 10–1000 keV are used. The fluence can also be computed

[3] www.batse.msfc.nasa.gov/batse/

using the spectral function fitted on the time integrated spectra of the GRB. Fluence computed this way is more reliable than the fluence computed crudely using 8 channel data[4] (see Chapter 3). From now on, fluence obtained by using the best fitted spectral function in 10–1000 keV energy interval will be designated as $F_{\rm best}$ and in 50–300 keV energy interval as $F_{\rm bbest}$. Definitions of the spectral functions are found in the section 4.2.5. Values of $F_{\rm best}$ and $F_{\rm b,best}$, respectively, with their errors, for the GRBz sample are listed in the third and fourth column of the Table 4.1.

4.2.4 Peak flux P

Peak flux $[\mathrm{ph}\cdot\mathrm{s}^{-1}\cdot\mathrm{cm}^{-2}]$ is the maximum photon flux over the duration of the burst on a defined time scale and in a defined energy interval. In FERMIGBRST peak fluxes are computed in energy intervals 50–300 keV and 10–1000 keV. Time scales are 64, 256 and 1024 ms. $P_{\rm [timescale]}$ will designate peak flux in 10–1000 keV and $P_{\rm b[timescale]}$ will designate peak flux in energy interval 50–300 keV. As for the fluence, more accurate peak fluxes are obtained by using the best fitted spectral functions. Peak fluxes obtained by this way will be denoted by subscript "best". Values of $P_{\rm b,best[1024]}$ with their errors, actually computed from the spectral functions for the GRBz sample, are listed in fifth column of Table 4.1. For details of error estimation see section 5.4.

4.2.5 Spectra

Spectral functions used for fitting the spectrum over the duration of the burst and over the time range of the peak flux of the burst are the BAND, PLAW, COMP and SBPL models, respectively. They are described as follows:

BAND model

This is the most widely used GRB empirical model introduced by Band et al. (1993). Its functional form is

$$N_{\rm BAND}(E)=\begin{cases} A\left(\frac{E}{100\ \mathrm{keV}}\right)^{\alpha}\exp\left(-\frac{(\alpha+2)E}{E_{\rm peak}}\right) & \mathrm{if}\, E<\frac{(\alpha-\beta)E_{\rm peak}}{\alpha+2},\\ A\left(\frac{E}{100\ \mathrm{keV}}\right)^{\beta}\exp(\beta-\alpha)\left(\frac{(\alpha-\beta)E_{\rm peak}}{100\ \mathrm{keV}(\alpha+2)}\right)^{\alpha-\beta} & \mathrm{if}\, E\geq\frac{(\alpha-\beta)E_{\rm peak}}{\alpha+2}, \end{cases} \tag{4.1}$$

where the amplitude A is in units $\left[\mathrm{ph}\cdot\mathrm{s}^{-1}\cdot\mathrm{cm}^{-2}\cdot\mathrm{keV}^{-1}\right]$, α is a low-energy index, β is a high-energy index and $E_{\rm peak}$ in [keV] is a so-called $E^2N_{\rm BAND}(E)$ peak energy. The $E^2N_{\rm BAND}(E)$ spectrum represents the total energy flux per energy band.

[4] https://heasarc.gsfc.nasa.gov/W3Browse/fermi/fermigbrst.html

PLAW model

Power law model – with two free parameters – is the simplest one among the four models. It is

$$N_{\mathrm{PLAW}}(E) = A\left(\frac{E}{E_{\mathrm{piv}}}\right)^{\lambda}, \tag{4.2}$$

where A is the amplitude in units $\left[\mathrm{ph}\cdot\mathrm{s}^{-1}\cdot\mathrm{cm}^{-2}\cdot\mathrm{keV}^{-1}\right]$, λ is a spectral index and E_{piv} is the pivot energy set to 100 keV for every spectrum (Kaneko et al. 2006).

COMP model

Comptonized model is a low-energy power law with an exponential high-energy cutoff, written as

$$N_{\mathrm{COMP}}(E) = A\left(\frac{E}{100\ \mathrm{keV}}\right)^{\alpha}\exp\left(-\frac{(\alpha+2)E}{E_{\mathrm{peak}}}\right), \tag{4.3}$$

where A is the amplitude in units $\left[\mathrm{ph}\cdot\mathrm{s}^{-1}\cdot\mathrm{cm}^{-2}\cdot\mathrm{keV}^{-1}\right]$, α is a low-energy power law index (Kaneko et al. 2006).

SBPL model

Smoothly broken power law is the last model used to fit the spectra. Its functional form is as follows

$$N_{\mathrm{SBPL}}(E) = A\left(\frac{E}{E_{\mathrm{piv}}}\right)^{b} 10^{a-a_{\mathrm{piv}}}, \tag{4.4}$$

where

$$\begin{aligned} a_{\mathrm{piv}} &= m\Delta\ln\left(\tfrac{\mathrm{e}^{q}+\mathrm{e}^{-q}}{2}\right), & a &= m\Delta\ln\left(\tfrac{\mathrm{e}^{q_{\mathrm{piv}}}+\mathrm{e}^{-q_{\mathrm{piv}}}}{2}\right), \\ q &= \tfrac{\log(E/E_b)}{\Delta}, & q_{\mathrm{piv}} &= \tfrac{\log(E_{\mathrm{piv}}/E_b)}{\Delta}, \\ m &= \tfrac{\lambda_2-\lambda_1}{2}, & b &= \tfrac{\lambda_1-\lambda_2}{2}. \end{aligned}$$

Amplitude A is in units $\left[\mathrm{ph}\cdot\mathrm{s}^{-1}\cdot\mathrm{cm}^{-2}\cdot\mathrm{keV}^{-1}\right]$, E_{piv} is set to 100 keV. λ_1 and λ_2 are the low- and high-energy power law indexes, respectively. E_b in unit [keV] is the break energy. Δ denotes the break energy scale fixed at 0.3 for all the spectra which describes the transitions between the high and low energy parts of the spectrum (Kaneko et al. 2006).

4.3 Selection of the Parameters

The GRBz sample is the main set studied in this thesis. GRBall and GRBtrun serve for comparison and estimation of possible biases. All selected parameters, which will

be used in the following two Chapters, are shown in Appendix C. Values are not shown since one can easily access them from the FERMIGBRST database[5].

Designation	T_{90} [s]	$F_{\rm best}$ $\left[10^{-5}\,\frac{\rm erg}{\rm cm^2}\right]$	$F_{\rm b,best}$ $\left[10^{-5}\,\frac{\rm erg}{\rm cm^2}\right]$	$P_{\rm b,best}$ $\left[10^{-7}\,\frac{\rm erg}{\rm s\cdot cm^2}\right]$
GRB080804972	24.7±1.4	1.12±0.03	0.513±0.011	$3.66^{+0.11}_{-0.69}$
GRB080810549	107±15	1.68±0.03	0.617±0.013	$3.10^{+0.16}_{-0.61}$
GRB080905705	105±6.8	0.19±0.02	0.118±0.007	$1.14^{+0.14}_{-0.14}$
GRB080916009	62.9±0.8	8.38±0.10	3.342±0.028	$14.81^{+0.34}_{-0.56}$
GRB080916406	46.3±7.1	1.28±0.03	0.550±0.013	$5.16^{+0.17}_{-0.65}$
GRB080928628	14.3±4.0	0.20±0.01	0.077±0.005	$1.14^{+0.16}_{-0.14}$
GRB081008832	150±12	0.73±0.05	0.398±0.014	$2.14^{+0.10}_{-0.94}$
GRB081121858	41.9±8.5	1.48±0.04	0.762±0.018	$6.9^{+0.1\dagger}_{-4.4}$
GRB081221681	29.6±0.4	3.08±0.05	1.776±0.018	$17.11^{+0.47}_{-0.56}$
GRB081222204	18.8±2.3	1.19±0.03	0.629±0.010	$9.64^{+0.24}_{-0.60}$
GRB090102122	26.6±0.8	3.26±0.06	1.508±0.016	$13.88^{+0.29}_{-0.46}$
GRB090113778	17.4±3.2	0.18±0.01	0.068±0.003	$3.01^{+0.10}_{-0.63}$
GRB090323002	135±1.4	12.6±0.1	5.270±0.034	$13.45^{+0.26}_{-0.47}$
GRB090328401	61.6±1.8	5.01±0.05	2.091±0.018	$17.10^{+0.30}_{-0.47}$
GRB090424592	14.1±0.2	4.67±0.05	2.599±0.021	$64.58^{+0.57}_{-0.81}$
GRB090516353	123±2.8	2.26±0.08	1.104±0.025	$2.13^{+0.18}_{-0.17}$
GRB090519881	74.1±5.1	0.47±0.03	0.138±0.009	$0.91^{+0.14}_{-0.13}$
GRB090618353	112±1.0	25.1±0.1	13.45±0.065	$60.2^{+1.0}_{-1.1}$
GRB090902462	19.3±0.2	27.9±0.1	8.767±0.027	$61.57^{+0.85}_{-0.79}$
GRB090926181	13.7±0.2	15.5±0.1	7.358±0.028	$88.26^{+0.72}_{-0.88}$
GRB090926914	55.5±7.6	0.77±0.01	0.529±0.014	$2.84^{+0.07}_{-0.88}$
GRB091003191	20.2±0.3	3.52±0.05	1.594±0.017	$37.00^{+0.48}_{-0.80}$
GRB091020900	24.2±7.9	0.80±0.04	0.413±0.012	$4.22^{+0.19}_{-0.19}$
GRB091024372	93.9±5.2	1.55±0.07	0.577±0.031	$2.33^{+0.37}_{-0.37}$
GRB091024380	450±2.3	3.92±0.14	2.314±0.044	$3.62^{+0.40}_{-0.44}$
GRB091127976	8.7±0.5	1.89±0.02	0.734±0.008	$26.21^{+0.37}_{-0.37}$
GRB091208410	12.4±5.0	0.79±0.02	0.337±0.010	$13.93^{+0.25}_{-0.93}$
GRB100414097	26.4±2.0	9.21±0.06	3.109±0.020	$21.81^{+0.34}_{-0.56}$

TABLE 4.1: Characteristics of the GRBz sample. Quantities T_{90}, $F_{\rm best}$ and $F_{\rm b,best}$, with their errors, are taken from the FERMIGBRST database. Quantity $P_{\rm b,best}$ denotes the peak flux on 1.024 ms timescale in energy range $\langle 50, 300\rangle$ keV, and it was computed by using the spectral parameters of the best fitted spectral function over the peak flux of the burst. The errors of $P_{\rm b,best}$ are computed by Monte Carlo (MC) technique briefly described in section 5.4.
†This error estimate is not reliable (see section 5.4).

[5]https://heasarc.gsfc.nasa.gov/W3Browse/fermi/fermigbrst.html

Chapter 5

The Analysis of the GRBz Sample

In this Chapter I describe the computation of the intrinsic properties of GRBs for the GRBz sample. Due to the fact that GRBs lie at cosmological distances, the computation of their intrinsic characteristics from the measured quantities, like duration T_{90}, fluence F and peak flux P, is not trivial. Measured quantities depend on the progenitor's characteristics and on its redshift. Due to the dependence on the redshift, the type of the Universe model plays a role in these computations. Further, the empirical relation discovered by Fenimore and Bloom (1995), studying BATSE data, plays an important role too.

Another important aspect of the cosmological formulas is the necessity to use k-correction (Bloom et al. 2001), when the total emitted energy in a comoving frame of reference is asked for an energy range $\langle E_1, E_2 \rangle$. The knowledge of the redshift z is a necessary condition for the computation of the k-correction. Equally important is the knowledge of the spectra of GRBs. The GRBs, which I selected (GRBz sample), meet both criteria (see the previous Chapter).

5.1 Calculation of $E_{\rm iso}$ and $L_{\rm iso}$

5.1.1 On the Theory of the $E_{\rm iso}$, $L_{\rm iso}$ and k-Correction

If we want to obtain the intrinsic properties of GRBs, we need to find a way of determining them. Assuming an ideal detector, that can detect all the radiation at all the wavelengths, the following cosmological formulas, for the measured $F_{\rm bol}$ in units of $\left[\mathrm{erg} \cdot \mathrm{cm}^{-2}\right]$ and $P_{\rm bol}$ in units of $\left[\mathrm{erg} \cdot \mathrm{s}^{-1} \cdot \mathrm{cm}^{-2}\right]$,

$$E_{\rm iso,bol} = \frac{4\pi D_{\rm l}^2}{1+z} F_{\rm bol} \tag{5.1}$$

and

$$L_{\mathrm{iso,bol}} = 4\pi D_{\mathrm{l}}^2 P_{\mathrm{bol}}, \tag{5.2}$$

may be used to calculate the bolometric energy $E_{\mathrm{iso,bol}}$, in units of [erg], and the bolometric luminosity $L_{\mathrm{iso,bol}}$, in units of $\left[\mathrm{erg}\cdot\mathrm{s}^{-1}\right]$. F_{bol} is a measured bolometric fluence, P_{bol} is a measured bolometric peak flux and D_{l} is the luminosity distance[1] of the source at redshift z. Subscript "iso" denotes the assumption that the source radiates isotropically.

Because every detector has a limited energy range, it is almost impossible to have F_{bol} and P_{bol}. What the detector can measure is the fluence $F_{\langle e_1,e_2\rangle}$ and the peak flux $P_{\langle e_1,e_2\rangle}$ in its energy band $\langle e_1, e_2\rangle$. If the spectrum of the burst in this energy band is known, it is possible to derive the quantity $E_{\langle E_1,E_2\rangle}$, which is the isotropic equivalent energy radiated by the source in the arbitrary source frame energy range $\langle E_1, E_2\rangle$. The quantity $L_{\langle E_1,E_2\rangle}$, which is the peak luminosity radiated by the source in the arbitrary source frame energy range $\langle E_1, E_2\rangle$, is calculated similarly. Essential assumption is that a fitted spectral function should also describe the spectrum outside the energy range of the detector $\langle e_1, e_2\rangle$. Corresponding equations for $F_{\langle e_1,e_2\rangle}$ in units of $\left[\mathrm{erg}\cdot\mathrm{cm}^{-2}\right]$ and $P_{\langle e_1,e_2\rangle}$ in units of $\left[\mathrm{erg}\cdot\mathrm{s}^{-1}\cdot\mathrm{cm}^{-2}\right]$ are

$$E_{\langle E_1,E_2\rangle} = \frac{4\pi D_{\mathrm{l}}^2}{1+z} F_{\langle e_1,e_2\rangle} k_E \tag{5.3}$$

and

$$L_{\langle E_1,E_2\rangle} = 4\pi D_{\mathrm{l}}^2 P_{\langle e_1,e_2\rangle} k_L, \tag{5.4}$$

where k_{E} and k_{L} are the k-corrections of isotropic equivalent energy and luminosity, respectively. They are defined as

$$k_{\mathrm{E}}(e_1,e_2,E_1,E_2,z,\phi) = \frac{\int_{E_1/(1+z)}^{E_2/(1+z)} E\phi_{\mathrm{E}}(E)\mathrm{d}E}{\int_{e_1}^{e_2} E\phi_{\mathrm{E}}(E)\mathrm{d}E} \tag{5.5}$$

and

$$k_{\mathrm{L}}(e_1,e_2,E_1,E_2,z,\phi) = \frac{\int_{E_1/(1+z)}^{E_2/(1+z)} E\phi_{\mathrm{L}}(E)\mathrm{d}E}{\int_{e_1}^{e_2} E\phi_{\mathrm{L}}(E)\mathrm{d}E}, \tag{5.6}$$

where $\phi(E)$ is the spectral function, subscript "E" denotes the average spectrum during the whole duration of the burst; subscript "L" denotes the spectrum derived during the

[1] Throughout the thesis I assume a widely accepted cosmological model ΛCDM, with $H_0 = 70\ \mathrm{km}\cdot\mathrm{s}^{-1}\cdot\mathrm{Mpc}^{-1}, \Omega_M = 0.3, \Omega_\Lambda = 0.7$.

time range of the peak flux. In derivation of $E_{\langle E_1,E_2\rangle}$ I adopted the method of Bloom et al. (2001).

Consider the eq. 5.1 and suppose we know the fluences and redshifts of randomly chosen GRBs. After rewriting the eq. 5.1 to a more convenient form of

$$F_{\rm bol} = c(z) E_{\rm iso,bol}\,, \tag{5.7}$$

where $c(z) = (1+z)/4\pi D_{\rm l}^2$, we may test the independence of $c(z)$ and $E_{\rm iso,bol}$. Assuming the log–normal distribution of $F_{\rm bol}$, we may use the formula

$$\sigma^2_{\log F_{\rm bol}} = \sigma^2_{\log c(z)} + \sigma^2_{\log E_{\rm iso,bol}} + 2\rho_{\rm bol}\sigma_{\log c(z)}\sigma_{\log E_{\rm iso,bol}}, \tag{5.8}$$

where σ is the dispersion for the given quantity denoted by the subscript and $\rho_{\rm bol}$ is the correlation coefficient. If there is no correlation between $c(z)$ and $E_{\rm iso,bol}$ then $\rho_{\rm bol}$ is zero and the equation reduces to the one introduced by Mészáros et al. (2006). Generally, it holds $-1 \leq \rho_{\rm bol} \leq 1$.

With a similar line of reasoning we obtain the equations rewritten for given energy ranges $\langle E_1, E_2\rangle$ and $\langle e_1, e_2\rangle$ as follows

$$F_{\langle e_1,e_2\rangle} = \frac{c(z)}{k_{\rm E}(z)} E_{\langle E_1,E_2\rangle}\,, \tag{5.9}$$

and

$$\sigma^2_{\log F_{\langle e_1,e_2\rangle}} = \sigma^2_{\log[c(z)/k_{\rm E}(z)]} + \sigma^2_{\log E_{\langle E_1,E_2\rangle}} + 2\rho\sigma_{\log[c(z)/k_{\rm E}(z)]}\sigma_{\log E_{\langle E_1,E_2\rangle}}. \tag{5.10}$$

I will calculate the values of $\sigma_{\log F_{\langle e_1,e_2\rangle}}, \sigma_{\log[c(z)/k_{\rm E}(z)]}, \sigma_{\log E_{\langle E_1,E_2\rangle}}$ and ρ for both of the fluences $F_{\rm best}$ and $F_{\rm b,best}$. For comparison, I will compute these values by neglecting the k-correction, which effectively means that I will compute the $E_{\langle E_1,E_2\rangle}$ in different source frame energy range $\langle E_1, E_2\rangle$ for every GRB, depending on the redshift of the burst.

For computation of the $k_{\rm E}$ the shape of the spectral function $\phi(E)$ must be known. The spectrum was fitted by four spectral functions: BAND (eq. 4.1), PLAW (eq. 4.2), COMP (eq. 4.3) and SBPL (eq. 4.4). The k-correction for a particular GRB will be computed by using the best fitted spectral function over the duration of the burst.

The estimation of the $\sigma_{\log F_{\rm best}}$ and $\sigma_{\log F_{\rm b,best}}$ is straightforward[2]. To estimate the $\sigma_{\log[c(z)/k_{\rm E,best}(z)]}, \sigma_{\log[c(z)/k_{\rm E,b,best}(z)]}, \sigma_{\log E_{\langle E_1,E_2\rangle,\rm best}}, \sigma_{\log E_{\langle E_1,E_2\rangle,\rm b,best}}, \rho_{\rm best}$ and $\rho_{\rm b,best}$ I use the statistical method of Maximum Likelihood Estimation (MLE) assuming the

[2]For definition of $F_{\rm best}$ and $F_{\rm b,best}$ look in the section 4.2.3.

bivariate log-normal distribution in the form (for details of MLE see Appendix D)

$$\Xi(\vec{r}\,|\,\vec{s}\,) = \frac{1}{2\pi\sigma_x\sigma_y\sqrt{1-\rho^2}} \exp\left\{-\frac{1}{2(1-\rho^2)}\left[\left(\frac{x-x_0}{\sigma_x}\right)^2 + \left(\frac{y-y_0}{\sigma_y}\right)^2 - 2\rho\frac{(x-x_0)(y-y_0)}{\sigma_x\sigma_y}\right]\right\}, \tag{5.11}$$

$$\text{where } \vec{r} = (x, y) = \left(\log\left[c(z)/k_E(z)\right], \log\left[E_{\langle E_1,E_2\rangle}\right]\right)$$

$$\text{and } \vec{s} = (\sigma_x, \sigma_y, x_0, y_0, \rho) = \left(\sigma_{\log[c(z)/k_E(z)]}, \sigma_{\log\left[E_{\langle E_1,E_2\rangle}\right]}, \mu_{\log[c(z)/k_E(z)]}, \mu_{\log\left[E_{\langle E_1,E_2\rangle}\right]}, \rho\right).$$

5.1.2 Determined Values of $E_{\rm iso}$ and $L_{\rm iso}$ with and without k-Correction

In this subsection the calculation of $E_{\rm iso}$ and $L_{\rm iso}$ with and without the k-correction will be presented. The energy range $\langle E_1, E_2\rangle$ in which the isotropic equivalent energy and isotropic luminosity is computed is set to $\langle 0.1, 10\,000\rangle$ keV. Quantities computed in this range will be denoted in the text below as "effective bolometric".

The estimated values of $\vec{s}$ in 5.11 for $F_{\langle 10,1000\rangle} = F_{\rm best}$ (denoted as $\vec{s}_{\rm best}$), together with the estimated $\vec{s}_{\rm best}$ without the k-correction are listed in the first and second column of Table 5.1. In Figure 5.1 the isotropic equivalent energy $E_{\langle 0.1,10\,000\rangle}$ as a function of $c(z)/k_{E,\rm best}(z)$, considering the k-correction (red dots) and not considering (blue dots), is shown.

The estimated values of $\vec{s}$ in 5.11 for $F_{\langle 50,300\rangle} = F_{\rm b,best}$ (denoted as $\vec{s}_{\rm b,best}$), together with the estimated $\vec{s}_{\rm b,best}$ without the k-correction are listed in the third and fourth column of Table 5.1. In Figure 5.2 the isotropic equivalent energy $E_{\langle 0.1,10\,000\rangle}$ is shown as a function of $c(z)/k_{E,\rm best}(z)$ considering the k-correction (red dots) and not considering (blue dots).

	$F_{\rm best}$		$F_{\rm b,best}$	
k-corr	with	without	with	without
$\sigma_{\log(F_{\rm best})}$	$0.596^{+0.098}_{-0.065}$		$0.596^{+0.098}_{-0.065}$	
$\sigma_{\log[c(z)/k_E(z)]}$	0.506	0.502	0.535	0.502
$\sigma_{\log\left[E_{\langle E_1,E_2\rangle}\right]}$	0.688	0.707	0.689	0.699
$\mu_{\log[c(z)/k_E(z)]}$	−57.9	−57.8	−58.2	−57.8
$\mu_{\log\left[E_{\langle E_1,E_2\rangle}\right]}$	53.2	52.8	53.2	52.8
ρ	−0.555	−0.576	−0.567	−0.566

TABLE 5.1: Values of the $\vec{s}$ for bivariate log-normal distribution 5.11 determinated by MLE for the measured fluence $F_{\rm best}$ and $F_{\rm b,best}$. For both of them with the k-correction and without it. The values of the uncertainties of $\sigma_{\log F_{\rm best}}$ and $\sigma_{\log F_{\rm b,best}}$ are really the same.

Since I have the k-corrected values of $E_{\langle 0.1,10\,000\rangle}$, the dependence on the redshift z may be easily visualized. In Figure 5.3 the $E_{\langle 0.1,10\,000\rangle}$ is plotted as a function of z computed from the measured $F_{\rm best}$ and $F_{\rm b,best}$ using the eq. 5.3. There is virtually no difference. A correlation coefficient ρ_E between $E_{\langle 0.1,10\,000\rangle}$ and z is virtually the

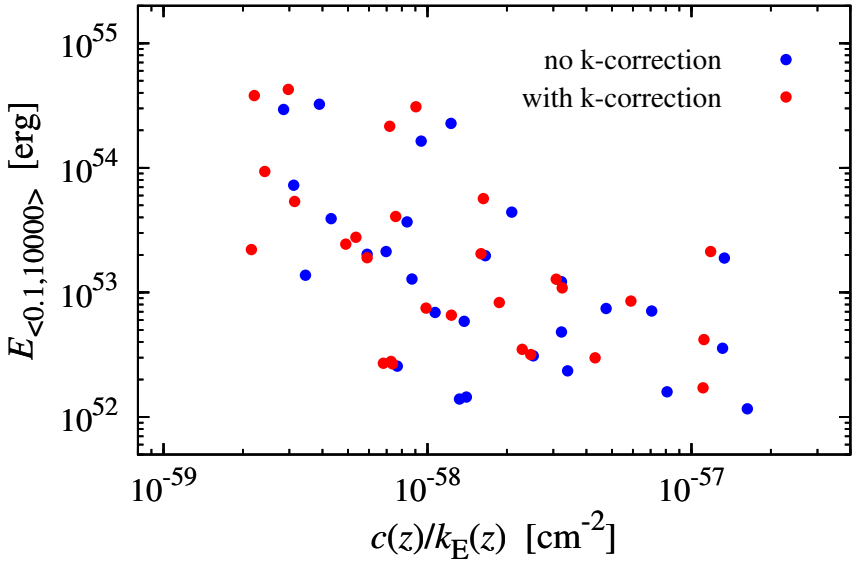

FIGURE 5.1: Distribution of $E_{\langle 0.1,10\,000\rangle}$ as a function of $c(z)/k_{\rm E}(z)$ (red dots) and of $c(z)$ alone (blue dots) (i.e. with the k-correction and without it) computed from $F_{\rm best}$ by eq. 5.9.

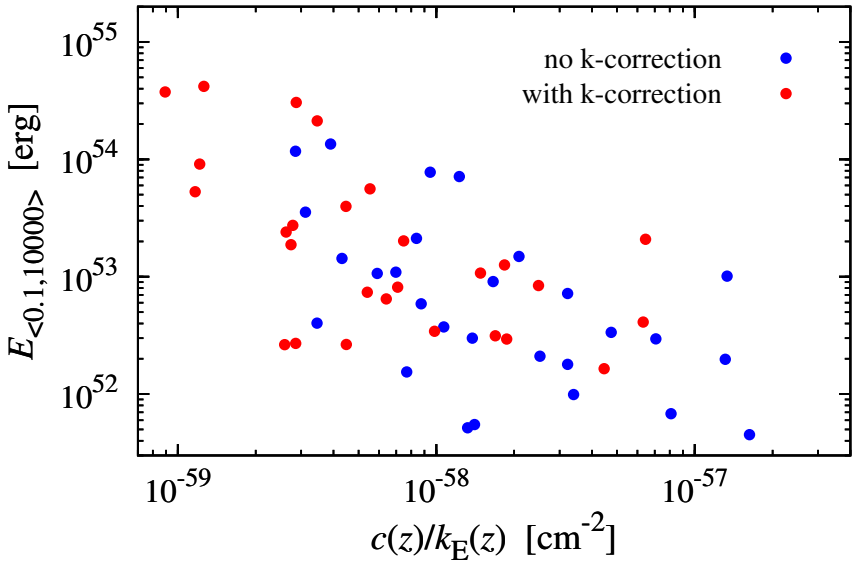

FIGURE 5.2: Distribution of $E_{\langle 0.1,10\,000\rangle}$ as a function of $c(z)/k_{\rm E}(z)$ (red dots) and of $c(z)$ alone (blue dots) (i.e. with the k-correction and without it) computed from $F_{\rm b,best}$ by eq. 5.9.

same for computation with both fluences, $\rho = 0.63$. In columns 2–5 of Table 5.4 the computed values of $E_{\langle 0.1,10\,000\rangle}$ are listed together with the k-correction factors defined by eq. 5.5.

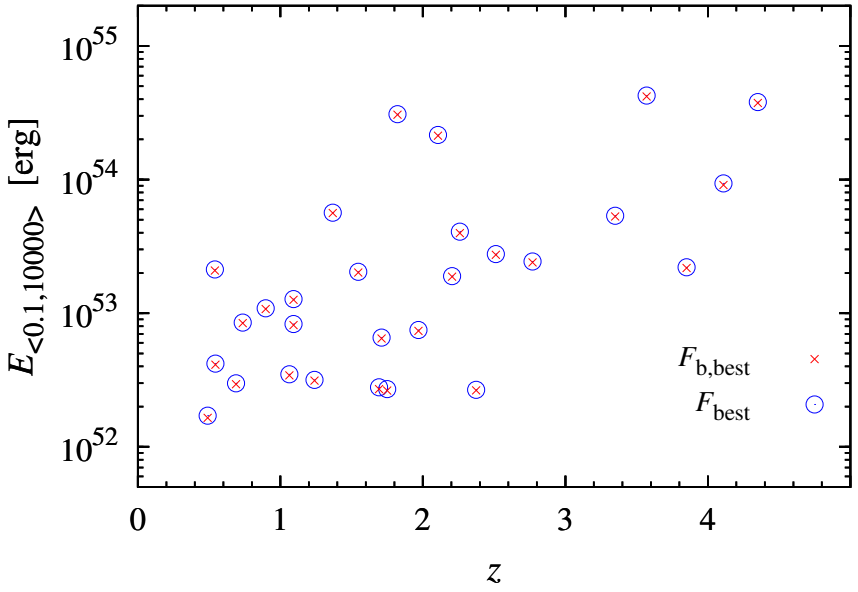

FIGURE 5.3: Distribution of the $E_{\langle 0.1,10\,000\rangle}$, computed with the k-correction for $F_{\rm best}$ (blue circles) and $F_{\rm b,best}$ (red crosses) using the eq. 5.3, as a function of the redshift z.

The next step is the estimation of averaged effective bolometric luminosity $L_{{\rm ave},\langle E_1,E_2\rangle}$ with the assumption of isotropic radiation of the burst using the formula

$$L_{{\rm ave},\langle E_1,E_2\rangle} = \frac{E_{\langle E_1,E_2\rangle}(1+z)^{0.6}}{T_{90}}. \tag{5.12}$$

The quantity $E_{\langle E_1,E_2\rangle}$ is computed from the $F_{\rm b,best}$. Computation with the $F_{\rm best}$ makes little difference (see second and third column of Table 5.4 and Figure 5.3). Due to the intrinsic characteristic of the GRBs discovered by (Fenimore et al. 1995), the factor 0.6 should be used in the exponent over $(1+z)$. The values of $L_{{\rm ave},\langle 0.1,10\,000\rangle}$ are listed in the sixth column of Table 5.4. Figure 5.8 shows the $L_{{\rm ave},\langle 0.1,10\,000\rangle}$ as a function of the redshift z. The red line will be explained in next section.

The average effective bolometric luminosity $L_{{\rm ave},\langle 0.1,10\,000\rangle}$ is computed directly from the $E_{\langle 0.1,10\,000\rangle}$. Although informative, k-corrected effective bolometric luminosity $L_{\langle 0.1,10\,000\rangle}$ computed from the peak flux $P_{\rm b,best}$ by the eq. 5.4 is more suitable for the analysis below. The values of $L_{\langle 0.1,10\,000\rangle}$ and corresponding k-correction factors $k_{\rm L}$ are listed in the seventh and eighth column of Table 5.4. Figure 5.9 shows the dependence of $L_{\langle 0.1,10\,000\rangle}$ on the redshift. The correlation coefficient ρ_L between $L_{\langle 0.1,10\,000\rangle}$ and z is $\rho_L = 0.65$.

In this section the isotropic equivalent energies and luminosities were computed. From Figures 5.1 and 5.2 it is apparent that $E_{\langle 0.1,10\,000\rangle}$ values computed without the k-correction ($k_{\rm E}$=1), do not differ from the k-corrected values in an overall trend. Values of the correlation parameter, $\rho \sim -0.5$, in the Table 5.1 confirm this. Additionally,

the correlation is also visible in Figures 5.8 and 5.9. For the burst with higher z, the $L_{\mathrm{ave},\langle 0.1,10\,000\rangle}$ and $L_{\langle 0.1,10\,000\rangle}$ is gradually higher, i.e. there is a deficit of low–luminosity bursts for $z \gtrsim 2$ and a deficit of high–luminosity burst for $z \lesssim 2$. The question arises, what is the reason for this correlation. A possible answer will be given in the following sections 5.2.1 and 5.3.

5.1.3 The Bivariate Log–normality of $\frac{c(z)}{k_{\mathrm{E}}(z)} E_{\langle 0.1,10\,000\rangle}$

In this section, the assumption of a log-normal distribution of the fluence in eq. 5.10 is tested. Considering the high p-values of the Lilliefors test for the fluences $F^{\mathrm{z}}_{\mathrm{best}}$ and $F^{\mathrm{z}}_{\mathrm{b,best}}$ in Table 6.2, the assumption of the log–normality of the eq. 5.10 is met (for description of the Lilliefors test see Appendix A).

Furthermore, the assumption of bivariate log–normal distribution of $\frac{c(z)}{k_{\mathrm{E}}(z)} E_{\langle 0.1,10\,000\rangle}$ is tested by multivariate Jarque-Bera tests (MJB) (Koizumi et al. 2009). P-values of the test are shown in Table 5.2 (for description of the tests see Appendix A). Since the p-values are high ~ 0.5, the log–normal distribution is a good assumption.

	F_{best}		$F_{\mathrm{b,best}}$	
k-corr	with	without	with	without
p-MJB^{*}_{M}	0.48	0.54	0.60	0.65
p-MJB^{*}_{S}	0.60	0.63	0.74	0.83

TABLE 5.2: P-values of the MJB tests applied on the values of $\left(\log\left[c(z)/k_E(z)\right], \log\left[E_{\langle 0.1,10\,000\rangle}\right]\right)$ computed by 5.9 for F_{best} and $F_{\mathrm{b,best}}$, with the k-correction and without it. The depictions of relevant $\left(\log\left[c(z)/k_E(z)\right], \log\left[E_{\langle 0.1,10\,000\rangle}\right]\right)$ are in figures 5.1 and 5.2. For details of p-values p-MJBm and p-MJBs see Appendix A.

5.1.4 Spectral Functions

The approach of taking four different spectral functions needs some discussion, which is done in this subsection.

Considering the rest frame energy interval $\langle 0.1, 10\,000\rangle$, for which the quantities in section 5.1.2 were derived, one assumes that the spectral functions – derived over the energy interval $\langle e_1, e_2\rangle$ – describe the intrinsic spectrum well. All four spectral functions defined in section 4.2.5 can fit the spectrum reasonably well and none is significantly more preferred than the other.

However, PLAW model is probably the most problematic, since it likely describes the spectra over the wide $\langle 0.1, 10\,000\rangle$ keV energy interval less accurately. The spectrum of the burst hardly have a form of a PLAW in bolometric energy range since the isotropic equivalent energy E_{bol} and peak luminosity L_{bol} would be infinite. It is plausible that a spectrum – best fitted by a PLAW model in $\langle 10, 1000\rangle$ keV energy interval – deviates

from the actual spectrum in $\langle 0.1, 10\,000\rangle$ keV energy interval. BAND, COMP or SBPL, may characterize the spectrum in that interval better and it does not hugely depend on which since they do not differ significantly compared to PLAW. One may even conclude that the spectrum in $\langle 10, 1000\rangle$ is only high-energy part of BAND or SBPL spectra, but the $E_{\rm peak}$ or $E_{\rm b}$ is too low for detection (i.e. $E_{\rm peak}$ or $E_{\rm b} < 10\,{\rm keV}$). Other possibility is that it is a low-energy part of the BAND, COMP or SBPL spectra, but the $E_{\rm peak}$ or $E_{\rm b}$ is too high (i.e. $E_{\rm peak}$ or $E_{\rm b} > 1000\,{\rm keV}$). For the spectra best fitted by the PLAW model, the most common situation is, that the spectrum has a poor quality (e.i. small S/N ratio) and the PLAW model with only two free parameters is statistically sufficient to describe the spectrum (i.e. taking a model with more free parameters does not significantly improve the fit). Indeed, one can see from figures 5.4, 5.5 and 5.6 that the fluences – $F_{\rm best}$ and $F_{\rm b,best}$ – and peak fluxes $P_{\rm b,best}$ of the GRBs, best fitted by PLAW function, are smaller in comparison with the fluences and peak fluxes of the GRBs, best fitted by the other three spectral functions.

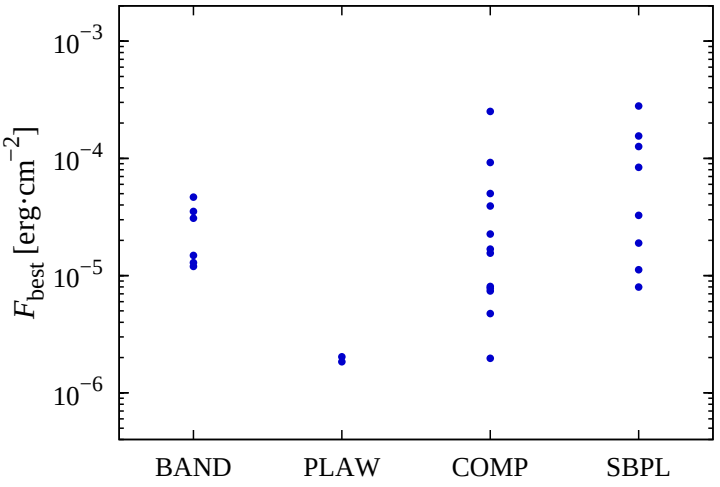

FIGURE 5.4: Depiction of $F_{\rm best}$ with respect to the best fitted spectral function (over the duration of the burst), BAND, PLAW, COMP and SBPL, of the GRBz sample.

The difference of the shape of the spectral functions is illustrated in figure 5.7 where I choose to depict the BAND, PLAW, COMP and SBPL functions for the burst GRB091024372. For better visibility of the spectra in the whole energy range $E_{\langle 0.1,10\,000\rangle}$, $E^2\phi(E)$ –also known as νF_ν power spectrum– is chosen. In the energy interval delimited by the vertical lines one can see that the spectral functions do not differ from each other much compared with the rest of the energy intervals. One may suggest that the PLAW model is an "average" of the rest of the models. BAND, COMP and SBPL functions are practically identical in low energy part of the spectrum $E \lesssim 100\,{\rm keV}$ compared with the PLAW which is above the others. In high energy part $E \gtrsim 100\,{\rm keV}$ the spectral functions differ a lot. PLAW is again above the other ones. The figure adequately represents the typical shape of the spectral functions when the

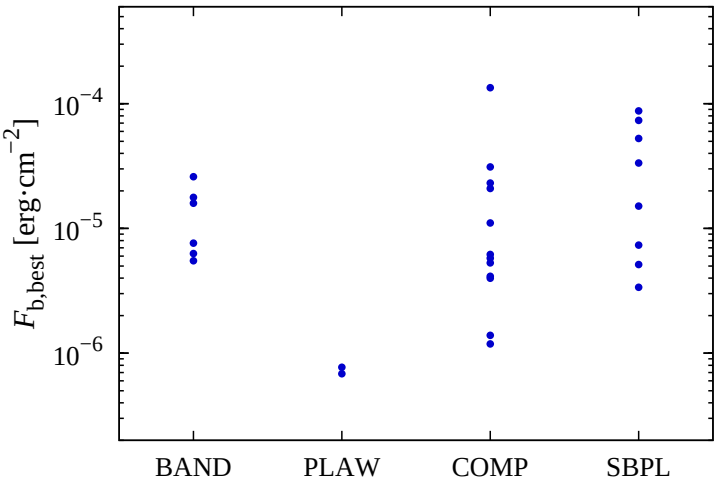

FIGURE 5.5: Depiction of $F_{\mathrm{b,best}}$ with respect to the best fitted spectral function (over the duration of the burst), BAND, PLAW, COMP and SBPL, of the GRBz sample.

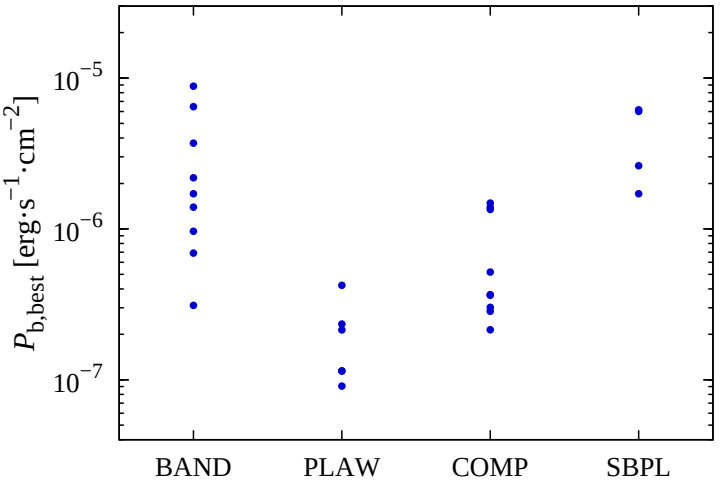

FIGURE 5.6: Depiction of $P_{\mathrm{b,best}}$ with respect to the best fitted spectral function (over the peak flux of the burst), BAND, PLAW, COMP and SBPL, of the GRBz sample.

GRB is best fitted by a PLAW model. From it follows that the quantities $E_{\langle 0.1,10\,000\rangle}$ and $L_{\langle 0.1,10\,000\rangle}$ may be most likely overestimated considering the PLAW model in calculation. In figure 5.10, $L_{\langle 0.1,10\,000\rangle}$ computed using every spectral model for the bursts in GRBz sample, is shown. This trend is clearly visible. The quantitative measure of the difference between the $L_{\langle 0.1,10\,000\rangle}$ computed by different spectral functions is taken to be an arithmetic mean of the corresponding $L_{\langle 0.1,10\,000\rangle}$ values for all the bursts in the GRBz sample[3]. In addition, the mean of $L_{\langle 0.1,10\,000\rangle}$ using the best fitted spectral functions is shown. The means are listed in Table 5.3.

In this section I discussed the approach of taking different spectral functions for deriving $L_{\langle 0.1,10\,000\rangle}$. From Table 5.3 one can see that for PLAW model the mean is

[3]For each spectral model, there will be sample of 28 values of $L_{\langle 0.1,10\,000\rangle}$.

higher than that of the others, which are basically the same. This may introduce some uncertainty in to the results. Its size depends on the percentage of the burst which are best fitted by a PLAW model[4].

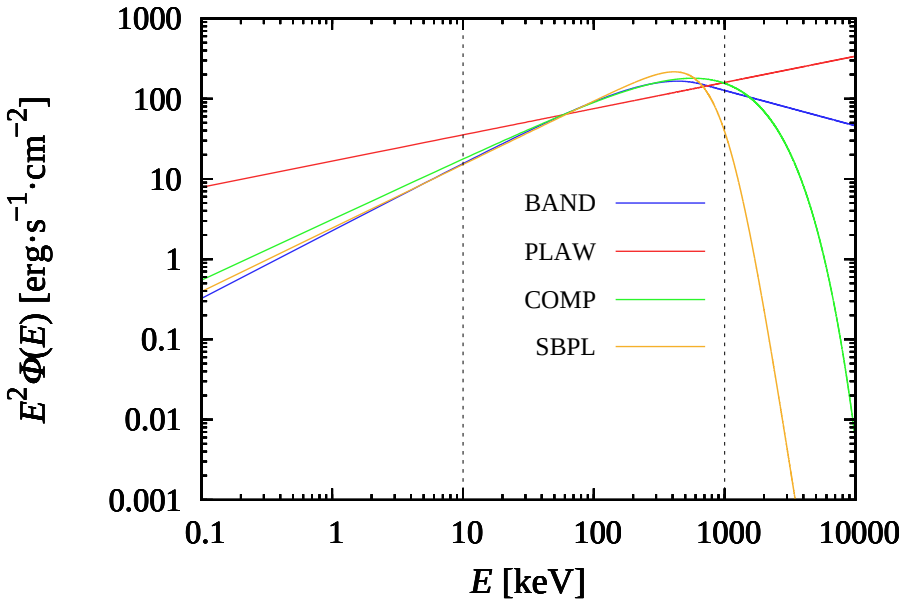

FIGURE 5.7: Comparison of the BAND (blue), PLAW (red), COMP (green) and SBPL (yellow) functions fitted over the peak flux for the burst designated as GRB091024372. Vertical lines delimit the energy interval $\langle 10, 1000 \rangle$ keV over which the spectral functions were fitted.

$L_{\langle 0.1,10\,000 \rangle}$ $[\mathrm{erg \cdot s^{-1}}]$				
BAND	PLAW	COMP	SBPL	BEST
$1.357 \cdot 10^{53}$	$1.704 \cdot 10^{53}$	$1.274 \cdot 10^{53}$	$1.339 \cdot 10^{53}$	$1.344 \cdot 10^{53}$

TABLE 5.3: List of the arithmetic means of $L_{\langle 0.1,10\,000 \rangle}$ for five different calculations. First four values correspond to $L_{\langle 0.1,10\,000 \rangle}$ derived by taking one spectral model –either BAND, PLAW, COMP or SBPL –for every burst and the last value is calculated using the best fitted model for the peak flux spectra.

5.2 Effect of the Detection Threshold

In this section it will be shown that a large part of the correlation of $L_{\langle 0.1,10\,000 \rangle}$ with redshift can be explained by the effect of the detector threshold. A curve in Figures 5.8 and 5.9 denotes the threshold limit of the detector. It is derived by assuming a sharp threshold model with $P_{\mathrm{thresh}} = 0.7$ ph$\cdot$s$^{-1}\cdot$cm^{-2}, where P_{thresh} is the lowest flux that can trigger the detector in the energy range $\langle 50, 300 \rangle$ keV. Crucial in derivation is the assumption of an "average" spectrum of the burst. This was taken to be a BAND

[4]The percentages of the burst, considering the best fitted spectral function, are listed in Table 6.6.

function 4.1 characterized by $\alpha_{\rm med} = -0.75$, $\beta_{\rm med} = -3.03$ and $E_{\rm peak,med} = 294\,{\rm keV}$, which are the median values of the spectral parameters of the BAND function fits of the spectra over the duration of the peak flux of the bursts in the GRBz sample. Amplitude A of the BAND function is computed so that $P^{\rm ph}_{\langle e_1,e_2\rangle} = P_{\rm thresh}$, where $P^{\rm ph}_{\langle e_1,e_2\rangle}$ is flux in units of $\left[{\rm ph}\cdot{\rm s}^{-1}\cdot{\rm cm}^{-2}\right]$. The BAND function constructed by this way is used for calculation of the k-corrected $L_{\langle 0.1,10\,000\rangle}$ using the eq. 5.4. Thus constructing the "threshold" $L_{\langle 0.1,10\,000\rangle}$ as a function of z.

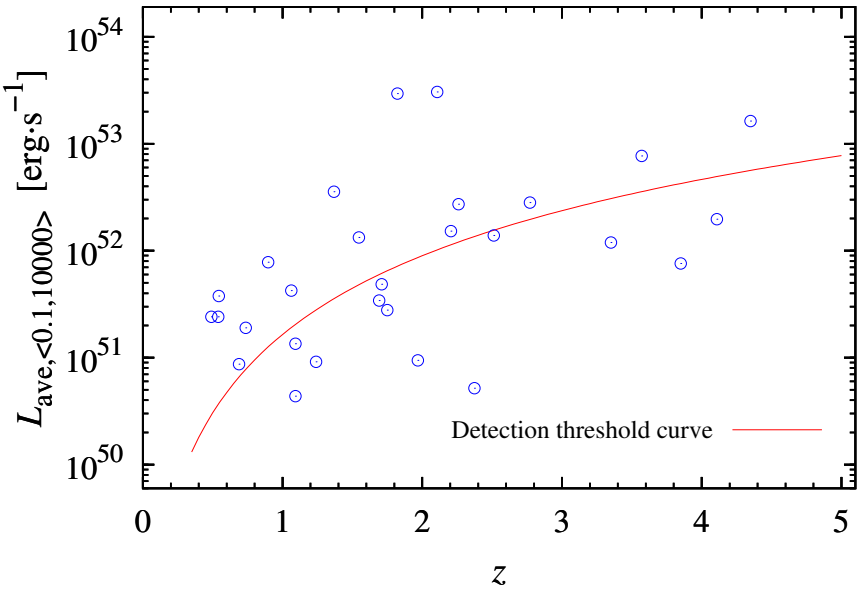

FIGURE 5.8: Distribution of the $L_{{\rm ave},\langle 0.1,10\,000\rangle}$, computed for $F_{\rm b,best}$ (blue circles) using the eq. 5.12, as a function of the redshift z. Red curve denotes the detection threshold limit derived by assuming, a) a sharp threshold with $P_{\rm thresh} = 0.7\ {\rm ph}\cdot{\rm s}^{-1}\cdot{\rm cm}^{-2}$ in $\langle 50, 300\rangle$ keV energy range, b) "average" Band function with spectral parameters defined above.

The sharp detector threshold model described in previous paragraph is more appropriate for the $L_{\langle 0.1,10\,000\rangle}$ than for $L_{{\rm ave},\langle 0.1,10\,000\rangle}$ (see Figure 5.9 and 5.8, respectively), since the detector threshold algorithm operates on time scales of fractions of seconds to seconds [Chapter 3]. The curve effectively separates the GRBs which could be detected by the FERMI satellite from those which could not be.

In this section, the detection threshold bias, that favors more luminous bursts in greater redshifts, was described. The detection threshold curve accounts for the absence of less luminous bursts for higher redshifts nicely. On the other hand, this effect surely cannot account for an apparent deficit of bright burst at lower redshifts $z \lesssim 2$ as is seen in Figures 5.3, 5.8 and 5.9. Because the detection threshold effect is most easily taken care for quantity $L_{\langle 0.1,10\,000\rangle}$, in the next section I will analyze this apparent deficit in the $\left[z, L_{\langle 0.1,10\,000\rangle}\right]$ plane.

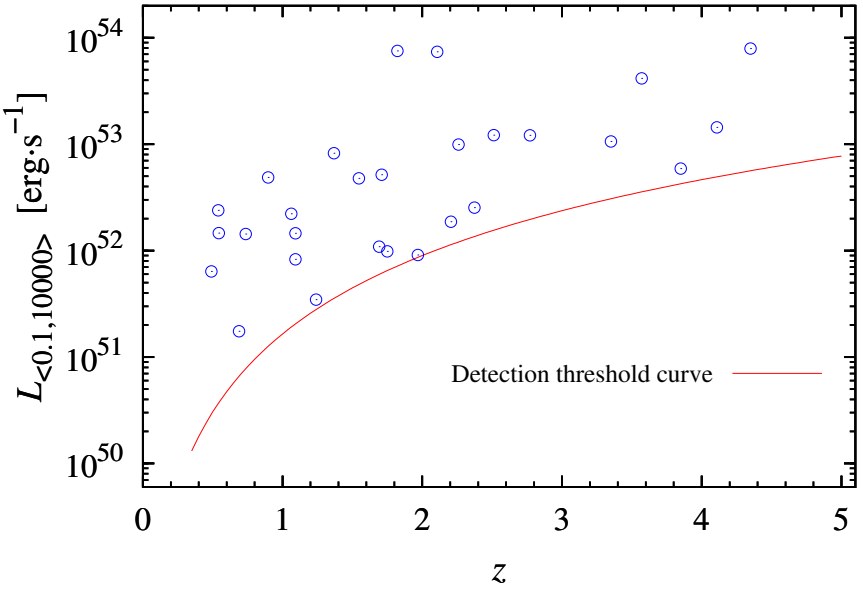

FIGURE 5.9: Distribution of the $L_{\langle 0.1,10\,000\rangle}$, computed for $F_{\mathrm{b,best}}$ (blue circles) using the eq. 5.4, as a function of the redshift z. Red curve denotes the detection threshold limit derived by assuming a sharp threshold with $P_{\mathrm{thresh}} = 0.7\ \mathrm{ph}\cdot\mathrm{s}^{-1}\cdot\mathrm{cm}^{-2}$ in $\langle 50, 300\rangle$ keV energy range and an "average" Band function with spectral parameters defined above.

5.2.1 Sharp Detection Threshold Model

Now the assumption of sharp detection threshold will be discussed. As one can see in figure 5.10, the detection threshold curves derived by assuming an "average" spectrum for each spectral function defined in the caption, are virtually the same for BAND, COMP and SBPL models. This assumption brings a small uncertainty into the results since the real threshold cannot be represented as a curve and more complicated description is needed. However, the uncertainty will be small due to the fact that the position of the detection threshold curve does not change strongly by varying the spectral parameters. Additionally, further away the spectral parameters from their median values are, less GRBs have them. As discussed above, a PLAW model most likely overestimates the value of $L_{\langle 0.1,10\,000\rangle}$, thus the corresponding curve lies above the other three.

Despite the simplification of the complicated detection threshold algorithm working on a multiple time scales and multiple threshold settings, the bursts in GRBz sample depicted in figure 5.10 are above the detection threshold curves – for BAND, COMP and SBPL – with exceptions. Thus fortifying the approach of taking four different spectral functions in calculation of the intrinsic properties of the GRBs.

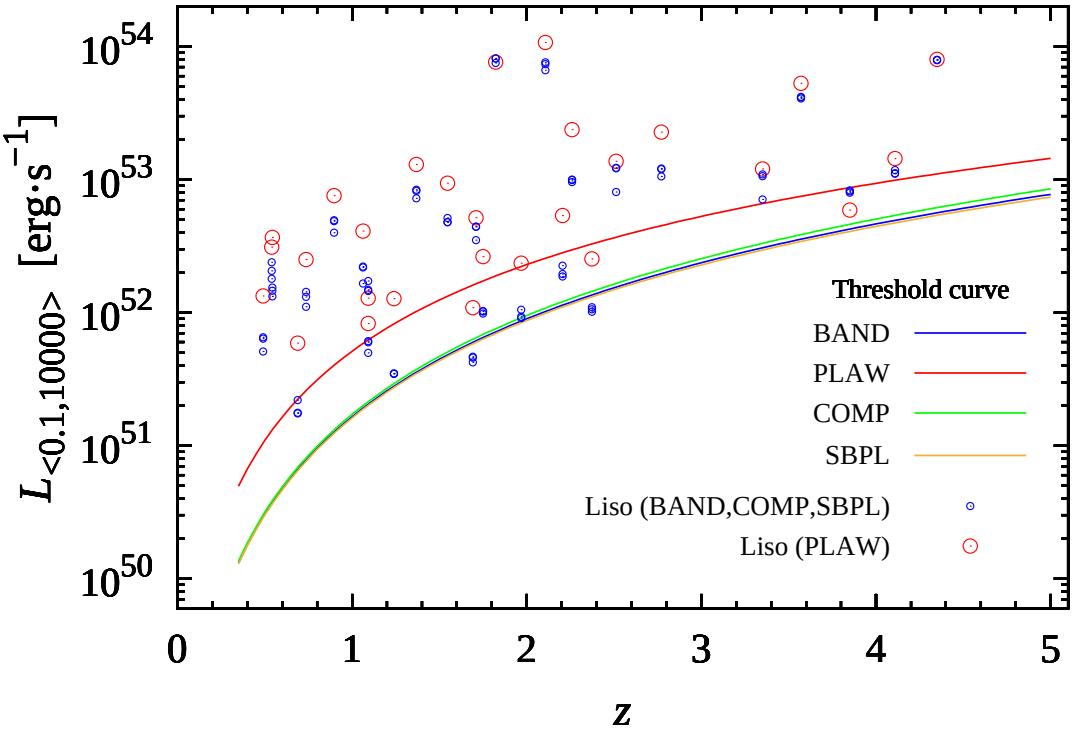

FIGURE 5.10: Comparison of the $L_{\langle 0.1,10\,000\rangle}$ computed using the PLAW model (red circles) with $L_{\langle 0.1,10\,000\rangle}$ computed using the BAND, COMP and SBPL model (blue points). Additionally the detection threshold curves derived by assuming an "average" spectrum with spectral parameters taken as medians of the relevant spectral characteristics are depicted. For BAND (blue) $\alpha = -0.75$, $\beta = -3.03$ and $E_{\rm peak} = 294\,\mathrm{keV}$; PLAW (red) $\lambda = -1.48$; COMP (green) $\alpha = -0.784$, $E_{\rm peak} = 265\,\mathrm{keV}$ and SBPL (yellow) $\lambda_1 = -0.874$, $\lambda_2 = -2.723$, $E_{\rm b} = 190.4\,\mathrm{keV}$ and $\Delta = 0.3$. Assuming the sharp detection threshold of the FERMI detectors as $P_{\rm thresh} = 0.7\,\mathrm{ph}\cdot\mathrm{s}^{-1}\cdot\mathrm{cm}^{-2}$.

Designation	$E_{\rm best}$ $[10^{52}{\rm erg}]$	$E_{\rm b,best}$ $[10^{52}{\rm erg}]$	$k_{\rm E,best}$	$k_{\rm E,b,best}$	$L_{{\rm ave},\langle 0.1,10\,000\rangle}$ $[10^{52}\,\frac{\rm erg}{\rm s}]$	$L_{\langle 0.1,10\,000\rangle}$ $[10^{52}\,\frac{\rm erg}{\rm s}]$	$k_{\rm L}$	z
GRB080804972	18.9	18.7	1.47	3.19	1.52	$1.87^{+0.08}_{-0.35}$	1.39	2.2045
GRB080810549	53.6	53.0	1.37	3.70	1.19	$10.6^{+2.9}_{-1.9}$	3.39	3.35
GRB080905705	2.67	2.64	1.04	1.71	0.05	$2.53^{+0.55}_{-0.39}$	5.05	2.374
GRB080916009	379	374	1.29	3.19	16.27	$79.2^{+4.2}_{-6.1}$	2.85	4.35
GRB080916406	2.99	2.93	1.87	4.32	0.08	$0.175^{+0.011}_{-0.026}$	1.62	0.689
GRB080928628	2.79	2.70	1.93	4.91	0.34	$1.09^{+0.16}_{-0.08}$	4.96	1.692
GRB081008832	7.48	7.38	1.08	1.97	0.094	$0.91^{+0.06}_{-0.37}$	1.52	1.9685
GRB081121858	27.7	27.3	1.30	2.50	1.39	$12.2^{+0.1}_{-7.8}$	3.50	2.512
GRB081221681	40.7	39.7	1.10	1.87	2.72	$9.93^{+0.82}_{-0.35}$	1.49	2.26
GRB081222204	24.4	24.0	1.20	2.25	2.82	$12.1^{+1.8}_{-1.0}$	1.97	2.77
GRB090102122	20.4	20.1	1.03	2.21	1.33	$4.77^{+0.18}_{-0.25}$	2.24	1.547
GRB090113778	2.70	2.63	1.94	5.10	0.277	$0.98^{+0.05}_{-0.21}$	1.57	1.7493
GRB090323002	425	418	1.31	3.09	7.71	$41.5^{+2.2}_{-2.9}$	2.63	3.57
GRB090328401	8.51	8.42	1.19	2.84	0.190	$1.434^{+0.075}_{-0.066}$	3.42	0.736
GRB090424592	4.19	4.11	1.17	2.07	0.377	$1.459^{+0.052}_{-0.038}$	1.92	0.544
GRB090516353	93.5	91.0	1.28	2.56	1.97	$14.4^{+1.5}_{-1.2}$	4.11	4.109
GRB090519881	22.0	21.8	1.60	5.42	0.758	$6.0^{+1.4}_{-1.0}$	4.62	3.85
GRB090618353	21.2	20.8	1.12	2.06	0.240	$2.387^{+0.039}_{-0.047}$	3.43	0.54
GRB090902462	308	305	1.35	4.27	29.5	$75.21^{+0.44\dagger}_{-0.44}$	5.31	1.822
GRB090926181	215	212	1.31	2.73	30.53	$73.8^{+1.6}_{-1.4}$	2.55	2.1062
GRB090926914	3.16	3.13	1.02	1.48	0.091	$0.35^{+0.01}_{-0.10}$	1.37	1.24
GRB091003191	10.8	10.7	1.46	3.20	0.781	$4.86^{+0.20}_{-0.19}$	3.29	0.8969
GRB091020900	6.56	6.46	1.11	2.15	0.484	$5.17^{+0.35}_{-0.32}$	6.22	1.71
GRB091024372	8.29	8.15	1.72	4.54	0.135	$0.83^{+0.21}_{-0.12}$	5.45	1.092
GRB091024380	12.7	12.6	1.04	1.75	0.043	$1.45^{+0.38}_{-0.36}$	6.17	1.092
GRB091127976	1.71	1.64	1.47	3.65	0.240	$0.637^{+0.018}_{-0.015}$	2.66	0.49
GRB091208410	3.48	3.42	1.48	3.45	0.423	$2.22^{+0.21}_{-0.23}$	2.62	1.063
GRB100414097	56.5	56.1	1.28	3.76	3.55	$8.23^{+0.63}_{-0.43}$	3.33	1.368

TABLE 5.4: Derived quantities for the GRBz sample. $E_{\rm best}$, $E_{\rm b,best}$, $k_{\rm E,best}$ and $k_{\rm E,b,best}$ denotes the isotropic equivalent energy released in energy range $\langle 0.1, 10\,000\rangle$ computed by taking $F_{\rm best}$ and $F_{\rm b,best}$ in eq. 5.3, respectively. Corresponding k-corrections computed by eq. 5.5 are denoted as $k_{\rm E,best}$ and $k_{\rm E,b,best}$. $L_{{\rm ave},\langle 0.1,10\,000\rangle}$ denotes the average effective bolometric luminosity in $\langle 0.1, 10\,000\rangle$ keV energy range defined by eq. 5.12 and $L_{\langle 0.1,10\,000\rangle}$ denotes the effective bolometric luminosity computed from $P_{\rm b,best}$ by eq. 5.3. Corresponding k-correction computed by eq. 5.6 is denoted as $k_{\rm L}$. The errors of $L_{\langle 0.1,10\,000\rangle}$ are computed by Monte Carlo technique briefly described in section 5.4.

†This error estimate is not reliable (see section 5.4).

5.3 Evolution of the GRB Rate and Luminosity Function

5.3.1 Theory

The first natural suggestion how the *GRB rate* depends on redshift is the assumption of a linear correlation with the SFR, $\dot{\rho}_{\rm GRB} \propto \dot{\rho}_{\rm SFR}$, where $\dot{\rho}_{\rm GRB}$ is the number of the bursts per year in the redshift interval $< z, z + {\rm d}z >$ and $\dot{\rho}_{\rm SFR}$ is the mass of the new born stars per year in the redshift interval $< z, z + {\rm d}z >$. However, to test a possible evolution of the GRB rate with respect to SFR, one should assume a deviation from it parameterized by a function $\xi(z)$; so we may write $\dot{\rho}_{\rm GRB}(z) \propto \xi(z)\dot{\rho}_{\rm SFR}(z)$.

For the description of the *observed* distribution of the GRBs I use a formula from Kistler et al. (2008) with a slight modification

$$\frac{{\rm d}\dot{N}(z)}{{\rm d}z{\rm d}\log L} \propto \Psi(z)\Phi(L)\dot{\rho}_{\rm GRB}(z)\frac{{\rm d}V(z)}{{\rm d}z}\frac{1}{1+z} = \Psi(z)\Phi(L)\xi(z)\dot{\rho}_{\rm SFR}(z)\frac{{\rm d}V(z)}{{\rm d}z}\frac{1}{1+z}, \tag{5.13}$$

where ${\rm d}\dot{N}(z)$ is the rate of bursts (per year) in the redshift interval $\langle z, (z + {\rm d}z)\rangle$ and luminosity interval $\langle \log L, (\log L + {\rm d}\log L)\rangle$, ${\rm d}V(z)/{\rm d}z$ is the comoving volume element, $1/(1 + z)$ is required by cosmological time dilation, $\Psi(z)$ is the fraction of bursts that can be seen at a given z and $\Phi(L)$ is the luminosity function of the GRBs.

$\Phi(L)$ is traditionally defined as a fraction of bursts with isotropic equivalent luminosities $L_{\langle E_1,E_2\rangle}$ in the interval $\langle \log L, (\log L + {\rm d}\log L)\rangle$. Assuming that the luminosity function is redshift independent (see subsection 2.3.3), we may define

$$\frac{{\rm d}\dot{N}_{\rm L}(z)}{{\rm d}z} = \int_{L_1}^{L_2} \frac{{\rm d}\dot{N}(z)}{{\rm d}z{\rm d}\log L}{\rm d}\log L, \tag{5.14}$$

where ${\rm d}\dot{N}_{\rm L}(z)$ is the rate of bursts (per year) in the redshift interval $\langle z, (z + {\rm d}z)\rangle$ and in an arbitrary luminosity interval $\langle L_1, L_2\rangle$. Then the equation

$$\frac{{\rm d}\dot{N}_{\rm L}(z)}{{\rm d}z} \propto \Psi(z)\dot{\rho}_{\rm GRB}(z)\frac{{\rm d}V(z)}{{\rm d}z}\frac{1}{1+z} = \Psi(z)\xi(z)\dot{\rho}_{\rm SFR}(z)\frac{{\rm d}V(z)}{{\rm d}z}\frac{1}{1+z} \tag{5.15}$$

holds.

Assuming the ΛCDM cosmological model with parameters stated in section 5.1.1, the comoving volume element may be expressed as

$$\frac{{\rm d}V}{{\rm d}z} = \frac{4\pi {\rm c}^3}{H_0^3}\frac{\int_0^z \frac{{\rm d}z'}{E(z')}}{E(z)}, \tag{5.16}$$

where

$$E(z) = \sqrt{(1+z)^3\Omega_M + \Omega_\Lambda}\ .$$

The star formation history of the universe is presently well known up to the redshift $z \approx 6$ and can be described by a number of empirical functions (Cole et al. 2001; Hopkins and Beacom 2006). For example, Cole et al. (2001) proposed for the $\dot{\rho}_{\rm SFR}$ function in the form

$$\dot{\rho}_{\rm SFR} = \dot{\rho}_{\rm c}(z) \propto \frac{a + bz}{1 + \left(\frac{z}{c}\right)^d}, \tag{5.17}$$

where (a, b, c, d) are free parameters. Hopkins and Beacom (2006) introduced a piecewise function in a form

$$\dot{\rho}_{\rm SFR} = \dot{\rho}_{\rm hop}(z) \propto \begin{cases} a(1+z)^b & \text{for } z < z_1 \\ c(1+z)^d & \text{for } z_1 < z < z_2 \\ e(1+z)^f & \text{for } z_2 < z < 6\,, \end{cases} \tag{5.18}$$

where $(a, b, c, d, e, f, z_1, z_2)$ are free parameters, but c and e are not independent, because $\dot{\rho}_{\rm hop}(z)$ should be continuous.

5.3.2 Testing of Evolution

Apparent deficit of the bright bursts $L_{\langle 0.1,10\,000\rangle} \gtrsim 10^{52.5}\mathrm{erg\cdot s^{-1}}$ for the redshifts $z \lesssim 2.5$ is seen in Figure 5.9. The question is, what is the reason for this behaviour. One of the possible hypotheses can be that the luminosity function of the GRB is redshift dependent. To test this hypothesis I create a sample of the GRBs matching the following criteria, a) the bursts have the peak luminosities in the range $\left\langle L^{\rm low}_{\langle 0.1,10\,000\rangle}, L^{\rm max}_{\langle 0.1,10\,000\rangle}\right\rangle$, where $L^{\rm low}_{\langle 0.1,10\,000\rangle}$ is an arbitrary lower value of the range and $L^{max}_{\langle 0.1,10\,000\rangle}$ is the effective bolometric peak luminosity of the most luminous burst, b) for minimizing the effect of the detection threshold I choose only the bursts with the redshifts z in the interval $\langle 0, z_{\rm tr}\rangle$, where $z_{\rm tr}$ is the highest redshift at which the burst with $L^{\rm low}_{\langle 0.1,10\,000\rangle}$ could be detected (this means that the point $\left[z_{\rm tr}, L^{\rm low}_{\langle 0.1,10\,000\rangle}\right]$ lies on the detection threshold curve: see Figure 5.11).

The question arises how to pick the $L^{\rm low}_{\langle 0.1,10\,000\rangle}$. I choose the approach of maximizing the number of burst,$n_{\rm max}$, for which the criteria above are met. I have found $n_{\rm max} = 14$ for $L^{\rm low}_{\langle 0.1,10\,000\rangle} = 1.36 \cdot 10^{52}\,\mathrm{erg\cdot s^{-1}}$ and $z_{\rm tr} = 2.374$. In Figure 5.11 the $L_{\langle 0.1,10\,000\rangle}$ is shown with respect to z. The denoted area depicts the region for which the criteria above are met. GRBs within the shaded area are listed in Table 5.5.

Since I want to study the possible luminosity function evolution, I have to create two independent subsamples of GRBs, each containing bursts in separate luminosity intervals. The idea is that, if there is any luminosity function evolution, then the functional form of the left hand side of eq. 5.15 should differ for separate luminosity intervals $\langle L_1, L_2\rangle$ and $\langle L_1', L_2'\rangle$. Conversely, if there is no luminosity function evolution,

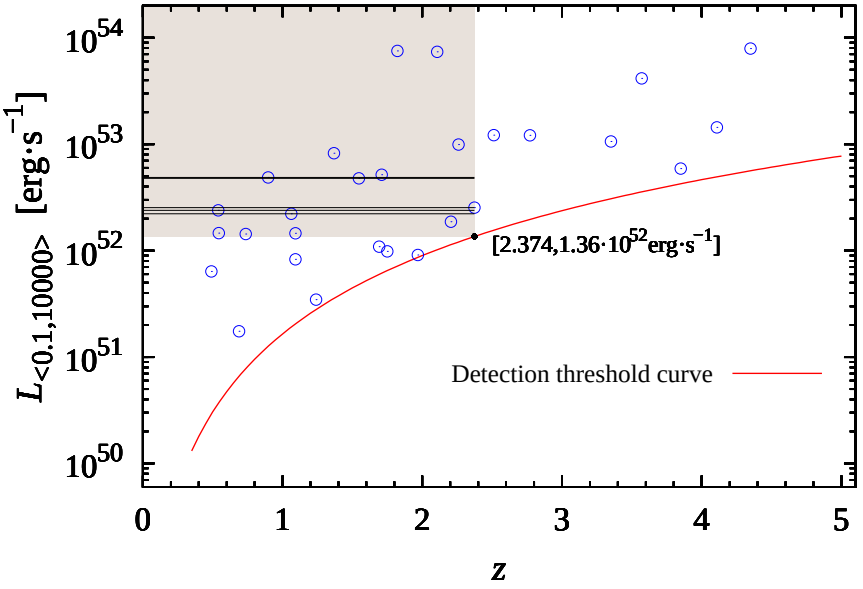

FIGURE 5.11: Distribution of the $L_{\langle 0.1,10\,000\rangle}$, computed for $F_{\mathrm{b,best}}$ (blue circles) using the eq. 5.4, as a function of the redshift z. Red curve denotes the detection threshold limit derived by assuming a sharp threshold with $P_{\mathrm{thresh}} = 0.7\ \mathrm{ph}\cdot\mathrm{s}^{-1}\cdot\mathrm{cm}^{-2}$ in $\langle 50, 300\rangle$ keV energy range. Shaded region denotes the area obtained by maximizing the number of bursts in that area. Horizontal lines denotes the "dividing" luminosities $L_{\mathrm{div1}} = 2.2154\cdot 10^{52}\,\mathrm{erg}\cdot\mathrm{s}^{-1}$, $L_{\mathrm{div2}} = 2.3874\cdot 10^{52}\,\mathrm{erg}\cdot\mathrm{s}^{-1}$, $L_{\mathrm{div3}} = 2.5306\cdot 10^{52}\,\mathrm{erg}\cdot\mathrm{s}^{-1}$, $L_{\mathrm{div4}} = 4.7712\cdot 10^{52}\,\mathrm{erg}\cdot\mathrm{s}^{-1}$, $L_{\mathrm{div5}} = 4.8621\cdot 10^{52}\,\mathrm{erg}\cdot\mathrm{s}^{-1}$, that separates the GRBs in the shaded region into two subsamples. Critical –black– point denotes the $\left[z_{\mathrm{tr}}, L^{\mathrm{low}}_{\langle 0.1,10\,000\rangle}\right] = \left[2.374, 1.36\cdot 10^{52}\,\mathrm{erg}\cdot\mathrm{s}^{-1}\right]$.

the functional form of the left hand side of the eq. 5.15 should be the same for any luminosity interval $\langle L_1, L_2\rangle$.

Taking the GRBs in the shaded region I have to choose the "dividing" luminosity[5] L_{div}, which separates the GRBs into two independent subsamples. Method, which I choose should minimize the bias introduced by taking only one value of L_{div}. Instead of taking one L_{div} I choose several of them with the condition of having minimum of five bursts in each sample. Five different L_{div} met the condition: $L_{\mathrm{div1}} = 2.2154\cdot 10^{52}\,\mathrm{erg}\cdot\mathrm{s}^{-1}$, $L_{\mathrm{div2}} = 2.3874\cdot 10^{52}\,\mathrm{erg}\cdot\mathrm{s}^{-1}$, $L_{\mathrm{div3}} = 2.5306\cdot 10^{52}\,\mathrm{erg}\cdot\mathrm{s}^{-1}$, $L_{\mathrm{div4}} = 4.7712\cdot 10^{52}\,\mathrm{erg}\cdot\mathrm{s}^{-1}$, $L_{\mathrm{div5}} = 4.8621\cdot 10^{52}\,\mathrm{erg}\cdot\mathrm{s}^{-1}$. See Figure 5.11.

First, the testing of the GRB rate evolution is carried out by maximizing a p-value of the Kolmogorov–Smirnov test. The Kolmogorov–Smirnov test compares the empirical cumulative distribution of the redshifts in one subsample of GRBs, with its theoretical Cumulative Distribution Function ($CDF_{\mathrm{theor}}(z)$) derived from the eq. 5.15

[5]Superscript $\langle 0.1, 10\,000\rangle$ is omitted due to the shortening.

	$L_{\langle 0.1,10\,000\rangle}$ $[\mathrm{erg}\cdot\mathrm{s}^{-1}]$	z
GRB090328401	$1.43\cdot10^{52}$	0.736
GRB091024380	$1.45\cdot10^{52}$	1.092
GRB090424592	$1.46\cdot10^{52}$	0.544
GRB080804972	$1.87\cdot10^{52}$	2.2045
GRB091208410	$2.22\cdot10^{52}$	1.063
GRB090618353	$2.39\cdot10^{52}$	0.54
GRB080905705	$2.53\cdot10^{52}$	2.374
GRB090102122	$4.77\cdot10^{52}$	1.547
GRB091003191	$4.86\cdot10^{52}$	0.8969
GRB091020900	$5.17\cdot10^{52}$	1.71
GRB100414097	$8.23\cdot10^{52}$	1.368
GRB081221681	$9.93\cdot10^{52}$	2.26
GRB090926181	$7.38\cdot10^{53}$	2.1062
GRB090902462	$7.52\cdot10^{53}$	1.822

TABLE 5.5: List of bursts which met the conditions, a) their effective bolometric luminosity $L_{\langle 0.1,10\,000\rangle}$ lie in the interval $\langle 1.36\cdot10^{52}, 7.52\cdot10^{53}\rangle$, b) their measured redshifts lie in the interval $\langle 0, 2.374\rangle$.

as follows

$$CDF_{\mathrm{theor}}(z) = \frac{\int_0^z (1+z')^{\omega}\dot{\rho}_{\mathrm{SFR}}(z')\frac{\mathrm{d}V}{\mathrm{d}z'}\frac{1}{1+z'}\mathrm{d}z'}{\int_0^{z_{\mathrm{tr}}} (1+z')^{\omega}\dot{\rho}_{\mathrm{SFR}}(z')\frac{\mathrm{d}V}{\mathrm{d}z'}\frac{1}{1+z'}\mathrm{d}z'} \tag{5.19}$$

with the essential assumption of $\Psi(z) = \mathrm{const}$. The GRB rate evolution $\xi(z)$ was parameterized by a power function $\xi(z) = (1+z)^{\omega}$, where ω is a free parameter over which the p-value of the K–S test is maximized.

The null hypothesis of the test is that the sample of redshifts is drawn from the reference distribution defined by the eq. 5.15. The maximizing of p-value of the K–S test over ω is done for each of the two subsamples defined by L_{div} (together 10).

To study the dependence of results on the SFR function, analysis is performed for three SFR functions $\dot{\rho}_{\mathrm{SFR}}(z')$. The first $\dot{\rho}_{\mathrm{cole}}(z)$, obtained by Cole et al. (2001), has the form of 5.17 with $(a,b,c,d) = (0.0166, 0.1848, 1.9474, 2.6316)$. The second $\dot{\rho}_{\mathrm{hop}}(z)$, obtained by Hopkins and Beacom (2006), is also in a form of 5.17 with $(a,b,c,d) = (0.017, 0.13, 3.3, 5.3)$. The third $\dot{\rho}_{\mathrm{hop,pw}}(z)$, obtained by Hopkins and Beacom (2006) is in a form of 5.18 with[6]

$$(a,b,c,d,e,f,z_1,z2) = (0.0151, 3.28, 0.1888, -0.26, 10\,000, -8, 1.04, 4.48).$$

[6]The SFR functions are derived assuming the *Salpeter* Initial Mass Function (IMF) – for $\dot{\rho}_{\mathrm{cole}}(z)$ – and *modified Salpeter A* IMF – for $\dot{\rho}_{\mathrm{hop}}(z)$ and $\dot{\rho}_{\mathrm{hop,pw}}(z)$.

By maximizing the p-value of the K–S test, over the parameter ω, for each subsample of the GRBs and for each SFR function, the values $\omega_{\max}$ were obtained. These values are summarized in Table 5.6. For illustration of the empirical and theoretical cumulative distribution functions look at Figure 5.12 and 5.13.

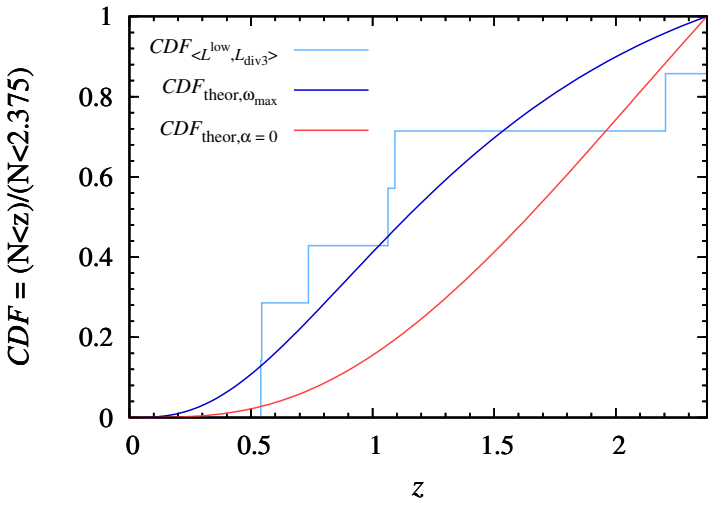

FIGURE 5.12: Depiction of cumulative distribution functions for the subsample of GRB with luminosities in the interval $\langle 1.36 \cdot 10^{52}, 2.5306 \cdot 10^{52} \rangle$ erg$\cdot$s^{-1} and redshifts in the interval $\langle 0, 2.374 \rangle$. Light blue curve denotes the empirical CDF, dark blue curve denotes the theoretical CDF (eq.5.19) with $\omega_{\max} = -3$ derived by maximizing the p-value of the K–S test. Red curve denotes the theoretical CDF with $\omega_{\max} = 0$. Assumed SFR function is $\dot{\rho}_{\mathrm{hop}}(z)$.

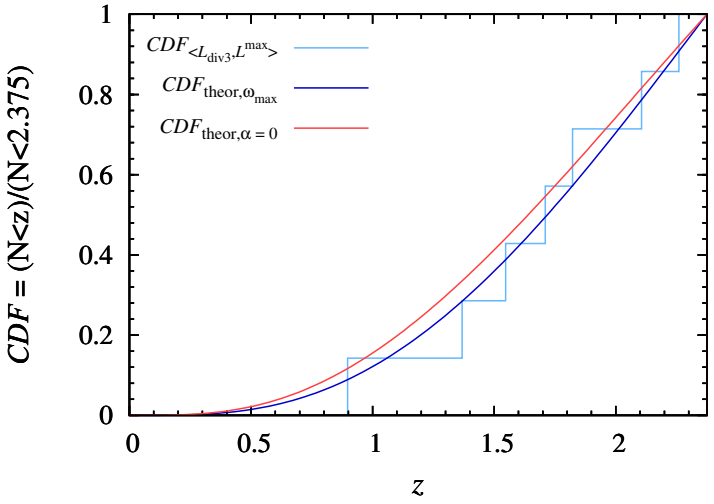

FIGURE 5.13: Depiction of cumulative distribution functions for the subsample of GRB with luminosities in the interval $\langle 2.5306 \cdot 10^{52}, 7.53 \cdot 10^{53} \rangle$ erg$\cdot$s^{-1} and redshifts in the interval $\langle 0, 2.374 \rangle$. Light blue curve denotes the empirical CDF, dark blue curve denotes the theoretical CDF (eq.5.19) with $\omega_{\max} = -3$ derived by maximizing the p-value of the K–S test. Red curve denotes the theoretical CDF with $\omega_{\max} = 0$. Assumed SFR function is $\dot{\rho}_{\mathrm{hop}}(z)$.

In Figure 5.14 a typical graph of the p-values of the K–S test as a function of ω is shown. One can see that the confidence interval of the ω – setting the significance level on $\alpha = 0.05$ – covers a wide range of values, typically 6–10, proving useless for its reasonable estimation. Additionally, for lesser significance level, the null hypothesis can be rejected for higher p-values. Therefore, the values in Table 5.6 carry little if none information. One can make only suggestion that generally the ω tends to be lower for the luminosity interval $\langle L^{\mathrm{low}}, L_{\mathrm{div}} \rangle$ compared with $\langle L_{\mathrm{div}}, L^{\mathrm{max}} \rangle$. The GRB luminosity function evolution is not seen, because the confidence intervals of the p-values for GRBs in different luminosity ranges are overlapping (for the given significance level).

	ω_{max}					
	$\dot{\rho}_{\mathrm{cole}}$		$\dot{\rho}_{\mathrm{hop}}$		$\dot{\rho}_{\mathrm{hop,pw}}$	
	$\langle L^{\mathrm{low}}, L_{\mathrm{div}} \rangle$	$\langle L_{\mathrm{div}}, L^{\mathrm{max}} \rangle$	$\langle L^{\mathrm{low}}, L_{\mathrm{div}} \rangle$	$\langle L_{\mathrm{div}}, L^{\mathrm{max}} \rangle$	$\langle L^{\mathrm{low}}, L_{\mathrm{div}} \rangle$	$\langle L_{\mathrm{div}}, L^{\mathrm{max}} \rangle$
L_{div1}	−3.5	1.6	−4.2	0.6	−4.1	1.3
L_{div2}	−3.8	3.0	−4.4	1.7	−4.4	2.9
L_{div3}	−2.2	1.8	−3.0	0.6	−2.5	1.8
L_{div4}	−1.7	2.3	−2.6	1.1	−2.1	2.3
L_{div5}	−2.3	3.8	−3.1	2.6	−2.7	3.8

TABLE 5.6: Values of the ω_{max}, for which the p-values of the K–S test are highest, computed for five different pairs of GRB subsamples. Each pair is defined by low luminosity boundary $L^{\mathrm{low}} = 1.36 \cdot 10^{52}\,\mathrm{erg \cdot s^{-1}}$, high luminosity boundary $L^{\mathrm{max}} = 7.53 \cdot 10^{53}\,\mathrm{erg \cdot s^{-1}}$ and by different value of ""dividing luminosity which separates the bursts to two subsamples, L_{div}. Values of L_{div} are $L_{\mathrm{div1}} = 2.2154 \cdot 10^{52}\,\mathrm{erg \cdot s^{-1}}$, $L_{\mathrm{div2}} = 2.3874 \cdot 10^{52}\,\mathrm{erg \cdot s^{-1}}$, $L_{\mathrm{div3}} = 2.5306 \cdot 10^{52}\,\mathrm{erg \cdot s^{-1}}$, $L_{\mathrm{div4}} = 4.7712 \cdot 10^{52}\,\mathrm{erg \cdot s^{-1}}$, $L_{\mathrm{div5}} = 4.8621 \cdot 10^{52}\,\mathrm{erg \cdot s^{-1}}$. All values of ω_{max} are computed for three different SFR function, $\dot{\rho}_{\mathrm{cole}}$ and $\dot{\rho}_{\mathrm{hop}}$ and $\dot{\rho}_{\mathrm{hop,pw}}$.

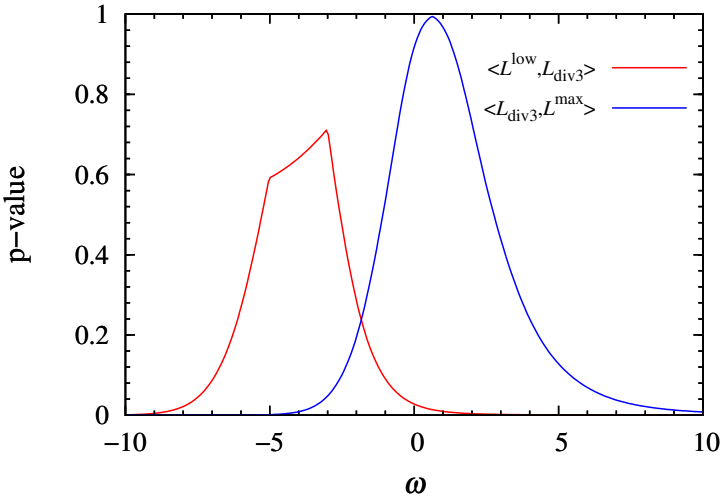

FIGURE 5.14: P-value of the K–S test as a function of ω. Red curve denotes the p-values computed for the subsample of GRBs with luminosities in the interval $\langle L^{\mathrm{low}}, L_{\mathrm{div}} \rangle$, where $L^{\mathrm{low}} = 1.36 \cdot 10^{52}\,\mathrm{erg \cdot s^{-1}}$ and $L_{\mathrm{div3}} = 2.5306 \cdot 10^{52}\,\mathrm{erg \cdot s^{-1}}$. Blue curve denotes the p-values for the luminosities in the interval $\langle L_{\mathrm{div}}, L^{\mathrm{max}} \rangle$, where $L^{\mathrm{max}} = 7.53 \cdot 10^{53}\,\mathrm{erg \cdot s^{-1}}$.

However, having the p-values of the K–S test for $\omega = 0$ one can estimate the incompatibility of the GRB rate evolution with SFR[7]. Values of $p_{\omega=0}$ are listed in Table 5.7. The p-values $p_{\omega=0}$, for the subsample of GRBs with luminosities in the range $\langle L^{\mathrm{low}}, L_{\mathrm{div}} \rangle$, fluctuate around the significance level $\alpha = 0.05$ (lower p-values are for $\dot{\rho}_{\mathrm{hop}}$).

	$p_{\omega=0}$					
	$\dot{\rho}_{\mathrm{cole}}$		$\dot{\rho}_{\mathrm{hop}}$		$\dot{\rho}_{\mathrm{hop,pw}}$	
	$\langle L^{\mathrm{low}}, L_{\mathrm{div}} \rangle$	$\langle L_{\mathrm{div}}, L^{\mathrm{max}} \rangle$	$\langle L^{\mathrm{low}}, L_{\mathrm{div}} \rangle$	$\langle L_{\mathrm{div}}, L^{\mathrm{max}} \rangle$	$\langle L^{\mathrm{low}}, L_{\mathrm{div}} \rangle$	$\langle L_{\mathrm{div}}, L^{\mathrm{max}} \rangle$
L_{div1}	0.071	0.758	0.028	0.971	0.057	0.774
L_{div2}	0.023	0.374	0.007	0.805	0.017	0.391
L_{div3}	0.082	0.523	0.028	0.918	0.064	0.542
L_{div4}	0.192	0.517	0.073	0.901	0.150	0.534
L_{div5}	0.078	0.209	0.023	0.486	0.059	0.218

TABLE 5.7: Values of the $p_{\omega=0}$, p-values of the K–S test for $\omega = 0$, computed for five different pairs of GRB subsamples. Each pair is defined by the low luminosity boundary $L^{\mathrm{low}} = 1.36 \cdot 10^{52}\,\mathrm{erg \cdot s^{-1}}$, the high luminosity boundary $L^{\mathrm{max}} = 7.53 \cdot 10^{53}\,\mathrm{erg \cdot s^{-1}}$ and by different value of the "dividing" luminosity, L_{div}, which separates the bursts into two subsamples. Values of L_{div} are $L_{\mathrm{div1}} = 2.2154 \cdot 10^{52}\,\mathrm{erg \cdot s^{-1}}$, $L_{\mathrm{div2}} = 2.3874 \cdot 10^{52}\,\mathrm{erg \cdot s^{-1}}$, $L_{\mathrm{div3}} = 2.5306 \cdot 10^{52}\,\mathrm{erg \cdot s^{-1}}$, $L_{\mathrm{div4}} = 4.7712 \cdot 10^{52}\,\mathrm{erg \cdot s^{-1}}$, $L_{\mathrm{div5}} = 4.8621 \cdot 10^{52}\,\mathrm{erg \cdot s^{-1}}$. All values of $p_{\omega=0}$ are computed for three different SFR function, $\dot{\rho}_{\mathrm{cole}}$, $\dot{\rho}_{\mathrm{hop}}$ and $\dot{\rho}_{\mathrm{hop,pw}}$.

Procedure above might become fruitful if the confidence interval for the ω, defined by the significance level of the p-value of the K–S test, will be in the order of tenth. Therefore, more GRBs with known redshifts would be useful.

Another approach for determination of the luminosity function evolution is to perform the two-sample K–S test on the luminosity subsamples described above. This approach might be more useful, because the biases, which are functions of redshift, are attenuated. However, biases which have a luminosity dependence are not. Further, the assumption of correlation with the SFR is irrelevant. The null hypothesis is that the subsamples comes from the same distribution, which means – no luminosity evolution. The p-values of the two-sample K–S test applied to five pairs of GRB subsamples are listed in Table 5.8.

5.3.3 Choosing the z_{tr}

The approach of maximizing the number of bursts in the region defined by condition $L > L^{\mathrm{low}}_{0.1,10\,000}$ and $z < z_{\mathrm{tr}}$, may not be adequate in a situation of having a small number of bursts. Although having a maximum number of bursts increases the robustness of the statistical analysis, the measure of the improvement is slight. It may happen that by choosing a different $L^{\mathrm{low}}_{0.1,10\,000}$ and $z < z_{\mathrm{tr}}$, allowing smaller number of bursts in the

[7] Stating the null hypothesis as: there is no evolution assuming particular $\dot{\rho}_{\mathrm{SFR}}$.

	p-value	
	$\langle L^{\mathrm{low}}, L_{\mathrm{div}} \rangle$	$\langle L_{\mathrm{div}}, L^{\mathrm{max}} \rangle$
L_{div1}	0.148	
L_{div2}	0.032	
L_{div3}	0.129	
L_{div4}	0.352	
L_{div5}	0.063	

TABLE 5.8: P-values of the two-sample K–S test computed for five different pairs of GRB subsamples. Each pair is defined by the low luminosity boundary $L^{\mathrm{low}} = 1.36 \cdot 10^{52}\,\mathrm{erg} \cdot \mathrm{s}^{-1}$, the high luminosity boundary $L^{\mathrm{max}} = 7.53 \cdot 10^{53}\,\mathrm{erg} \cdot \mathrm{s}^{-1}$ and by different value of the "dividing" luminosity, L_{div}, which separates the bursts into two subsamples. Values of L_{div} are $L_{\mathrm{div1}} = 2.2154 \cdot 10^{52}\,\mathrm{erg} \cdot \mathrm{s}^{-1}, L_{\mathrm{div2}} = 2.3874 \cdot 10^{52}\,\mathrm{erg} \cdot \mathrm{s}^{-1}, L_{\mathrm{div3}} = 2.5306 \cdot 10^{52}\,\mathrm{erg} \cdot \mathrm{s}^{-1}, L_{\mathrm{div4}} = 4.7712 \cdot 10^{52}\,\mathrm{erg} \cdot \mathrm{s}^{-1}, L_{\mathrm{div5}} = 4.8621 \cdot 10^{52}\,\mathrm{erg} \cdot \mathrm{s}^{-1}$.

region, the results may change dramatically. This problem can be solved simply by waiting for more GRBs with determined redshifts.

5.3.4 $\Psi(z) = \mathrm{const}$

Assumption that is most likely erroneous is expressed by a simple equation $\Psi(z) = \mathrm{const}$. In this function all the biases are hidden. Generally, the situation may become more complicated since Ψ can also be a function of luminosity. However, I will assume that it is *not*.

Kistler et al. (2008) describes the fraction of observable bursts, Ψ, as a product of multiple independent functions; $\Psi(z) = \psi_{\mathrm{E/A}}\psi_{\mathrm{AG}}\psi_{\mathrm{human}}\psi_{\mathrm{FERMI}}\psi_{\mathrm{GRBz}}$. The $\psi_{\mathrm{E/A}}$ function comprises the emission/absorption bias. Redshifts of closer bursts tend to be determined by emission lines of the host galaxies and redshifts of more distant bursts by an absorption lines in the afterglow spectra. ψ_{AG} denotes the observability of the optical afterglow. In ψ_{human} function, non-intrinsic properties, like which ground telescope is chosen for the observation of the afterglow, are included. ψ_{FERMI} denotes the detectability of the bursts by the FERMI satellite. Finally, ψ_{GRBz} contains the bias introduced by creating the GRBz sample.

In section 6.1 I have shown that the GRBz sample is not a random sampling from the GRBall sample, indicating that ψ_{GRBz} is not a constant and should have an influence on the results.

If we assume that the ψ_{GRBz} is not dependent on luminosity, then the p-values of the two-sample K–S test in able 5.8 are not influenced by this bias. However, the p-values should be considered as less reliable since the $\mathrm{k} = \mathrm{N_1N_2}/(\mathrm{N_1} + \mathrm{N_2}) \sim 3.5$, where $\mathrm{N_1}$ and $\mathrm{N_2}$ are the sizes of the subsamples. For details of the K–S test see Appendix A.

5.3.5 On the meaning of the significances

In section 5.3 the GRB rate evolution and GRB luminosity function evolution were studied. Given the p-values of the K–S test in Table 5.7, the GRB rate of the GRBs with luminosities in the interval $\sim \langle 1.36 \cdot 10^{52}, 2.5 \cdot 10^{52} \rangle \,\mathrm{erg \cdot s^{-1}}$ is incompatible with the SFR function $\dot{\rho}_{\mathrm{hop}}$ on $\sim 95\,\%$ significance level. However, for the SFR functions $\dot{\rho}_{\mathrm{cole}}$ and $\dot{\rho}_{\mathrm{hop,pw}}$ the GRB rate is compatible with them. The GRBs with luminosities in the interval $\sim \langle 2.5 \cdot 10^{52}, 7.5 \cdot 10^{53} \rangle \,\mathrm{erg \cdot s^{-1}}$ look as they are compatible with the star formation rate. However, the confidence interval, on the $\sim 95\,\%$ significance level, for the ω is $\sim \langle -3, 7 \rangle$, therefore one cannot conclude the compatibility. Strictly speaking, the null hypothesis – the observed distribution of the GRBs is drawn from the theoretical distribution, which depends on ω – is not rejected on given significance level $\sim 95\,\%$ for $\omega \in \sim \langle -3, 7 \rangle$.

The p-values in Table 5.8 indicate possible luminosity function evolution, however, it is hard to establish the significance level. The p-values fluctuate noticeably, which shows sensitivity on the L_{div}. If we discard the highest p-value, then the null hypothesis that the two subsamples come from the same distribution (no luminosity evolution) is rejected on $\sim 85\,\%$ significance level.

All this means, that the apparent gap in the shaded region in Figure 5.11, is not statistically significant.

5.4 Computation of the Uncertainties

In this section I describe the method I used for the computation of the uncertainties. Generally, the calculation of error is possibly the trickiest thing to do. It requires many assumptions, which are hard to validate. The method I choose, is a widely known Monte Carlo technique, which relies on the capability of producing random numbers and brute computational force.

To estimate the probability density function (PDF) and confidence interval of the quantity $g = f(a_1, \ldots, a_n)$, which is a function of n parameters $a_1, \ldots, a_n$ (denoted $\vec{a}$), one have to have a covariance matrix of these parameters. Further, assuming that $\vec{a}$ come from a multivariate normal distribution, defined by this covariance matrix, one can generate a correlated random vector $\vec{b}$. That will be used in the function $g = f(b_1, \ldots, b_n)$. By generating many ($\sim 10\,000$) random vectors $\vec{b}$ and calculating g for each one of them, one can construct the PDF of g. The confidence interval can be determined by calculation of an appropriate quantiles of the PDF (for further details see Appendix C).

In Table 5.4, the uncertainties of $L_{\langle 0.1,10\,000\rangle}$ are shown. They were computed by, a) taking the relevant covariance matrixes from the FERMIGBRST database[8], b) calculation of the relevant PDF using 10 000 iterations, c) setting the quantiles of the confidence interval as $\langle 0.159, 84.1\rangle$, so that 68.2 % of the all simulated values of $L_{\langle 0.1,10\,000\rangle}$ lie in this interval.

The uncertainties of $P_{\mathrm{b,best}}$ listed in Table 4.1 are computed similarly.

This method can produce reasonable estimates of the uncertainties if the assumption of multinormality of $\vec{a}$ is met. For the bursts GRB081121858 and GRB090902462, the assumption, that the spectral parameters come from a multivariate normal distribution, is probably not met, since the simulated PDF covered wide range of values and the estimated confidence intervals of the relevant quantities were unrealistic.

In figure 5.15 the uncertainties of $L_{\langle 0.1,10\,000\rangle}$ are shown as error bars. One can make a suggestion that the error bars are smaller if the burst is further away from the detection threshold curve.

[8] http://heasarc.gsfc.nasa.gov/FTP/fermi/data/gbm/triggers/

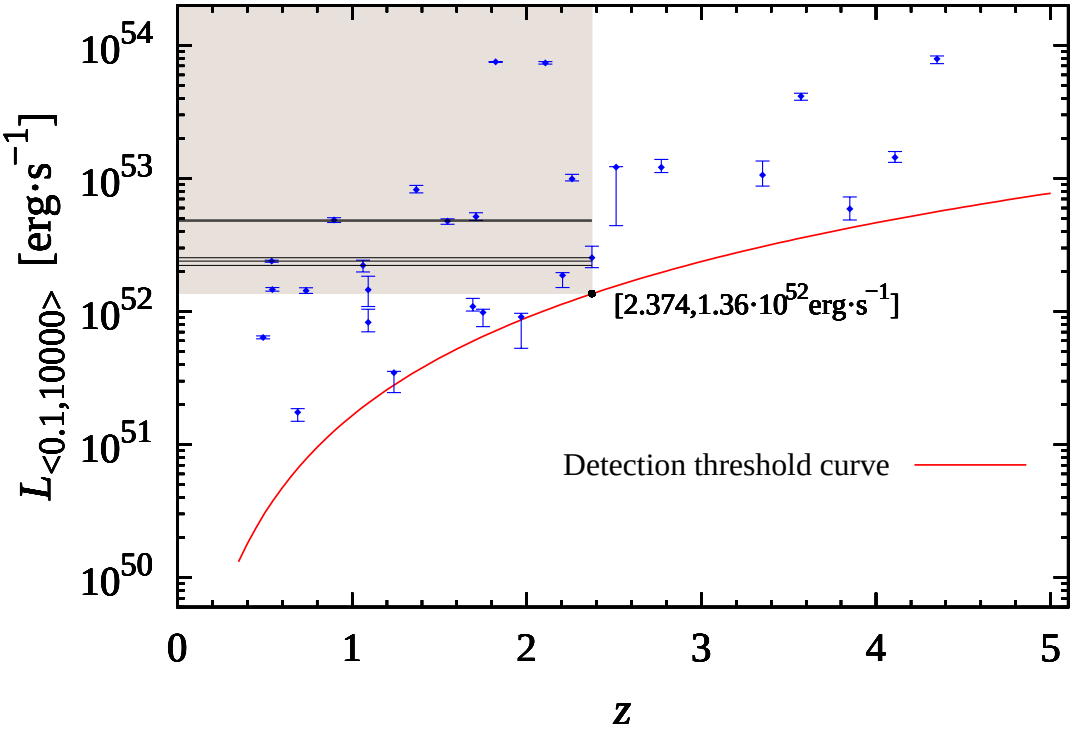

FIGURE 5.15: Distribution of the $L_{\langle 0.1,10\,000\rangle}$, computed for $F_{\mathrm{b,best}}$ (blue circles) using the eq. 5.4, as a function of the redshift z. Red curve denotes the detection threshold limit derived by assuming a sharp threshold with $P_{\mathrm{thresh}} = 0.7\ \mathrm{ph}\cdot\mathrm{s}^{-1}\cdot\mathrm{cm}^{-2}$ in $\langle 50, 300\rangle$ keV energy range. Shaded region denotes the area obtained by maximizing the number of bursts in that area. Horizontal lines denotes the "dividing" luminosities $L_{\mathrm{div1}} = 2.2154\cdot 10^{52}\,\mathrm{erg}\cdot\mathrm{s}^{-1}, L_{\mathrm{div2}} = 2.3874\cdot 10^{52}\,\mathrm{erg}\cdot\mathrm{s}^{-1}, L_{\mathrm{div3}} = 2.5306\cdot 10^{52}\,\mathrm{erg}\cdot\mathrm{s}^{-1}, L_{\mathrm{div4}} = 4.7712\cdot 10^{52}\,\mathrm{erg}\cdot\mathrm{s}^{-1}, L_{\mathrm{div5}} = 4.8621\cdot 10^{52}\,\mathrm{erg}\cdot\mathrm{s}^{-1}$, that separates the GRBs in the shaded region into two subsamples. Critical –black– point denotes the $\left[z_{\mathrm{tr}}, L^{\mathrm{low}}_{\langle 0.1,10\,000\rangle}\right] = \left[2.374, 1.36\cdot 10^{52}\,\mathrm{erg}\cdot\mathrm{s}^{-1}\right]$. The error bars are computed by Monte Carlo technique described in section 5.4 and Appendix B. The lower value of $L_{\langle 0.1,10\,000\rangle}$ is obtained as a 0.159 quantile of the relevant probability density distribution. The upper value of $L_{\langle 0.1,10\,000\rangle}$ is obtained as a 0.841 quantile of the relevant probability density distribution. Number of iterations in Monte Carlo simulation is $n = 10\,000$.

Chapter 6

Analyses of the GRBall, GRBtrun and GRBz Sample

6.1 Statistical Tests

Because I studied the intrinsic physical properties of the GRBs, the knowledge of the redshifts (assuming particular cosmology) greatly helped. Therefore, all previous calculations of these properties were done for the GRBz sample alone. The question arises whether the GRBz sample does represent a random sampling from the GRBall sample. If it does not, the properties derived using GRBz sample, are not representative of all GRBs detected by the FERMI satellite. Oppositely, if it does, then the derived properties may characterize the intrinsic properties of the GRBs detected by FERMI satellite well. All three samples, GRBz, GRBtrun and GRBall, will be needed in the study of the random sampling.

6.1.1 The GRBtrun Sample

Statistical tests, which I will use have several assumptions. In order to carry out a proper statistical analysis these assumptions must be satisfied. To test the randomness of sampling, which is the goal, I choose several measured physical quantities, considering both the GRBall and the GRBz sample. An inconvenience occurs, when the F-test and the t-test are applied directly. One of the assumptions of these tests, is the independence of the samples, which is not the case for the GRBall and GRBz samples. Therefore, the GRBtrun sample[1], instead of the GRBall sample, will also be used. The first question is, how much the GRBall and the GRBtrun samples differ. The expectations is that the sample does not change significantly, when excluding a small number of bursts from the GRBall sample. To test the significance of the change I use the K–S test (see Appendix A for details). P-values of the tests are shown in Table 6.1. Since all p-values

[1] For the definition of the GRBtrun sample see the section 4.1.

are identically or very close to 1, one can really say that the GRBtrun and GRBall do not differ on high level of significance. Thus the expectation is met. For illustration, a cumulative plot of the quantity T_{90} for the GRBall and GRBtrun sample is shown in Figure 6.1.

	T_{90}	$F_{\rm best}$	$F_{\rm b,best}$	P_{64}	P_{256}	P_{1024}	$P_{\rm b,64}$	$P_{\rm b,256}$	$P_{\rm b,1024}$
p-value	1	0.933	0.928	1	1	1	1	1	1

TABLE 6.1: P-values of the two–sample K–S test comparing the GRBtrun and GRBall sample.

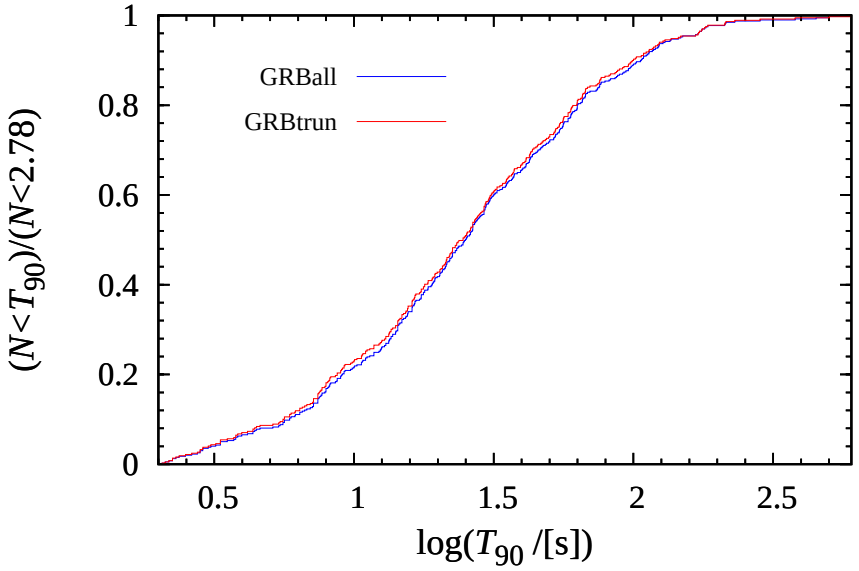

FIGURE 6.1: Cumulative plot of the T_{90} for the GRBall (blue) and GRBtrun (red) samples.

6.1.2 Test of Log-normality

The log-normality assumption is a common feature of many statistical tests. Many procedures may be used to test this assumption. One of them is the Lilliefors test for normality, which is a modification of the Kolmogorov–Smirnov test of goodness of the fit. The test is also suitable for small samples, which is the main reason why was it chosen (see Appendix A for details).

Since I am using the Lilliefors test to assess the log-normality assumption of the F-test and t-test, p-values for GRBtrun and GRBz sample are important. For completeness, p-values for GRBall sample are also computed. Physical quantities, log-normality of which I have tested are as follows: T_{90}, $F_{\rm best}$, $F_{\rm bbest}$, $P_{\rm [64,256,1024]}$, $P_{\rm b[64,256,1024]}$. The p-values obtained by applying the Lilliefors test on the selected quantities are shown in Table 6.2.

	T_{90}	$F_{\rm best}$	$F_{\rm b,best}$	P_{64}	P_{256}	P_{1024}	$P_{\rm b,64}$	$P_{\rm b,256}$	$P_{\rm b,1024}$
GRBall	0.809	0.329	0.718	0	0	0	0	0	0
GRBtrun	0.836	0.668	0.300	0	0	0	0	0	0
GRBz	0.156	0.918	0.626	0.022	0.012	0.020	0.324	0.265	0.285

TABLE 6.2: P-values of the Lilliefors test applied on T_{90}, $F_{\rm best}$, $F_{\rm b,best}$, P_{64}, P_{256}, P_{1024}, $P_{\rm b64}$, $P_{\rm b256}$, $P_{\rm b1024}$ for GRBall and GRBz sample.

P-values can be viewed, arguably, as a measure of validity of the log-normality assumption. Strictly speaking, if p-value is greater than significance level alpha one cannot reject the null hypothesis on the given significance level. The alpha level I have chosen for rejecting the null hypothesis is alpha = 0.05 (i.e. a standard 2-sigma level). If a p-value is greater than alpha, then one does not reject the null hypothesis (log-normality), otherwise one accepts the alternative hypothesis (non-log-normality).

Table 6.2 tells us that the log-normal assumption of T_{90} is not rejected for all three samples. Similarly, log-normality of $F^{z}_{\rm best}$, $F^{\rm all}_{\rm b,best}$ and $F^{\rm z}_{\rm b,best}$ is not in doubt. However, all the other quantities, on high level of significance, do not have log-normal distributions. It should be noted that p-values of the quantities of the GRBz sample tend to be higher than those of the GRBtrun sample. A second interesting fact is that the physical quantities computed in the 50–300 keV energy range tend to have greater p-values than quantities computed in the 10–1000 keV energy range.

6.1.3 Tests of the Randomness of the Sampling

F-test

Now I may apply F-test on the measured quantities for which an assumption of the log-normality is not rejected on the given level of significance ($\alpha = 0.05$): T_{90}, $F_{\rm best}$ and $F_{\rm bbest}$. The F-test tests the null hypothesis that the two samples (GRBtrun and GRBz) have the same variance. The assumptions are the independence and normality (see Appendix A for details), respectively. P-values of the F-test are listed in Table 6.3. Validity of the null hypothesis is not in question.

	T_{90}	$F_{\rm best}$	$F_{\rm b,best}$
p-value	0.385	0.402	0.648

TABLE 6.3: P-values of the F-test applied on T_{90}, $F_{\rm best}$, $F_{\rm b,best}$ comparing the GRBtrun and GRBz sample.

t-test

The t-test tests the null hypothesis that the samples have equal means assuming independence, normality and same variance of the samples (see Appendix A for details).

For T_{90}, $F_{\rm best}$ and $F_{\rm bbest}$ in GRBtrun and GRBz these assumptions are met. P-values for the test are listed in Table 6.4. The results are conclusive. For the quantities $F_{\rm best}$ and $F_{\rm bbest}$ in the GRBtrun and GRBz sample the p-values are basically zero. The null hypothesis is rejected on high level of significance. P-value p = 0.02 for T_{90} implies the rejection of the null hypothesis on the given level of significance ($\alpha = 0.05$).

	T_{90}	$F_{\rm best}$	$F_{\rm b,best}$
p-value	0.010	$6.8\text{x}10^{-11}$	$5.1\text{x}10^{-10}$

TABLE 6.4: P-values of the t-test applied on T_{90}, $F_{\rm best}$, $F_{\rm b,best}$ comparing the GRBtrun and GRBz sample.

K–S test

F-test and t-test requires many assumptions, therefore only on three of the measured quantities they can be applied. For the rest of the quantities a more robust test is needed. One of the most common nonparametric statistical tests is the two–sample Kolmogorov–Smirnov test. The null hypothesis I posed is the equality of the continuous distributions of the samples (see Appendix A for details). I performed the test on the quantities of the GRBtrun and GRBz samples as shown in Table 6.1. The p-values are listed in Table 6.5 – second row. The test may be applied directly on the GRBall and GRBz sample, because the assumption of the independence is not necessary. For completeness I calculated the p-values for this case. The p-values are listed in Table 6.5 – first row. As can be seen the p-values are basically the same. The p-value is reasonably accurate for samples which satisfies the condition: $k = N_1N_2/(N_1 + N_2) \geq 4$, where N_1 and N_2 are the sizes of the samples. In both of the cases GRBtrun vs. GRBz and GRBall vs. GRBz sample: k = 26. For illustration, a cumulative plot of the quantity $F_{\rm best}$ for the GRBall and GRBz sample is shown in Figure 6.2. They differ significantly.

	T_{90}	$F_{\rm best}$	$F_{\rm b,best}$	P_{64}	P_{256}	P_{1024}	$P_{\rm b,64}$	$P_{\rm b,256}$	$P_{\rm b,1024}$
all–z	0.142	$1{\cdot}10^{-6}$	$9{\cdot}10^{-7}$	0.009	0.007	0.005	0.002	0.002	0.002
bias–z	0.095	$1{\cdot}10^{-7}$	$9{\cdot}10^{-8}$	0.004	0.003	0.002	$8{\cdot}10^{-4}$	$5{\cdot}10^{-4}$	$8{\cdot}10^{-4}$

TABLE 6.5: P-values of the two–sample K–S test comparing the GRBall with GRBz sample (row "all–z") and GRBtrun with GRBz sample (row bias–z).

The p-values in Table 6.5 of the K–S test shows that only for the T_{90} the null hypothesis cannot be rejected on the given level of significance. For all the other quantities one may conclude that their distributions are different on high level of significance. Thus the original hypothesis "randomness of the sampling from GRBall sample" can be rejected on a high level of significance.

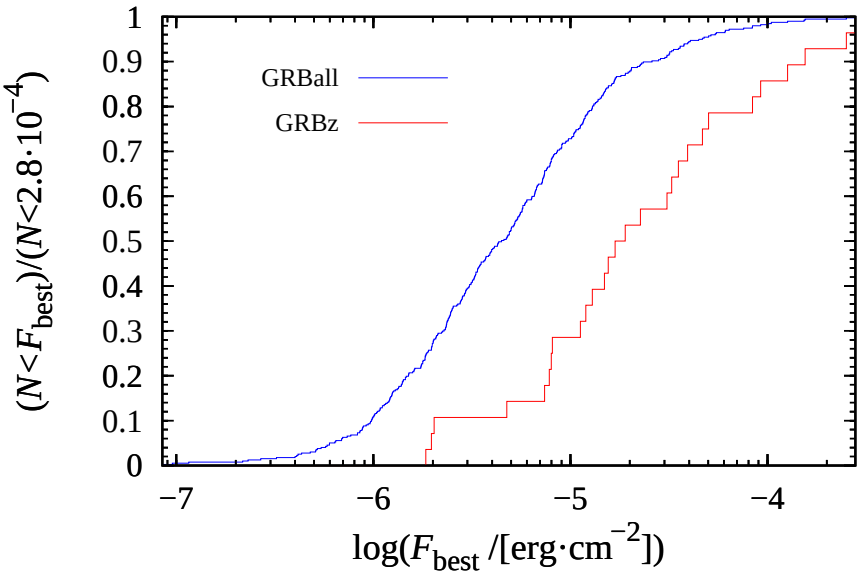

FIGURE 6.2: Cumulative plot of the F_{bias} for the GRBall (blue) and GRBz (red) samples.

All this means that in the definition of the GRBz sample probably some unknown selection effect played a role.

6.2 Percentages of the BAND, PLAW, COMP and SBPL Model

Further, I compare the percentages of the spectra, best fitted by the BAND,...,SBPL model in the GRBz sample, with the percentages of the spectra, best fitted by the BAND,...,SBPL model in the GRBall sample. Table 6.6 shows the topical numbers and percentages according to the best fitted spectral function. One can see that the percentage of the PLAW model in the GRBz sample is approximately two times smaller than in the GRBall sample. One explanation may be as follows: the PLAW model is best fitted for bursts with low fluence (peak flux). Assuming that they have high redshifts, they are harder to be observed by ground telescopes.

	Fluence spectra		Peak flux spectra	
	GRBall	GRBz	GRBall	GRBz
BAND	66(16.6 %)	6(21.4 %)	62(15.6 %)	9(32.1 %)
PLAW	83(20.9 %)	2(7.1 %)	168(42.3 %)	6(21.4 %)
COMP	201(50.6 %)	12(42.9 %)	130(32.7 %)	9(32.1 %)
SBPL	47(11.8 %)	8(28.6 %)	37(9.3 %)	4(14.3 %)

TABLE 6.6: List of actual numbers and relevant percentages for the best fitted spectral functions with respect to the GRBall (397 bursts) and GRBz (28 bursts) sample. First two columns describe the fluence spectra (obtained by considering the duration of the bursts) and last two columns describe the peak flux spectra (obtained by considering the 1024ms time scale for the peak flux over the duration).

Chapter 7

Conclusions

In Chapter 2 I summarized the present observational characteristics of the GRBs. Chapter 3 introduced the Fermi satellite and its data products.

In Chapter 4 I described the creation of the three GRB samples and the process of acquiring the data from the FERMIGBRST database. First, the GRBall sample was created. It contained the sample of GRBs that were longer than 2 s and their spectral characteristics in the FERMIGBRST were determined. Second, the bursts from the GRBall sample that have determined redshifts, were designated as the GRBz sample. The redshifts were obtained from the heavily referenced Greiner table. Third, the GRBtrun sample was defined as GRBall minus GRBz sample.

The quantities F_{best} and $F_{\mathrm{b,best}}$ were defined as the fluence that is obtained by integrating the best fitted spectral function over the duration of the burst in $\langle 10, 1000\rangle$ keV and $\langle 50, 300\rangle$ keV energy range, respectively. The quantity $P_{\mathrm{b,best}}$ was defined as the fluence that is obtained by integrating the best fitted spectral function over the peak flux of the burst in $\langle 50, 300\rangle$ keV energy range.

In Chapter 5 I investigated the intrinsic properties of the bursts in the GRBz sample. Intrinsic quantities E_{iso}, the isotropic equivalent energy, and L_{iso}, the isotropic equivalent peak luminosity on 1024 ms timescale, were calculated from the F_{best}, $F_{\mathrm{b,best}}$ and $P_{\mathrm{b,best}}$, respectively. The source frame energy range in which E_{iso} and L_{iso} were computed was $\langle 0.1, 10\,000\rangle$ keV. The calculation encompassed the proper usage of the k-correction in gamma-band. The relevant k-correction factors for F_{best}, $F_{\mathrm{b,best}}$ and $P_{\mathrm{b,best}}$ were computed.

A correlation between E_{iso} and a function of the redshift was found, $\rho \sim -0.5$ (Figure 5.1). The correlation coefficient ρ was determined by the statistical method of Maximum Likelihood Estimation (MLE). Assumption of bivariate log-normality of F_{best} was addressed by a computation of p-values of the multivariate Jarque-Bera tests. The p-values were always higher than the significance level $\alpha = 0.05$, implying correctness of the assumption. It has been shown that the strength of this correlation does not

depend on the usage of the k-correction. Additionally, correlation coefficient between $E_{\rm iso}$ and redshift z was found to be $\rho_E = 0.63$.

A correlation between $L_{\rm iso}$ and redshift was also found. The correlation coefficient is $\rho_L = 0.65$.

The key question is if these two correlations are given either by observational biases or are real astrophysical phenomena. In essence, this thesis searches for an answer to this question.

In section 5.2 I showed that most of the correlation can be explained by the detection threshold effect – the lowest peak luminosity of the bursts that could trigger a detector is an increasing function of the redshift. The detection threshold curve was computed assuming a sharp detection threshold model with threshold peak flux $P_{\rm tr} = 0.7\,{\rm ph}\cdot{\rm cm}^{-2}\cdot{\rm s}^{-1}$ and typical Band spectrum with spectral parameters as medians of the spectral parameters of the GRBz sample.

In Section 5.3 the apparent deficit in observed rate of the bright bursts $L_{\rm iso} \gtrsim 5\cdot 10^{52}\,{\rm erg}\cdot{\rm s}^{-1}$ on low redshifts $z \lesssim 1.5$, was analyzed. To test the hypothesis that this deficit is caused by the luminosity function evolution, a sample of GRBs with $L_{\rm iso} \geq 1.36\cdot 10^{52}\,{\rm erg}\cdot{\rm s}^{-1}$ and $z \leq 2.374$ was chosen. This sample was divided into two independent subsamples, each containing bursts within non-overlapping luminosity ranges. Assuming that the deficit in observed rate is caused by the GRB rate evolution and that the luminosity function is redshift independent, the GRB rate should have the same functional form on the redshift for each of the subsamples of GRBs within the non-overlapping luminosity ranges. The GRB rate was assumed to be proportional to the star formation rate (SFR) times a power law function $(1+z)^{\omega}$. Power law exponent $\omega_{\rm max}$, that explained the observed distribution of the luminosity subsamples the best, was found by maximizing the p-value of the K-S test. The null hypothesis of the K-S test was that the observed distribution of the bursts comes from the theoretical distribution, that was the function of z and ω. The values of $\omega_{\rm max}$ were computed. They were found to be strongly dependent on the way of splitting the GRBs into the luminosity subsamples and slightly dependent on the assumed form of the SFR function. The confidence intervals (for p-value $> \alpha = 0.05$) of ω were found to have ranges $\sim 6-10$ and that they are overlapping for the GRBs within different luminosity intervals. This means that the hypothesis of the luminosity function evolution is not supported by the data. P-values of the two-sample K-S test applied on the two independent luminosity subsamples yielded the same conclusion.

In Chapter 6 the statistical analysis of the GRBz, GRBall and GRBtrun samples was performed. It was shown that the GRBz sample is not a random sampling from the GRBall sample. The null hypothesis that the GRBz sample and GRBall sample comes from the same distribution was rejected on high level of significance. The physical quantities of the bursts in the GRBz and GRBall samples that were actually tested are

T_{90}, $F_{\rm best}$, $F_{\rm b,best}$ and peak fluxes on various time scales and energy ranges. Except for T_{90}, the p-values of the K-S test ranges from 0.009 to $9 \cdot 10^{-8}$.

The Lilliefors test of normality applied on the log-normal values of the physical quantities T_{90}, $F_{\rm best}$ and $F_{\rm b,best}$, yielded high p-values ($p > \alpha = 0.15$), concluding that the assumption of log-normality is not rejected on the given significance level. On the other hand, p-values of the Lilliefors test for the peak fluxes are virtually zero for GRBall and GRBtrun sample, rejecting the log-normality assumption.

All these statistical efforts suggest that the correlations, shown in Figures 5.1, 5.2, 5.9, 5.8 and 5.9, can be probably explained by observational biases (compare with the findings of Wanderman and Piran (2010) and Lloyd-Ronning et al. (2002) in subsection 2.3.3). Also the sample GRBz itself is observationaly biased, if it is compared either with GRBall or with GRBtrun sample (Chapter 6). On the other hand, a real dependence on the redshift of $E_{\rm iso}$ and $L_{\rm iso}$, respectively, is not excluded yet, but simply it cannot be proclaimed unambiguously.

Appendix A

Used Statistical Tests

In this section of the thesis I shortly describe the statistical tests used in Chapters 5 and 6. Except of the multivariate Jarque–Bera test of normality, all tests were performed by using the relevant functions in The Statistics Toolbox in Matlab. For more detailed information one should look in the Statistics Toolbox Manual and the references within[1].

A.1 Lilliefors Test of Normality

The Lilliefors test is a two-sided goodness-of-fit test used when the exact form of the null distribution is unknown. However, the null distribution must be a member of a location-scale family of distributions. The null hypothesis is that the sample comes from the null distribution. The test has an advantage of giving accurate results even if the size of the sample is small $N < 50$. It is a modification of the well-known Kolmogorov–Smirnov test.

The Lilliefors test statistic is

$$D^* = \max_x |F(x) - G(x)|,$$

where $F(x)$ is the empirical CDF of the sample and $G(x)$ is the CDF of the hypothesized distribution with estimated parameters equal to the sample parameters[2]. On the given significance level α, the null hypothesis is rejected if D^* will be greater than or equal to the critical value D_{critical}, which is a critical value for the distribution of the Lilliefors test. It must be computed by using the Monte Carlo technique.

[1] www.mathworks.com/help/stats/index.html
[2] www.mathworks.com/help/stats/lillietest.html

A.2 Two-sample t-Test

The two-sample t-test is a parametric test which is used for testing if two independent normally distributed random samples, $\{x_i = 1, \ldots, N_\mathrm{x}\}$ and $\{x_i = 1, \ldots, N_\mathrm{x}\}$, have equal population means. Further, suppose that the population variances are equal. There exist many variations, from which I choose the following. The test statistic is given as

$$t = \frac{\overline{x} - \overline{y}}{s_{xy}\sqrt{\frac{1}{N_\mathrm{x}} + \frac{1}{N_\mathrm{y}}}},$$

where

$$s_{xy} = \sqrt{\frac{(N_\mathrm{x} - 1)s_\mathrm{x}^2 + (N_\mathrm{y} - 1)s_\mathrm{y}^2}{N_\mathrm{x} + N_\mathrm{y} - 2}},$$

where $\overline{x}$ and $\overline{y}$ are the sample means, s_x^2 and s_y^2 are the sample variances and N_x and N_y are the sizes of the samples.

The null hypothesis (means are equal) is rejected (in favor of the two sided alternative hypothesis that the means are not equal) on the significance level α, when the test statistic $|t| > t_{1-\alpha/2, N_\mathrm{x}+N_\mathrm{y}-2}$, where $t_{1-\alpha/2, N_\mathrm{x}+N_\mathrm{y}-2}$ is $(1 - \alpha/2)$-quantile of the t-distribution with $N_\mathrm{x} + N_\mathrm{y} - 2$ degrees of freedom.

A.3 Two-sample F-Test

The two-sample F-test is a parametric test which is used for testing if two independent normally distributed random samples, $\{x_i = 1, \ldots, N_\mathrm{x}\}$ and $\{x_i = 1, \ldots, N_\mathrm{x}\}$, have equal population variances. The test statistic is given as

$$F = \frac{s_\mathrm{x}^2}{s_\mathrm{y}^2},$$

where s_x^2 and s_y^2 are the sample variances.

The null hypothesis (variances are equal) is rejected (in favor of the alternative hypothesis that the variances are not equal) on the significance level α, when the test statistic $F > F_{\alpha/2, N_\mathrm{x}-1, N_\mathrm{y}-1}$ or $F > 1/F_{\alpha/2, N_\mathrm{x}-1, N_\mathrm{y}-1}$, where $F_{\alpha/2, N_\mathrm{x}-1, N_\mathrm{y}-1}$ is $(1 - \alpha/2)$-quantile of the F-distribution with $N_\mathrm{x} - 1$ and $N_\mathrm{y} - 1$ degrees of freedom.

A.4 One-Sample Kolmogorov–Smirnov Test

The one-sample Kolmogorov–Smirnov test is a non-parametric statistical test which is used for testing if the sample, $\{x_i = 1, \ldots, n\}$, comes from the hypothesized continuous

distribution $g(x)$. The test statistic is given as

$$D = \max_x |F(x) - G(x)|,$$

where $F(x)$ is the empirical CDF of the sample and $G(x)$ is the hypothesized cumulative distribution obtained from $g(x)$.

The null hypothesis (sample comes from the hypothesized distribution) is rejected in favor of two-sided alternative hypothesis (sample does not come from the hypothesized distribution $G(x)$) on a given significance level α if the test statistic $D > D_{\text{crit}}/\sqrt{n}$, where n denotes the sample size and D_{crit} is found from

$$\text{Prob}(K \leq D_{\text{crit}}) = 1 - \alpha,$$

where

$$\text{Prob}(K \leq x) = \frac{\sqrt{2\pi}}{x} \sum_{k=1}^{\infty} \exp^{-(2k-1)^2\pi^2/(8x^2)}.$$

A.5 Two-sample Kolmogorov–Smirnov Test

The two-sample Kolmogorov–Smirnov test is a non-parametric statistical test which is used for testing if two samples, $\{x_i = 1, \ldots, n\}$ and $\{y_i = 1, \ldots, m\}$, come from the same distribution. The test statistic is given as

$$D = \max_x |F_{1,n}(x) - F_{2,m}(x)|,$$

where $F_{1,n}$ and $F_{2,m}$ are empirical CDFs of the samples.

The null hypothesis (samples come from the same distribution) is rejected in favor of two-sided alternative hypothesis (samples do not come from the same distribution) on a given significance level α if the test statistic D meets the condition

$$\sqrt{\frac{nm}{n+m}} D > D_{\text{crit}},$$

where D_{crit} is defined in previous section.

A.6 Multivariate Jarque–Bera Test

The univariate Jarque–Bera test is a well known statistical test of normality. For assessing a multivariate normality Koizumi et al. (2009) proposed four new test statistics. Two of them are described below.

For small sample size Koizumi et al. (2009) recommend to use the test statistics MJB^*_{M} and MJB^*_{S}, whose definitions are as follows,

$$MJB^*_{\mathrm{M}} = z^*_{\mathrm{M},1} + z^{*^2}_{\mathrm{M},2}$$

and

$$MJB^*_{\mathrm{S}} = z^*_{\mathrm{S},1} + z^{*^2}_{\mathrm{S},2},$$

where

$$z^*_{\mathrm{M},1} = \frac{N}{6} b_{\mathrm{M},1} \frac{(p+1)(N+1)(N+3)}{N[(N+1)(p+1)-6]},$$

$$z^*_{\mathrm{M},2} = \frac{\sqrt{(N+3)(N+5)}\,[(N+1)b_{\mathrm{M},2} - p(p+2)(N-1)]}{\sqrt{8p(p+2)(N-3)(N-p-1)(N-p+1)}},$$

$$z^*_{\mathrm{S},1} = \frac{(N+1)(N+3)}{6(N-2)} p b_{\mathrm{S},1},$$

and

$$z^*_{\mathrm{S},2} = \frac{\sqrt{p(N+3)(N+5)}\,[(N+1)b_{\mathrm{S},2} - 3(N-1)]}{\sqrt{24N(N-2)(N-3)}}.$$

Further

$$b_{\mathrm{M},1} = \frac{1}{N^2} \sum_{i=1}^{N} \sum_{j=1}^{N} \left[(\vec{x}_i - \vec{x})' S^{-1} (\vec{x}_j - \vec{x})\right]^3,$$

$$b_{\mathrm{M},2} = \frac{1}{N} \sum_{i=1}^{N} \left[(\vec{x}_i - \vec{x})' S^{-1} (\vec{x}_i - \vec{x})\right]^2,$$

$$b_{\mathrm{S},1} = \frac{1}{N^2 p} \sum_{i=1}^{p} \left[\omega_i^{-\frac{3}{2}} \sum_{j=1}^{N} (v_{ij} - \vec{v}_i)^3 \right]^2$$

and

$$b_{\mathrm{S},2} = \frac{1}{Np} \sum_{i=1}^{p} \omega_i^{-2} \sum_{j=1}^{N} (v_{ij} - \vec{v}_i)^4,$$

where $\vec{x} = \frac{1}{N} \sum\limits_{j=1}^{N} \vec{x}_j$, $S = \frac{1}{N} \sum\limits_{j=1}^{N} (\vec{x}_j - \vec{x})(\vec{x}_j - \vec{x})'$, $v_{ij} = \vec{h}_i' \vec{x}_j$, $\vec{v}_i = \frac{1}{N} \sum\limits_{j=1}^{N} v_{ij}$. Finally, $\vec{x}_i, i = 1, \ldots, N$ is the multivariate sample with N observations and the dimensionality of $\vec{x}_i$ is p. ω_i and $\vec{h}_i$ are eigenvalues and eigenvectors of the matrix S, respectively.

The test statistic MJB^*_{M} has a χ^2-distribution with $f+1$ degrees of freedom, where $f = p(p+1)(p+2)/6$. The null hypothesis (the data comes from p-variate normal distribution) is rejected (in favor of the alternative hypothesis that the data do not come from p-variate normal distribution) on a given significance level α if the test statistic $MJB^*_{\mathrm{M}} > \chi^2_{1-\alpha,f+1}$, where $\chi^2_{1-\alpha,f+1}$ is $(1-\alpha)$-quantile of χ^2-distribution with $f+1$ degrees of freedom.

The test statistic MJB^*_{S} has a χ^2-distribution with $p+1$ degrees of freedom. The

null hypothesis (the data comes from p-variate normal distribution) is rejected (in favor of the alternative hypothesis that the data do not come from p-variate normal distribution) on a given significance level α if the test statistic $MJB_{\mathrm{S}}^{*} > \chi^2_{1-\alpha,p+1}$, where $\chi^2_{1-\alpha,p+1}$ is $(1-\alpha)$-quantile of χ^2-distribution with $p+1$ degrees of freedom.

A.7 Maximum Likelihood Estimation

The maximum likelihood estimation is a method used to estimate the parameters of hypothesized statistical model. Let us have a sample of n independent and identically distributed observations $\{\vec{x}_i, i = 1, \ldots, n\}$, that follow a certain parametric statistical distribution $f(\cdot|\vec{\theta}_0)$. The parameter vector $\vec{\theta}_0$ is unknown and MLE defines its estimation from the sample $\vec{x}_i$ by maximizing the likelihood function

$$\mathcal{L}\left(\vec{\theta}|\vec{x}_1, \ldots, \vec{x}_n\right) = \prod_{i=1}^{n} f\left(\vec{x}_i|\vec{\theta}\right).$$

In practice one works with the logarithm of $\mathcal{L}$. In that case it is maximized

$$\ln\mathcal{L}\left(\vec{\theta}|\vec{x}_1, \ldots, \vec{x}_n\right) = \sum_{i=1}^{n} \ln\left[f\left(\vec{x}_i|\vec{\theta}\right)\right].$$

Appendix B

Computation of Uncertainties

In this section I briefly describe the method used to compute the uncertainties for $L_{\langle 0.1,10\,000\rangle}$ in table 5.4. The method is a widely known Monte Carlo technique (Gentle 2003).

Let us have a continuous function $g = f(a_1, \ldots, a_N)$. Assume that the multivariate error distribution function for the parameters $a_1, \ldots, a_N$ is a multivariate normal distribution, $\mathcal{N}_N(\mu, \Sigma)$, where Σ is covariance matrix of the parameters $a_1, \ldots, a_N$. Having a random vector $\vec{x}$, each of its component coming from the normal distribution $\mathcal{N}(0, 1)$, correlated random vector $\vec{b}$ is computed as follows

$$\vec{b} = \vec{\mu} + \mathcal{T}^{\mathrm{T}}\vec{x},$$

where $\mathcal{T}^{\mathrm{T}}$ is defined such that $\mathcal{T}^{\mathrm{T}}\mathcal{T} = \Sigma$. $\mathcal{T}$ is a Cholesky factor of Σ.

Now generate n random vectors $\vec{b}_i, i = 1, \ldots, n$ and for each compute $\vec{g}_i = f(\vec{b}_i)$. Sample of vectors $\vec{g}_i$ comes from the probability density distribution of g (g_{PDF}).

To compute a confidence interval of the g, $\langle g_{\mathrm{lower}}, g_{\mathrm{upper}}\rangle$, one need to choose the lower and upper quantiles (q_{lower} and q_{upper}).

One may, by brute computational force, estimate the g_{PDF} very accurately. The accuracy is better for larger n. Reasonable results can be obtained with $n \sim 10\,000$.

Appendix C

Selected Parameters from the FERMIGBRST Database

The parameters selected from the FERMIGBRST database, which were used in the calculation of the $E_{\langle 0.1,10\,000\rangle}$, $L_{ave,\langle 0.1,10\,000\rangle}$, $L_{\langle 0.1,10\,000\rangle}$ and the relevant k-correction factors, are listed below. For their detailed description one should look on the web page of the FERMIGBRST database[1].

t90	flnc_sbpl_pivot
flux_64	flnc_sbpl_indx1
flux_256	flnc_sbpl_brken
flux_1024	flnc_sbpl_brksc
flux_batse_64	flnc_sbpl_indx2
flux_batse_256	flnc_sbpl_ergflnc
flux_batse_1024	flnc_sbpl_ergflncb
flnc_best_fitting_model	pflx_best_fitting_model
flnc_band_ampl	pflx_band_ampl
flnc_band_epeak	pflx_band_epeak
flnc_band_alpha	pflx_band_alpha
flnc_band_beta	pflx_band_beta
flnc_band_ergflnc	pflx_plaw_ampl
flnc_band_ergflncb	pflx_plaw_pivot
flnc_plaw_ampl	pflx_plaw_index
flnc_plaw_pivot	pflx_comp_ampl
flnc_plaw_index	pflx_comp_epeak
flnc_plaw_ergflnc	pflx_comp_index
flnc_plaw_ergflncb	pflx_comp_pivot
flnc_comp_ampl	pflx_sbpl_ampl
flnc_comp_epeak	pflx_sbpl_pivot
flnc_comp_index	pflx_sbpl_indx1
flnc_comp_pivot	pflx_sbpl_brken
flnc_comp_ergflnc	pflx_sbpl_brksc
flnc_comp_ergflncb	pflx_sbpl_indx2
flnc_sbpl_ampl	

Table C.1: Selected parameters from the FERMIGBRST database.

[1] heasarc.gsfc.nasa.gov/W3Browse/fermi/fermigbrst.html

Appendix D

Designations of the GRBs in the GRBall and the GRBtrun Samples

GRB080714086	GRB081130212	GRB090518244	GRB090912660	GRB100219026
GRB080714425	GRB081130629	GRB090519462	GRB090915650	GRB100221368
GRB080714745	GRB081204004	**GRB090519881**	GRB090917661	GRB100224112
GRB080715950	GRB081206275	GRB090520850	GRB090920035	GRB100225115
GRB080717543	GRB081206604	GRB090520876	GRB090922539	GRB100225249
GRB080719529	GRB081206987	GRB090522344	GRB090922605	GRB100225580
GRB080723557	GRB081207680	GRB090524346	GRB090925389	GRB100225703
GRB080723985	GRB081215784	GRB090528173	**GRB090926181**	GRB100228544
GRB080724401	GRB081215880	GRB090528516	**GRB090926914**	GRB100228873
GRB080725435	GRB081217983	GRB090529310	GRB090928646	GRB100301223
GRB080727964	**GRB081221681**	GRB090529564	GRB090929190	GRB100304004
GRB080730520	**GRB081222204**	GRB090530760	GRB091002685	GRB100304534
GRB080730786	GRB081224887	GRB090602564	**GRB091003191**	GRB100306199
GRB080803772	GRB081225257	GRB090606471	GRB091005679	GRB100307928
GRB080804456	GRB081226156	GRB090608052	GRB091010113	GRB100311518
GRB080804972	GRB081231140	GRB090610648	GRB091015129	GRB100313288
GRB080805496	GRB090101758	GRB090610723	GRB091017861	GRB100313509
GRB080805584	**GRB090102122**	GRB090610883	GRB091017985	GRB100315361
GRB080806584	GRB090107681	GRB090612619	**GRB091020900**	GRB100318611
GRB080806896	GRB090112332	**GRB090618353**	GRB091020977	GRB100322045
GRB080807993	GRB090112729	GRB090620400	GRB091023021	GRB100323542
GRB080808451	**GRB090113778**	GRB090621185	**GRB091024372**	GRB100324172
GRB080808565	GRB090117335	GRB090621417	**GRB091024380**	GRB100325246
GRB080808772	GRB090117632	GRB090621447	GRB091026485	GRB100325275
GRB080809808	GRB090117640	GRB090623107	GRB091026550	GRB100326294
GRB080810549	GRB090126227	GRB090623913	GRB091030613	GRB100326402
GRB080812889	GRB090129880	GRB090625234	GRB091030828	GRB100330309
GRB080816503	GRB090131090	GRB090625560	GRB091031500	GRB100330856

GRB080816989	GRB090202347	GRB090626189	GRB091101143	GRB100401297
GRB080817161	GRB090207777	GRB090629543	GRB091102607	GRB100406758
GRB080817720	GRB090217206	GRB090630311	GRB091103912	GRB100410356
GRB080818579	GRB090222179	GRB090701225	GRB091106762	GRB100410740
GRB080818945	GRB090225009	GRB090703329	GRB091107635	GRB100413732
GRB080821332	GRB090227310	GRB090704242	GRB091109895	**GRB100414097**
GRB080823363	GRB090228976	GRB090704783	GRB091112737	GRB100417789
GRB080824909	GRB090301315	GRB090706283	GRB091112928	GRB100420008
GRB080825593	GRB090304216	GRB090708152	GRB091115177	GRB100421917
GRB080828189	GRB090306245	GRB090709630	GRB091117080	GRB100423244
GRB080829790	GRB090307167	GRB090711850	GRB091120191	GRB100424729
GRB080830368	GRB090309767	GRB090713020	GRB091123081	GRB100424876
GRB080831921	GRB090310189	GRB090717034	GRB091123298	GRB100427356
GRB080904886	GRB090316311	GRB090718720	**GRB091127976**	GRB100429999
GRB080905570	GRB090319622	GRB090718762	GRB091128285	GRB100502356
GRB080905705	GRB090320045	GRB090719063	GRB091201089	GRB100503554
GRB080906212	GRB090320418	GRB090720276	GRB091202072	GRB100504806
GRB080912360	GRB090320801	GRB090720710	GRB091202219	GRB100506653
GRB080913735	**GRB090323002**	GRB090725838	GRB091207333	GRB100507577
GRB080916009	GRB090326633	GRB090730608	**GRB091208410**	GRB100510810
GRB080916406	GRB090327404	GRB090802666	GRB091209001	GRB100511035
GRB080920268	**GRB090328401**	GRB090804940	GRB091215234	GRB100513879
GRB080924766	GRB090330279	GRB090805622	GRB091219462	GRB100515467
GRB080925775	GRB090403314	GRB090807832	GRB091220442	GRB100516369
GRB080927480	GRB090409288	GRB090809978	GRB091221870	GRB100517072
GRB080928628	GRB090411838	GRB090810659	GRB091223511	GRB100517132
GRB081003644	GRB090411991	GRB090810781	GRB091227294	GRB100517154
GRB081006604	GRB090413122	GRB090811696	GRB091230260	GRB100517243
GRB081006872	GRB090419997	GRB090813174	GRB091230712	GRB100517639
GRB081008832	GRB090422150	GRB090814950	GRB091231206	GRB100519204
GRB081009140	GRB090423330	GRB090815300	GRB091231540	GRB100522157
GRB081009690	**GRB090424592**	GRB090815438	GRB100101028	GRB100527795
GRB081012549	GRB090425377	GRB090815946	GRB100111176	GRB100528075
GRB081017474	GRB090426066	GRB090817036	GRB100112418	GRB100530737
GRB081021398	GRB090426690	GRB090820027	GRB100116897	GRB100604287
GRB081022364	GRB090427688	GRB090820509	GRB100118100	GRB100605774
GRB081024851	GRB090428441	GRB090823133	GRB100122616	GRB100608382
GRB081025349	GRB090428552	GRB090824918	GRB100126460	GRB100609783
GRB081028538	GRB090429530	GRB090826068	GRB100130729	GRB100612726
GRB081101167	GRB090502777	GRB090828099	GRB100130777	GRB100614498
GRB081101532	GRB090509215	GRB090829672	GRB100131730	GRB100615083
GRB081102739	GRB090510325	GRB090829702	GRB100201588	GRB100619015
GRB081109293	GRB090511684	GRB090831317	GRB100204024	GRB100620119
GRB081110601	GRB090513916	GRB090902401	GRB100204566	GRB100621452
GRB081118876	GRB090513941	**GRB090902462**	GRB100205490	GRB100625891
GRB081120618	GRB090514006	GRB090904058	GRB100207665	GRB100701490
GRB081121858	GRB090514726	GRB090904581	GRB100207721	GRB100704149
GRB081122520	GRB090514734	GRB090907017	GRB100210101	GRB100707032

GRB081124060	GRB090516137	GRB090908314	GRB100211440	GRB100709602
GRB081125496	**GRB090516353**	GRB090908341	GRB100212550	
GRB081126899	GRB090516853	GRB090909487	GRB100212588	
GRB081129161	GRB090518080	GRB090910812	GRB100218194	

TABLE D.1: Designations of the bursts in the GRBall sample (all entries). Bold entries denote the bursts in the GRBz sample and entries in normal font denote the burst in GRBtrun sample.

List of Figures

List of Tables

Abbreviations

BAT	**B**urst **A**lert **T**elescope
BATSE	**B**urst **a**nd **T**ransient **S**ource **E**xperiment
CGRO	**C**ompton **G**amma-**R**ay **O**bservatory
EGRET	**E**nergetic **G**amma-**R**ay **E**xperiment **T**elescope
FERMIGBRST	**Fermi G**BM **Burst** Catalogue
FoV	**F**ield **o**f **V**iew
GBM	**G**amma-ray **B**urst **M**onitor
GLAST	**G**amma-ray **L**arge **A**rea **S**pace **T**elescope
GRB	**G**amma-**R**ay **B**urst
HETE	**H**igh **E**nergy **T**ransient **E**xplorer
IPN	**I**nter**P**lanetary **N**etwork
K-S	**K**olmogorov-**S**mirnov
LAT	**L**arge **A**rea **T**elescope
LC	**L**ight **C**urve
lGRB	**l**ong **G**amma-**R**ay **B**urst
MC	**M**onte **C**arlo
MJB	**M**ultivariate **J**arque-**B**era
MLE	**M**aximum **L**ikelihood **E**stimation
PDF	**P**robability **D**ensity **F**unction
RHESSI	Reuven **R**amaty **E**nergy **S**olar **S**pectroscopic **I**mager
SFR	**S**tar **F**ormation **R**ate
sGRB	**s**hort **G**amma-**R**ay **B**urst
SN	**Super**nova
UVOT	**U**ltra-**V**iolet/**O**ptical **T**elescope
XRT	**X**-**R**ay **T**elescope

Bibliography

Amati, L., Frontera, F., Tavani, M., et al. (2002). Intrinsic spectra and energetics of BeppoSAX Gamma-Ray Bursts with known redshifts. *Astronomy and Astrophysics*, 390:81.

Atwood, W. B., Abdo, A. A., Ackermann, M., et al. (2009). The Large Area Telescope on the Fermi Gamma-Ray Space Telescope Mission. *The Astrophysical Journal*, 697:1071.

Balázs, L. G., Bagoly, Z., Horváth, I., et al. (2003). On the difference between the short and long gamma-ray bursts. *Astronomy & Astrophysics*, 401:129.

Band, D., Matteson, J., Ford, L., et al. (1993). BATSE observations of gamma-ray burst spectra. 1. Spectral diversity. *The Astrophysiscal Journal*, 413:281.

Barthelmy, S. D., Barbier, L. M., Cummings, J. R., et al. (2005). The Burst Alert Telescope (BAT) on the SWIFT Midex Mission. *Space Science Reviews*, 120:143.

Bloom, J. S., Frail, D. A., & Sari, R. (2001). The prompt energy release of gamma-ray bursts using a cosmological k-correction. *The Astronomical Journal*, 121:2879.

Butler, N. R., Bloom, J. S., & Poznanski, D. (2010). The Cosmic Rate, Luminosity Function, and Intrinsic Correlations of Long Gamma-Ray Bursts. *The Astrophysical Journal*, 711:495.

Bystřický, P. (2011). MsD thesis: Statistical analysis of the gamma-ray bursts satellite data. *Charles University in Prague, Astronomical Insitute.*

Cobb, B., Bloom, J., Cenko, B., et al. (2010). Exceptional Swift and Fermi GRBs: Gemini North Targets of Opportunity. *NOAO Proposal*, page 421.

Cole, S., Norberg, P., Baugh, C. M., et al. (2001). The 2dF galaxy redshift survey: near-infrared galaxy luminosity functions. *Monthly Notices of the Royal Astronomical Society*, 326:255.

Fenimore, E. E. & Bloom, J. S. (1995). Determination of Distance from Time Dilation of Cosmological Gamma-Ray Bursts. *The Astrophysical Journal*, 453:25.

Fenimore, E. E., in 't Zand, J. J. M., Norris, J. P., et al. (1995). Gamma-Ray Burst Peak Duration as a Function of Energy. *Astrophysical Journal Letters*, 448:L101.

Fenimore, E. E. & Ramirez-Ruiz, E. (2000). Redshifts For 220 BATSE Gamma-Ray Bursts Determined by Variability and the Cosmological Consequences. *ArXiv Astrophysics e-prints*, arXiv:astro-ph/0004176.

Firmani, C., Avila-Reese, V., Ghisellini, G., & Tutukov, A. V. (2005). The Luminosity Function and Formation Rate History of GRBs. *Nuovo Cimento C Geophysics Space Physics C*, 28:665.

Fishman, G. J. & Meegan, C. A. (1995). Gamma-Ray Bursts. *Annual Review of Astronomy and Astrophysics*, 33:415.

Gentle, J. E. (2003). Random Number Generation and Monte Carlo Methods. *Springer*, Second edition:197–198.

Ghirlanda, G., Ghisellini, G., & Lazzati, D. (2004). The Collimation-corrected Gamma-Ray Burst Energies Correlate with the Peak Energy of Their νF_ν Spectrum. *The Astrophysical Journal*, 616:331.

Gruber, D. (2012). Rest-frame properties of gamma-ray bursts observed by the Fermi Gamma-Ray Burst Monitor. *ArXiv Astrophysics e-prints*, arXiv:1207.4620.

Guidorzi, C., Frontera, F., Montanari, E., et al. (2005). The gamma-ray burst variability-peak luminosity correlation: new results. *Monthly Notices of the Royal Astronomical Society*, 363:315.

Heise, J., Zand, J. I., Kippen, R. M., et al. (2001). X-Ray Flashes and X-Ray Rich Gamma Ray Bursts. In: *Gamma-ray Bursts in the Afterglow Era*, E. Costa, F. Frontera, & J. Hjorth, ed., page 16.

Hjorth, J., Sollerman, J., Møller, P., et al. (2003). A Very energetic supernova associated with the gamma-ray burst of 29 March 2003. *Nature*, 423:847.

Hopkins, A. M. & Beacom, J. F. (2006). On the Normalization of the Cosmic Star Formation History. *The Astrophysical Journal*, 651:142.

Horváth, I. (1998). A Third Class of Gamma-Ray Bursts? *The Astrophysiscal Journal*, 508:757.

Horváth, I., Balázs, L. G., Hakkila, J., et al. (2012). Classification of Fermi and Swift GRBs. In: *Gamma-Ray Bursts 2012 Conference (GRB 2012)*, page 46.

Kaneko, Y., Preece, R. D., Briggs, M. S., et al. (2006). The Complete Spectral Catalog of Bright BATSE Gamma-Ray Bursts. *The Astrophysical Journal Supplement Series*, 166:298.

Kistler, M. D., Yüksel, H., Beacom, J. F., et al. (2008). An Unexpectedly Swift Rise in the Gamma-Ray Burst Rate. *The Astrophysical Journal*, 673:L119.

Klebesadel, R. W., Strong, I. B., & Olson, R. A. (1973). Observations of Gamma-Ray Bursts of Cosmic Origin. *The Astrophysiscal Journal*, 182:L85.

Koizumi, K., Okamoto, N., & Seo, T. (2009). On Jarque-Bera Tests for Tssessing Multivariate Normality. *Journal of Statistics: Advances in Theory and Applications 1*, 1:207.

Kouveliotou, C., Meegan, C. A., Fishman, G. J., et al. (1993). Identification of two classes of gamma-ray bursts. *The Astrophysiscal Journal*, 413:L101.

Lloyd-Ronning, N. M., Fryer, C. L., & Ramirez-Ruiz, E. (2002). Cosmological Aspects of Gamma-Ray Bursts: Luminosity Evolution and an Estimate of the Star Formation Rate at High Redshifts. *The Astrophysical Journal*, 574:554.

Meegan, C., Lichti, G., Bhat, P. N., et al. (2009). The Fermi Gamma-ray Burst Monitor. *The Astrophysical Journal*, 702:791.

Mészáros, A., Bagoly, Z., Balázs, L. G., et al. (2006). Redshift distribution of gamma-ray bursts and star formation rate. *Astronomy & Astrophysics*, 455:785.

Mészáros, A. & Mészáros, P. (1996). Cosmological Evolution and Luminosity Function Effects on Number Counts, Redshift, and Time Dilation of Bursting Sources. *The Astrophysical Journal*, 466:29.

Mészáros, P. (2006). Gamma-ray bursts. *Reports on Progress in Physics*, 69:2259.

Paciesas, W. S., Meegan, C. A., von Kienlin, A., et al. (2012). The Fermi GBM Gamma-Ray Burst Catalog: The First Two Years. *The Astrophysical Journal Supplement*, 199:18.

Reichart, D. E., Lamb, D. Q., Fenimore, E. E., et al. (2001). A Possible Cepheid-like Luminosity Estimator for the Long Gamma-Ray Bursts. *The Astrophysical Journal*, 552:57.

Řípa, J. (2011). PhD thesis: Statistical Analysis of the Observable Data of Gamma-Ray Bursts. *Charles University in Prague, Astronomical Insitute.*, ArXiv:1105.2467.

Řípa, J., Mészáros, A., Veres, P., et al. (2012). On the Spectral Lags and Peak Counts of the Gamma-Ray Bursts Detected by the RHESSI Satellite. *The Astrophysical Journal*, 756:44.

Salvaterra, R., Campana, S., Vergani, S. D., et al. (2012). A Complete Sample of Bright Swift Long Gamma-Ray Bursts. I. Sample Presentation, Luminosity Function and Evolution. *The Astrophysical Journal*, 749:68.

Schaefer, B. E. (2007). The Hubble Diagram to Redshift > 6 from 69 Gamma-Ray Bursts. *The Astrophysical Journal*, 660:16.

Schaefer, B. E., Deng, M., & Band, D. L. (2001). Redshifts and Luminosities for 112 Gamma-Ray Bursts. *The Astrophysical Journal*, 563:L123.

Stanek, K. Z., Matheson, T., Garnavich, P. M., et al. (2003). Spectroscopic Discovery of the Supernova 2003dh Associated with GRB 030329. *The Astrophysical Journal*, 591:L17.

van Paradijs, J., Groot, P., Galama, T., et al. (1997). Transient optical emission from the error box of the gamma-ray burst of 28 February 1997. *Nature*, 386:686.

Virgili, F. J., Qin, Y., Zhang, B., et al. (2012). Spectral and temporal analysis of the joint Swift/BAT-Fermi/GBM GRB sample. *Monthly Notices of the Royal Astronomical Society*, 424:2821.

Wanderman, D. & Piran, T. (2010). The luminosity function and the rate of Swift's gamma-ray bursts. *Monthly Notices of the Royal Astronomical Society*, 406:1944.

Wang, F.-Y., Qi, S., & Dai, Z.-G. (2011). The updated luminosity correlations of gamma-ray bursts and cosmological implications. *Monthly Notices of the Royal Astronomical Society*, 415:3423.

Xu, M. & Huang, Y. F. (2012). New three-parameter correlation for gamma-ray bursts with a plateau phase in the afterglow. *Astronomy & Astrophysics*, 538:A134.

Yonetoku, D., Murakami, T., Nakamura, T., et al. (2004). Gamma-Ray Burst Formation Rate Inferred from the Spectral Peak Energy-Peak Luminosity Relation. *The Astrophysical Journal*, 609:935.

Zhang, Z. B., Chen, D. Y., & Huang, Y. F. (2012). Correlation between Peak Energy and Peak Luminosity in Short Gamma-Ray Bursts. *The Astrophysical Journal*, 755:55.